STRUCTURAL AND PHYSICAL PROPERTIES OF HIGH REDSHIFT GALAXIES IN THE HUBBLE ULTRA DEEP FIELD

by

Nimish P. Hathi

A Dissertation Presented in Partial Fulfillment
of the Requirements for the Degree
Doctor of Philosophy

ARIZONA STATE UNIVERSITY

August 2008

STRUCTURAL AND PHYSICAL PROPERTIES OF HIGH REDSHIFT GALAXIES IN THE HUBBLE ULTRA DEEP FIELD

by

Nimish P. Hathi

has been approved

May 2008

Graduate Supervisory Committee:

Rogier A. Windhorst, Co-Chair
Sangeeta Malhotra, Co-Chair
James Rhoads
Rolf A. Jansen
Richard Lebed

ACCEPTED BY THE GRADUATE COLLEGE

ABSTRACT

In the past decade, the Hubble Space Telescope has observed large numbers of distant galaxies. Nonetheless, the process of galaxy assembly and formation at high redshifts remains poorly constrained. There is presently little information on structure formation and star-formation processes within these high-redshift galaxies. This dissertation presents results from three studies in the Hubble Ultra Deep Field (HUDF), the deepest optical data yet, to understand these distant galaxies.

The first part of this dissertation is a study of faint compact Lyman-break galaxies (LBGs) at redshift 4 to 6 (about 1 billion years after the Big Bang) in the HUDF. These LBGs are too faint individually to accurately measure their radial surface brightness (SB) profiles. The HUDF images of sets of these LBGs, pre-selected to have nearly identical compact sizes and the roundest shapes, were co-added. From these composite images, average SB profiles were then computed that show that even the faintest galaxies at redshift 4 to 6 are resolved and that the inner regions are best represented by disk-like Sersic profiles.

The second part of this dissertation utilizes the deep GRism ACS Program for Extragalactic Science (GRAPES) to spectroscopically confirm 47 LBGs at redshift 5 to 6 in the HUDF. These 47 galaxies are less dusty than galaxies at redshift 3, and their peak star-formation rate (SFR) intensity (i.e., SFR per unit area) does not vary significantly from that in the local universe. The constancy of this peak intensity implies that the same physical mechanisms limit starburst intensity at all redshifts up to 6.

The third part of this dissertation uses the HUDF images and the GRAPES spectroscopy to explore the stellar population ages of the bulges in late-type galaxies (i.e., Hubble types Sb-Sd) at redshift one. The results show that these late-type bulges are younger and less massive than bulges in early-type galaxies at similar redshifts, and that these late-type bulges are better fit by an exponential than by de Vaucouleurs SB profile. The overall picture emerging from this analysis is that, in late-type galaxies at redshift one, bulges form from disk material rather than from a major-merger event.

This dissertation is dedicated to my wife, Purvi, and to my parents for their unconditional love and support.

ACKNOWLEDGMENTS

The path towards this dissertation, carried out at the Department of Physics at Arizona State University (ASU), spans several years of work, and many people have been involved in and have contributed towards the presented work. I acknowledge my debt to those who have helped along the way.

I would like to express my sincere gratitude to Rogier Windhorst, who has been my supervisor since the beginning of my study. He provided me with many helpful suggestions, important advice, financial support and constant encouragement during the course of this work. He gave me many opportunities to lead proposals and observations, and he took every possible chance he got to introduce my work to others. I am also grateful to Sangeeta Malhotra, for her supervision, discussions, financial support and understanding in various aspects of my research. Her suggestions and guidance have encouraged me throughout the study. I would also thank Seth Cohen, who was very helpful with my everyday research. I learned a lot from him and it was fun working with him. I thank my whole committee for doing their part to make this process worthwhile. They are Rogier Windhorst, Sangeeta Malhotra, Rolf Jansen, James Rhoads, and Richard Lebed.

I gratefully thank my fellow graduate students who provided both emotional support and taught me many of the important skills that I learned along the way. In no particular order, they are Luis Echevarria, Joseph Baker, Joseph Foy, Jason Cook, Violet Taylor, Russell Ryan, Kazuyuki Tamura, Amber Straughn, Hwihyun Kim and Steven Finkelstein. In addition to those already mentioned, I have enjoyed

working with many other excellent astronomers along the way and I thank them for their collaboration and guidance during these years. They are Steven Odewahn, Rolf Jansen, Haojing Yan, Michael Corbin, William Keel, James Rhoads, Norbert Pirzkal, Chun Xu, Ignacio Ferreras, Anna Pasquali, Anton Koekemoer and Norman Grogin.

I would also thank all the rest of the academic and support staff of the Department of Physics, the ASU School of Earth and Space Exploration (SESE) and the International Student Office (ISO) for their hospitality and help during my many years through this process.

Financial support during my research at ASU has come from various sources. First, I thank ASU and the Physics Department for giving me Teaching Assistantship during my initial years of my graduate studies and secondly, I would like to thank STScI/NASA for various research grants, whose funding helped me during my thesis work and those are HST-GO-9066, HST-GO-9780, HST-GO-9793, HST-GO-10530, HST-AR-10298, HST-AR-11258 & HST-AR-11287 from STScI, which is operated by AURA under NASA contract NAS5-26555. I would also like to thank the Graduate Professional Student Association (GPSA) at ASU for their travel grants for my conference presentations.

Finally but most importantly, I thank my wife and parents, for supporting me along the way. Your patience, love and encouragement have upheld me particularly in those days in which I spent more time with my computer than with you. I also appreciate the support from the rest of my family over the years.

TABLE OF CONTENTS

Page

Page

Page

LIST OF TABLES

LIST OF FIGURES

Figure Page

1. INTRODUCTION

In the past decade, space-based and ground-based observations of high redshift galaxies have begun to outline the process of galaxy assembly. The details of that process at high redshifts, however, remain poorly constrained. There are two major — somewhat contradicting — scenarios of galaxy assembly and formation. Many observational and theoretical predictions favor a hierarchical picture of galaxy formation, in which galaxies we observe locally were built-up by a series of mergers from smaller building blocks (e.g., Yan & Windhorst 2004a; Ferguson *et al.* 2004; Ryan *et al.* 2007), while in an alternate 'anti'-hierarchical scenario, the most massive galaxies assemble earlier than their less massive counterparts (e.g., Cowie *et al.* 1996; Heavens *et al.* 2004; Panter *et al.* 2007). The only way to test these or similar scenarios, and to constrain their details, is to obtain deep multi-color imaging and study distant galaxies while they undergo such processes.

In the last decade, major deep high-resolution imaging surveys, such as the Hubble Deep Fields (HDF; Williams *et al.* 1996), the Great Observatories Origins Deep Survey (GOODS; Giavalisco *et al.* 2004a), the Galaxy Evolution from Morphology and SEDs (GEMS; Rix *et al.* 2005), the Hubble Ultra Deep Field (HUDF; Beckwith *et al.* 2006), the All-wavelength Extended Groth Strip International Survey (AEGIS; Davis *et al.* 2007), and the Cosmological Evolution Survey (COSMOS; Scoville *et al.* 2007), have increased the availability of deep imaging manifold. It is no longer possible to obtain ground-based spectroscopic identification for every source in a field, both due to the huge number of sources in a field and due to the faintness of these distant sources.

Photometric redshift techniques use broad-band photometry obtained through various band-passes (filters) to estimate (the observed) Spectral Energy Distributions (SEDs) of each galaxy. These observed SEDs are in a sense very low resolution spectra that can be compared to theoretical SEDs to estimate the redshifts and the intrinsic properties of distant galaxies. Therefore, photometric redshifts estimated from observed fluxes are an important tool for the statistical study of distant galaxies (e.g., Fernández-Soto *et al.* 1999; Benitez 2000; Mobasher *et al.* 2004, 2007; Ryan *et al.* 2007). Details of this technique are described in, e.g., Ryan *et al.* (2007). The success of photometric redshift techniques heavily relies on observing either of the two strongest spectral features (breaks) in the observed galaxy SEDs. These are the Lyman-break (below rest-frame 1216 Å) and the 4000 Å break (due to the combination of the Balmer break at 3646 Å, higher order Balmer absorption lines and absorption by ionized metals especially Ca II H-K). These two spectral breaks are very useful to identify distant ($z \gtrsim 1$) galaxies, because at these redshifts, these breaks are redshifted into the observed optical/near-infrared band-passes, which are most observed in major imaging surveys. This dissertation is based on three different studies of distant ($z \gtrsim 1$) galaxies selected by their Lyman and 4000 Å breaks as discussed in following two sections.

1.1. *Lyman Break Selection ($z \gtrsim 3$)*

The Lyman-break technique (Steidel & Hamilton 1992; Steidel *et al.* 1996a) has been widely used to select galaxies at high redshifts ($z \gtrsim 3$). This method relies on multi-band imaging to identify the redshifted, characteristic discontinuity — the

Lyman-break — in the SED of high-redshift galaxies, which is largely caused by the Lyman limit and Lyman-α absorption ($\lambda_{rest} \lesssim 1216$ Å) of far-Ultraviolet (UV) photons by intervening neutral hydrogen along the sight-lines to such galaxies (e.g., Madau 1995). This technique requires imaging in at least two passbands, one to the blue side of the break and the other to the red side. The presence of a Lyman-break makes high-redshift galaxies much fainter in the blue band than in the red one, or in other words, it makes them appear to "drop-out" from the blue band. For this reason, this method is also known as the drop-out selection, and the candidates found in this way are generally referred to as "dropouts".

The 'classical' Lyman-break technique used by Steidel *et al.* (1996a) uses three filters: one redward of rest frame Lyman-α ($\lambda_{rest} > 1216$ Å), a second in the spectral region between rest frame Lyman-α and the rest frame Lyman limit (912 Å), and a third at $\lambda_{rest} < 912$ Å. At $z \simeq 3$, the technique relies on the ubiquitous step in the spectra of the stellar component of galaxies at 912 Å. The photons emitted by the galaxy at wavelengths bluer than the Lyman limit are capable of ionizing neutral hydrogen, and thus are quickly absorbed by even a slight amount of intervening neutral hydrogen in the intergalactic medium (IGM) along the sight-line. This Lyman-break technique was first applied to galaxies at $z \simeq 3$. At these redshifts, the strongest drop in the flux level occurs at/below restframe 912 Å, which in the observer's frame occurs in UV filters, such as F300W on the *Hubble Space Telescope* (*HST*), or the ground-based U-band at slightly longer wavelengths ($\sim$3600 Å). Because the break occurs in the U-band, these galaxies are also called U-band dropouts. At higher redshifts

($z \simeq 4$ and beyond), there are more intervening neutral hydrogen clumps between the observer and a galaxy, and the Lyman-α absorption forest (between Ly-α and Ly-β) and the Lyman-β absorption forest (between Ly-β and Lyman limit) — due to thick intervening neutral hydrogen clouds — becomes so dense that most of the UV continuum blueward of rest-frame 1216 Å will be absorbed (see Madau 1995). As we move to higher redshifts, this break travels into optical bands redwards of the U-band and therefore, for galaxies at $z \simeq 4$ ($3.5 \leq z \leq 4.4$) it occurs in the B-band (F435W). This galaxy population at $z \simeq 4$ is also called the "B-band dropouts". Similarly, galaxies at $z \simeq 5$ ($4.5 \leq z \leq 5.4$) are referred to as "V-band (F606W) dropouts".

As its first application in the $z \simeq 6$ regime, Yan *et al.* (2003, hereafter YWC03) used this technique in a deep field observed by the Advanced Camera for Surveys (ACS) in the default pure parallel mode (Sparks *et al.* 2001) soon after its deployment on-board the *HST*. In this redshift range, the Lyman-break occurs at around 8512 Å in the observer's frame, which is well bracketed by the i' (F775W) and z' (F850LP) filters (as shown in Figure 1), through which this deep parallel field was imaged. YWC03 found a significant number of i'-band dropouts, and argued that the vast majority of them were very likely galaxies at $z \simeq 6$.

Many recent surveys have found a large numbers of these dropouts, which are candidate galaxies at $z \gtrsim 4$. The HUDF, GOODS and deep ACS parallel fields contain $\gtrsim$500 objects (Yan & Windhorst 2004a,b; Beckwith *et al.* 2006; Bouwens *et al.* 2006, 2007) which are B, V, or i'-band dropouts, making them candidates for galaxies at $z \simeq 4$, 5, 6, respectively. Figure 2 shows an example of a dropout galaxy at

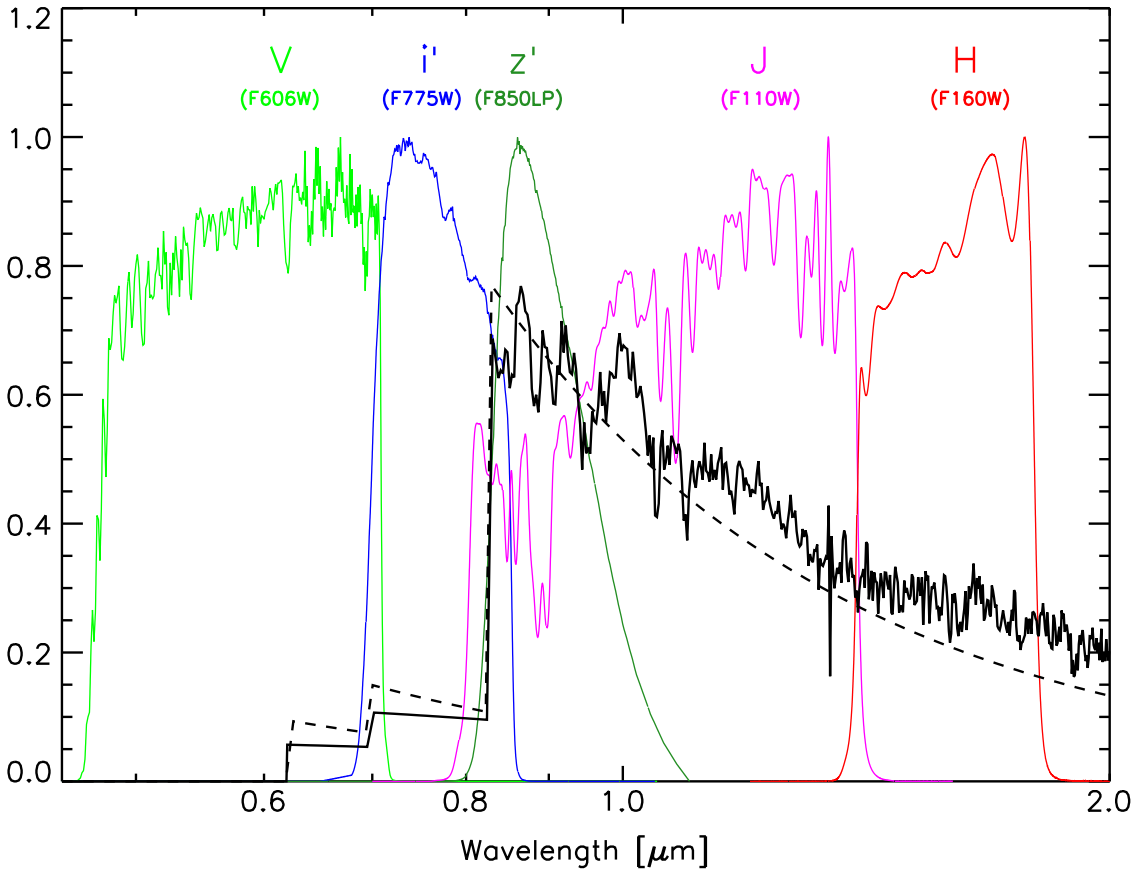

FIG. 1. Normalized transmission profiles of the V, i', z', J, H filters on the *HST*. Overplotted on these are the profiles of a starburst galaxy placed at $z \simeq 5.8$ (solid line; Kinney *et al.* 1996) and also a power-law profile with $f_\lambda \propto \lambda^{-2.0}$ (dashed line). We have applied the Madau (1995) prescriptions to compute the opacity of IGM (between rest-frame 912 Å and 1216 Å) through the mean attenuation factors $\langle D_A \rangle$ and $\langle D_B \rangle$. The Lyman continuum flux below $\lambda_{\rm L}$ is set to zero for both spectra, where $\lambda_{\rm L} = 912$ Å is the Lyman limit.

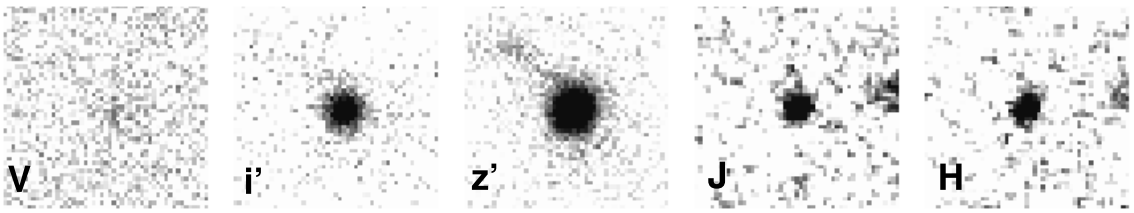

FIG. 2. HUDF 2225 galaxy is spectroscopically confirmed to be at $z \simeq 5.8$, and is a very good example of a dropout galaxy. Here we show its grayscale image in 5 *HST* filters (V,i',z',J,H). The galaxy 'drops-out' completely from the V-band and partially from the i'-band, because the i' filter observations are deepest and more sensitive compared to other filters.

$z \simeq 5.8$ in the HUDF. The majority of the galaxies at $z \gtrsim 4$ are not spectroscopically confirmed in these studies, and are selected purely on the basis of their broad-band colors. This selection can cause the samples to be contaminated by lower redshift, dusty elliptical galaxies and foreground Galactic stars with similar broad-band colors. Details regarding some of the possible interlopers in selecting galaxies at $z \simeq 5-6$ are discussed in the literature (e.g., YWC03; Ryan *et al.* 2005; Yan *et al.* 2008). The candidate galaxies at $z \simeq 5-6$ are comparatively fainter than most interlopers, and most of the major survey fields are located at higher galactic latitudes, where the surface density of galactic stars is very low. Therefore, we expect only a relatively small fraction (<10%; Vanzella *et al.* 2006) of contaminants in the sample of dropouts.

There is presently little information on the dynamical structure/morphology of faint galaxies at $z \gtrsim 4$. It is not clear whether these objects represent isolated disk systems, or collapsing spheroids, mergers or other dynamically young objects. In chapter 2 of this dissertation, we investigate faint high-redshift ($z \simeq 4-6$) dropout galaxies in the HUDF to understand their structure, morphology and stellar populations. In chapter 3, we take a sub-sample of these high redshift dropout galaxies — with spectroscopically confirmed redshifts from the *HST*/ACS low resolution faint grism spectroscopy — and compare their intrinsic physical properties with their lower redshift counterparts.

1.2. *4000 Å Break Selection ($z \simeq 1$)*

The most easily detectable feature in the SED of an old stellar population (evolved stars) — and thus the best option with which to confirm redshifts of com-

paratively older $z \simeq 1$ galaxies (e.g., ellipticals, spiral bulges) — is the 4000 Å break. The 4000 Å break is due to absorption in the atmospheres of stars and arises because of an accumulation of absorption lines of mainly ionized metals and higher-order Balmer lines. As the opacity increases with decreasing stellar temperature, the 4000 Å break gets stronger with older ages. This makes the 4000 Å break a powerful diagnostic in stellar population studies (e.g., Pasquali *et al.* 2006b; Hathi *et al.* 2008c).

Bulges in spiral galaxies were historically thought to be elliptical galaxies that happen to have a disk of stars around them. Recent high resolution images, using *HST*, reveal that many bulges have properties that more closely resemble disk galaxies. It is now thought that there are at least two types of bulges, bulges that are like elliptical galaxies (classical bulges) and bulges that are like disk galaxies (disky bulges or pseudo bulges). Detailed discussion on these two classes of bulges is given in the review by Kormendy & Kennicutt (2004). Based on this differentiation of bulges, there are currently two alternative scenarios to explain bulge formation in galaxies. First, semi-analytic models have traditionally proposed early formation from mergers, generating a scaled-down version of an elliptical galaxy (e.g., Kauffmann *et al.* 1993). Second, dynamical instabilities can contribute to the formation of a bulge within a primordial disk (e.g., Kormendy & Kennicutt 2004). These instabilities can be triggered either internally or by the accretion of small satellite galaxies (Hernquist & Mihos 1995), and may result in later stages of star formation (e.g., Kannappan *et al.* 2004). Hence, studies of the stellar populations in galaxy bulges provide valuable constraints to distinguish between these two scenarios.

The ability of *HST* to spatially resolve distant galaxies enabled the study of bulges in galaxies out to redshift $z \simeq 1$ (Bouwens *et al.* 1999; Abraham *et al.* 1999; Ellis *et al.* 2001; Menanteau *et al.* 2001; Koo *et al.* 2005; MacArthur *et al.* 2008). Based on an analysis of *HST* data on distant galaxies, Bouwens *et al.* (1999) specified three basic bulge formation scenarios: (1) a secular evolution model in which bulges form after disks and undergo several central starbursts; (2) a primordial collapse model in which bulges and disks form simultaneously; and (3) an early bulge-formation model in which bulges form prior to disks. Models 1 and 2 both predict that a large fraction of distance bulges are luminous and relatively blue, while model 3 predicts mainly very red bulges. The advantage of the lookback time probed out to $z \simeq 1$ allows us to quantify the occurrence of merging vs. secular formation of bulges.

In the sample presented in Chapter 4 of this dissertation, we take advantage of the superb capabilities of the *HST*/ACS to extract (slitless) low-resolution spectra of bulges within late-type galaxies (i.e., Hubble types Sb-Sd) to understand their stellar population and how these galaxies assemble at $z \simeq 1$.

This dissertation is organized as follows: the contents of Chapter 2 have appeared as Hathi, N. P., *et al.* 2008, AJ, 135, 156 (copyrighted and published by the American Astronomical Society in January 2008 issue of The Astronomical Journal), while the contents of Chapter 3 have appeared as Hathi, N. P., *et al.* 2008, ApJ, 673, 686 (copyrighted and published by the American Astronomical Society in March 2008 issue of The Astrophysical Journal). The contents of Chapter 4 have been accepted to appear as Hathi, N. P., *et al.* 2008 in the Astrophysical Journal (will be copyrighted

and published by the American Astronomical Society). Chapter 5 summarizes important results of this dissertation and present possible future research directions to be pursued.

2. SURFACE BRIGHTNESS PROFILES AT $z \simeq 4-6$

2.1. *Overview*

The Hubble Ultra Deep Field (HUDF) contains a significant number of B-, V- and i'-band dropout objects, many of which were recently confirmed to be young star-forming galaxies at $z \simeq 4-6$. These galaxies are too faint individually to accurately measure their radial surface brightness profiles. Their average light profiles are potentially of great interest, since they may contain clues to the time since the onset of significant galaxy assembly. We separately co-add V, i'- and z'-band HUDF images of sets of $z \simeq 4, 5$ and 6 objects, pre-selected to have nearly identical compact sizes and the roundest shapes. From these stacked images, we are able to study the averaged radial structure of these objects at much higher signal-to-noise ratio than possible for an individual faint object. Here we explore the reliability and usefulness of a stacking technique of compact objects at $z \simeq 4-6$ in the HUDF. Our results are: (1) image stacking provides reliable and reproducible average surface brightness profiles; (2) the shape of the average surface brightness profile shows that even the faintest $z \simeq 4-6$ objects are *resolved* at the *HST* diffraction limit in the red ($\sim$0.″08 FWHM); and (3) if late-type galaxies dominate the population of galaxies at $z \simeq 4-6$, as previous *HST* studies have shown for $z \lesssim 4$, then limits to dynamical age estimates for these galaxies from their profile shapes are comparable with the Spectral Energy Distribution (SED) ages obtained from the broadband colors. We also present accurate measurements of the sky-background in the HUDF and its associated 1σ uncertainties.

2.2. *Introduction*

In the last decade, ground and space based observations of high redshift galaxies have begun to outline the process of galaxy assembly. The details of that process

at high redshifts, however, remain poorly constrained. There is increasing support for the model of galaxy formation, in which the most massive galaxies assemble earlier than their less massive counterparts (e.g., Cowie *et al.* 1996; Guzman *et al.* 1997; Kodama *et al.* 2004; McCarthy *et al.* 2004). A detailed analysis of the 'fossil record' of the current stellar populations in nearby galaxies selected from the *Sloan Digital Sky Survey* (SDSS; York *et al.* 2000) provides strong evidence for this downsizing picture (Heavens *et al.* 2004; Panter *et al.* 2007). The increasing number of luminous galaxies spectroscopically confirmed to be at $z \simeq 6.5$ (e.g., Hu *et al.* 2002; Kodaira *et al.* 2003; Kurk *et al.* 2004; Rhoads *et al.* 2004; Stern *et al.* 2005; Taniguchi *et al.* 2005), or $\lesssim$0.9 Gyr after the Big Bang, also supports this general picture. In an alternate hierarchical scenario, arguments have been made that significant number of low luminosity dwarf galaxies were present at these times, and were the main contributor to finish the process of reionization of the intergalactic medium (Yan & Windhorst 2004a,b). However, there is presently little information on the dynamical structure of these or other galaxies at $z \simeq 6$. It is not clear whether these objects represent isolated disk systems, or collapsing spheroids, mergers or other dynamically young objects.

Ravindranath *et al.* (2006) used deep, multi-wavelength images obtained with the *Hubble Space Telescope* (*HST*) Advanced Camera for Surveys (ACS) as part of the Great Observatories Origins Deep Survey (GOODS) to analyze 2-D surface brightness distributions of the brightest Lyman-break galaxies (LBGs) at $2.5 < z < 5$. They distinguish various morphologies based on the Sérsic index n, which measures the shape of the azimuthally averaged surface brightness profile (where n=1 for exponential

disks and n=4 for a de Vaucouleurs law). Ravindranath *et al.* (2006) find that 40% of the LBGs have light profiles close to exponential, as seen for disk galaxies, and only $\sim$30% have high n, as seen in nearby spheroids. They also find a significant fraction ($\sim$30%) of galaxies with light profiles *shallower* than exponential, which appear to have multiple cores or disturbed morphologies, suggestive of close pairs or on-going galaxy mergers. Distinction between these possible morphologies and, therefore, a better estimate of the formation redshifts of the systems observed at $z \simeq 4-6$ in particular, is important for testing the galaxy assembly picture, and for the refinement of galaxy formation models.

One possible technique involves the radial surface brightness profiles of the most massive objects — those that will likely evolve to become the massive elliptical galaxies, which we see in place at redshifts $z \lesssim 2$ (Driver *et al.* 1998; van Dokkum *et al.* 2003, 2004). This can be analytically understood in the context of the Lynden-Bell (1967) relaxation formalism and the numerical galaxy formation simulations of van Albada (1982), which describe collisionless collapse and violent relaxation as the formation mechanism for elliptical galaxies. As the time-scale for relaxation is shorter in the inner than in the outer parts of a galaxy, convergence toward a $r^{1/n}$-profile will proceed from the inside to progressively larger radii at later times. Moreover, Kormendy (1977) has shown that tidal perturbations due to neighbors can cause the radial surface brightness profile to deviate from a pure de Vaucouleurs profile in the outer parts of a galaxy. This implies that the radius where surface brightness profiles start to deviate significantly from an $r^{1/n}$ profile *might* serve as a "*virial clock*" that

traces the time since the onset of the last major merger, accretion events or global starburst in these objects.

Image stacking methods have been used extensively on X-ray (Brandt *et al.* 2001; Nandra *et al.* 2002) and radio (Georgakakis *et al.* 2003; White *et al.* 2007) data to study the mean properties (e.g., flux, luminosity) of well-defined samples of sources that are otherwise too faint to be detected individually. Pascarelle *et al.* (1996) applied such a stacking method to a large number of optically very faint, compact objects at $z = 2.39$ to trace their "average" structure. This approach was also applied by Zibetti *et al.* (2004) to detect the presence of faint stellar halos around disk galaxies selected from the SDSS. An attempt to apply this technique to high redshift galaxies in the Hubble Deep Field (HDF; Williams *et al.* 1996) was not conclusive (H. Ferguson; private communication) due to the poorer spatial sampling and shallower depth of the HDF/WFPC2 compared to the HUDF/ACS (Beckwith *et al.* 2006).

For this project, we use the exceptional depth and fine spatial sampling of the HUDF to study the potential of this image stacking technique, and will estimate limits to dynamical ages of faint, young galaxies at $z \simeq 4-6$. The HUDF reaches $\sim$1.5 mag deeper than the equivalent HDF exposure in the i'-band, and has better spatial sampling than the HDF. The HUDF depth also allows us to characterize the sky background very accurately, which is critical for successfully using a stacking method to measure the mean surface-brightness profiles for these faint young galaxies.

Throughout this chapter we refer to the *HST*/ACS F435W, F606W, F775W, and F850LP filters as the B-, V-, i'-, and z'-bands, respectively. We assume a *Wilkin-*

son Microwave Anisotropy Probe (WMAP) cosmology of Ω_m=0.24, Ω_Λ=0.76 and H_0=73 km s^{-1} Mpc^{-1}, in accord with the most recent 3-year WMAP results of Spergel *et al.* (2007). This implies a current age for the Universe of 13.7 Gyr. All magnitudes are given in the AB system (Oke & Gunn 1983).

2.3. *Observations and Sample Selection*

The HUDF contains $\gtrsim$100 objects that are i'-band dropouts, making them candidates for galaxies at $z\simeq6$ (Bouwens *et al.* 2004a, 2006; Bunker *et al.* 2004; Yan & Windhorst 2004b). Similarly, there are larger numbers of objects in the HUDF that are B-band dropouts (415 in total) or V-band dropouts (265 in total), and are candidates for galaxies at $z\simeq4$ and $z\simeq5$, respectively. Beckwith *et al.* (2006) and Bouwens *et al.* (2007) find similar number of B- and V-band dropouts in the HUDF. A significant fraction of these objects to AB$\lesssim$27 mag have recently been spectroscopically confirmed to have redshifts $z\simeq4-6$ through the detection of Lyα emission or identifying their Lyman break (Malhotra *et al.* 2005; Dow-Hygelund *et al.* 2007). We discuss our detailed drop-out selection criteria below. Despite the depth (AB$\lesssim$29.5 mag) of the HUDF images, however, these objects appear very faint and with little, if any, discernible structural detail. Visual inspection of all these objects shows their morphologies to divide into four broad categories: symmetric, compact, elongated, and amorphous.

We construct three separate catalogs for these $z\simeq4,5,6$ galaxy candidates, selecting only the *isolated*, *compact* and *symmetric* galaxies. We exclude objects with obvious nearby neighbors, to avoid a bias due to dynamically disturbed objects

and complications due to chance superpositions. Figure 3 demonstrates that our completeness limit for $z \simeq 4$ and $z \simeq 5$ objects is AB$\lesssim$29.3 mag, and for $z \simeq 6$ objects it is AB$\lesssim$29.0 mag. Therefore, all three catalogs are complete to AB$\lesssim$29.0 mag, which is equivalent to at least a 10σ detection for objects that are nearly point sources. For each object in our $z \simeq 4, 5, 6$ samples, we extracted 51×51 pixel postage stamps (which at $0\farcs03$ pix^{-1} span $1\farcs53$ on a side) from the HUDF V, i' and z'-band images, respectively. Each postage stamp was extracted from the full HUDF, such that the centroid of an object (usually coincident with the brightest pixel) was at the center of that stamp.

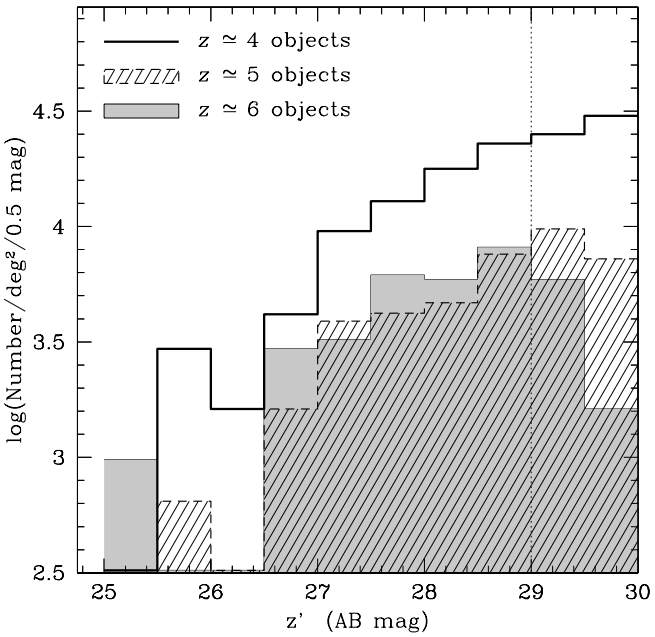

FIG. 3. The HUDF number counts for all $z \simeq 4, 5, 6$ objects before the sub-selection of compact isolated $z \simeq 4, 5, 6$ objects were made. The vertical dotted line shows the magnitude to which the number counts of all these redshifts are complete. The area of the HUDF is 3.15×10^{-3} deg^2.

The $z \simeq 4$ and $z \simeq 5$ objects (B-, V-band dropouts). — We used the i'-band selected $BVi'z'$ HUDF catalog (Beckwith *et al.* 2006) to select the $z \simeq 4$ and $z \simeq 5$ objects. With the `HyperZ` code (Bolzonella *et al.* 2000), we computed photometric redshift estimates, using the magnitudes and associated uncertainties tabulated in

the HUDF catalog. All objects with $3.5 \leq z_{\rm phot} \leq 4.4$ were assigned to the bin of $z \simeq 4$ candidates, and all objects with $4.5 \leq z_{\rm phot} \leq 5.4$ to the bin of $z \simeq 5$ candidates.

We then applied color criteria, similar to those adopted by Giavalisco *et al.* (2004b), to select the $B(z \simeq 4)$ and $V(z \simeq 5)$ dropout samples. For B-band dropouts, we require:

$$\begin{cases} (B-V) \geq 1.2 + 1.4 \times (V-z') \quad \text{mag} \\ \text{and} \quad (B-V) \geq 1.2 \quad \text{mag} \\ \text{and} \quad (V-z') \leq 1.2 \quad \text{mag} \end{cases}$$

For V-band dropouts, the following color selection was applied:

$$\begin{cases} (V-i') > 1.5 + 0.9 \times (i'-z') \ \text{ or } \ (V-i') > 2.0 \quad \text{mag} \\ \text{and} \quad (V-i') \geq 1.2 \quad \text{mag} \\ \text{and} \quad (i'-z') \leq 1.3 \quad \text{mag} \end{cases}$$

We note, that only objects satisfying *both* color *and* photometric redshift criteria were selected in our samples. Vanzella *et al.* (2006) using VLT/FORS2 observed $\sim$100 B-, V- and i'-band dropout objects in the Chandra Deep Field South (CDFS) selected based on above mentioned color criteria (Giavalisco *et al.* 2004b). They have spectroscopically confirmed >90% of their high redshift galaxy candidates. Therefore, we expect only a small number (<10%) of contaminants in our sample of dropouts. One or two objects in our final sample could be such contaminants, but because we have 3 different realizations of 10 objects (3×10), each showing similar profiles, they do not appear to affect our results.

The $z \simeq 4$ sample has 415 objects, while the $z \simeq 5$ sample has 265 objects. In Figure 4ab, we show the distribution of the full-width half maximum (FWHM)

and ellipticity, $\epsilon = (1 - b/a)$, measured in each of the two samples using `SExtractor` (Bertin & Arnouts 1996). We further constrained our samples by imposing limits on compactness and on roundness of FWHM $\leq 0\farcs3$ and $\epsilon \leq 0.3$. Again, this is to minimize the probability that the $z \simeq 4-5$ candidates are significantly dynamically disturbed, and to maximize the probability of selecting physically similar objects. Our goal is to find the visibly most symmetric, least disturbed systems for the current study. This sub-selection leaves 204 objects in the $z \simeq 4$ sample and 102 objects in the $z \simeq 5$ sample. Most of these objects are faint, and are only a few pixels across in size, and, hence, have larger uncertainties in their measurements of FWHM and ellipticity. Therefore, we also checked our objects visually to eliminate any possibility of our selected objects being contaminated by unrelated nearby objects, being clearly extended, or objects with complex morphologies.

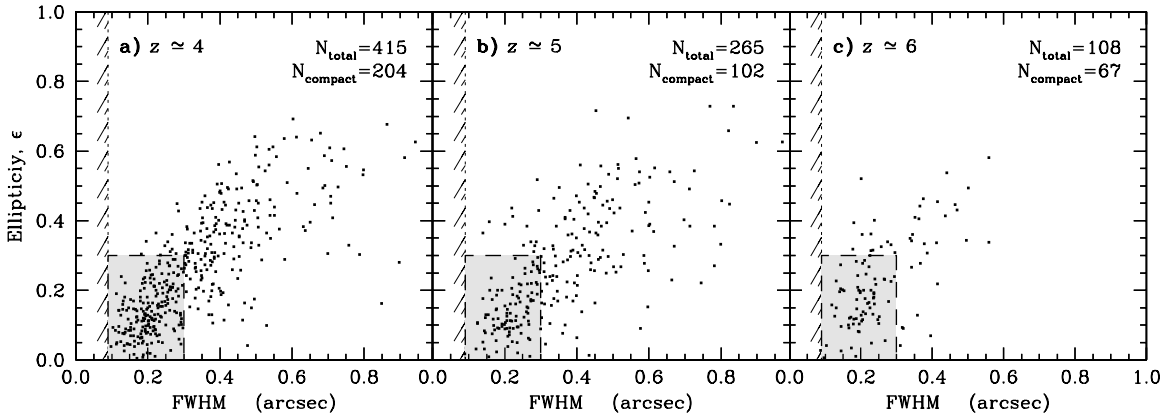

FIG. 4. Ellipticity, $(1 - b/a)$, versus object FWHM, for all $z \simeq 4$ **(a)**, $z \simeq 5$ **(b)** and $z \simeq 6$ **(c)** objects selected in the HUDF. Measurements were performed in i'-band for $z \simeq 4$ and $z \simeq 5$ objects, while we used the z'-band for $z \simeq 6$ objects. The FWHM of a stellar image/PSF is $\sim$3 pixels or $0\farcs09$, indicated by the leftmost hatched area in each panel. Objects within the shaded area meet our additional selection criteria on roundness ($\epsilon \leq 0.3$) and compactness (FWHM $\leq 0\farcs3$ or 10 pixels).

The $z \simeq 6$ objects (i'-band dropouts). — Yan & Windhorst (2004b) found 108 possible $5.5 \leq z \leq 6.5$ candidates in the HUDF to $m_{AB}(z_{850})$=30.0 mag. Bunker *et al.* (2004) independently found the brightest 54 of these 108 $z \simeq 6$ candidates to AB=28.5 mag. Similarly, deep *HST*/ACS grism spectra of the HUDF i'-band dropouts confirm $\gtrsim$90% of these objects at AB$\lesssim$27.5 mag to be at $z \simeq 6$ (Malhotra *et al.* 2005; Hathi *et al.* 2008a). Using the catalog of Yan & Windhorst (2004b), we extracted 108 postage stamps (51×51 pixels in size), from the HUDF z'-band image.

Like for the $z \simeq 4$ and $z \simeq 5$ objects, for each $z \simeq 6$ object we measured its z'-band FWHM and ellipticity using `SExtractor`. Figure 4c shows the measured ellipticity versus FWHM for all 108 $z \simeq 6$ candidates. A smaller sample of 67 objects satisfies our constraints on the FWHM and ellipticity. Further visual inspection, to make sure that our sample has only isolated, compact and round objects, leaves 30 objects in our $z \simeq 6$ sample. We therefore imposed a sample size of 30 objects also on the two lower redshift bins after visual inspection.

The results in this project are therefore based on approximately (30/415)∼7%, (30/265)∼11%, and (30/108)∼28% of the total $z \simeq 4, 5$ and 6 galaxy populations.

2.4. *The HUDF Sky Surface-Brightness Level*

For the present work, it is *critical* that we accurately characterize the sky-background, and correctly propagate the true 1σ errors due to the subtraction of this sky-background. In the following, we will pursue two complimentary approaches to determine the sky surface-brightness, and compare the results. Here, we discuss the z'-band measurements in detail.

We first measured the sky-background in each of the 415 $z \simeq 4$ object stamps ('local' sky measurements). The Interactive Data Language (IDL[1]) procedure `SKY`[2] was used to measure the sky-background. This procedure is adapted from the `DAOPHOT` (Stetson 1987) routine of the same name and works as follows. First, the average and sigma are obtained from the sky pixels. Second, these values are used to eliminate outliers with a low probability. Third, the values are then recomputed and the process is repeated up to 20 iterations. If there is a contamination due to an object, then the contamination is estimated by comparing the mean and median of the remaining sky pixels to get the true sky value. The output of this procedure is the modal sky-level in the image.

Figure 5c shows a histogram of the z'-band modal sky values obtained from all 415 object stamps extracted from the drizzled HUDF images. The 1σ uncertainty in the sky, $\sigma_{\rm sky}$, determined from a Gaussian fit to the histogram, is 2.19×10^{-5} electrons sec^{-1} in the z'-band. The sky-background level within the HUDF was obtained from the original flat-fielded ACS images, because the final co-added HUDF data products are sky-subtracted. The header parameters MDRIZSKY and EXPTIME were used to obtain the actually observed sky-value. MDRIZSKY is the sky value in electrons (e^-) computed by the MultiDrizzle code (Koekemoer *et al.* 2002), while EXPTIME is the total exposure time for the image in seconds, so that the average sky-value in the HUDF has the units of e^- sec^{-1}. Figure 6d shows the histogram of the sky-values obtained from 288 HUDF z'-band flat-fielded exposures. The average value of the sky

[1]IDL Website http://www.ittvis.com/index.asp

[2]Part of the IDL Astronomy User's Library, see: http://idlastro.gsfc.nasa.gov/homepage.html

background, I_{sky}, is 0.02051 e^- sec^{-1}. That sky-value is measured from the flat-fielded individual ACS images with pixel sizes of 0.″050 pix^{-1} and hence, in the following calculations, the average sky-value is multiplied by a factor of $(0.030/0.05)^2$=0.60^2 to obtain the corresponding average sky-value for the HUDF drizzled pixel size of 0.″030 pix^{-1}. Using these values, we estimate the relative rms random sky-subtraction error as follows:

$$\Sigma_{ss,ran} = \frac{\sigma_{sky,ran}}{I_{sky}} = \frac{2.19 \times 10^{-5}}{2.05 \times 10^{-2} \ \cdot \ 0.60^2} = 2.97 \times 10^{-3}$$

The measured average sky background level can then be expressed as the z'-band sky surface brightness as follows:

$$\mu_{z'} = 24.862 - 2.5 \cdot \log\left(\frac{0.0205 \ \cdot \ 0.60^2}{0.030^2}\right) = 22.577 \pm 0.003 \text{ mag arcsec}^{-2}$$

where 24.862 is the ACS/WFC z'-band AB zero-point, and 0.″030 pixel^{-1} is the drizzled pixel scale. This is consistent with the values obtained by extrapolating the on-orbit BVI sky surface brightness of Windhorst *et al.* (1994, 1998) to z', with the sky-background estimates from the ACS Instrument Handbook (Gonzaga *et al.* 2005), and with the colors obtained by convolving the filter transmission curves with the solar spectrum. Table 1 and Table 2 gives the measured electron detection rate, surface brightness and colors of the sky background with their corresponding errors for the HUDF $BVi'z'$ bands as calculated from Figure 5 and Figure 6. The contribution of the zodiacal background dominates the total sky-background, which we find to be only ∼10% redder in (V–i') and (i'–z') than the Sun. The z'-band surface brightness corresponding to the 1σ sky-subtraction uncertainty is therefore:

$$\mu_{z'} - 2.5 \cdot \log(\Sigma_{ss,ran}) = 22.577 - 2.5 \cdot \log(2.97 \times 10^{-3}) = 28.895 \text{ mag arcsec}^{-2}$$

Next, we measure the sky-background from 415 '*blank*' sky stamps (51×51 pixel) distributed throughout the HUDF ('global' sky measurements). We measure the sky background using the same IDL algorithm as used above.

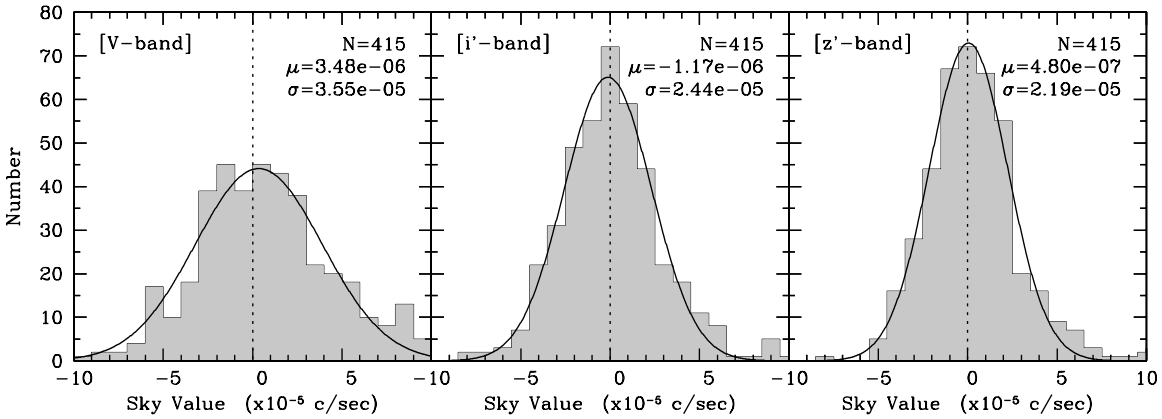

FIG. 5. Distribution of the modal sky background level used to estimate the 1σ uncertainty in that level, as measured in the 415 $z \simeq 4$ *object stamps* extracted from the drizzled HUDF images **(a)** for V-band, **(b)** for i'-band, and **(c)** for z'-band. The mean (μ) and the sigma (σ) of the best-fit Gaussian to these distributions are also shown in each panel.

Figure 7c shows the histogram of the measured z'-band modal sky values. A Gaussian distribution was fit to this histogram, giving a sky-sigma of 2.00×10^{-5} e^- sec^{-1}. The average value of the sky remains 0.02051 e^- sec^{-1} (Figure 6d). Using these values, we can estimate a relative rms systematic sky-subtraction error as follows:

$$\Sigma_{\rm ss,sys} = \frac{\sigma_{\rm sky,sys}}{\rm I_{sky}} = \frac{2.00 \times 10^{-5}}{2.05 \times 10^{-2} \ \cdot \ 0.60^2} = 2.71 \times 10^{-3}$$

Since the z'-band sky surface brightness remains 22.577 mag arcsec^{-2}, this gives us for the surface brightness corresponding to the 1σ sky subtraction uncertainty:

$$\mu_{z'} - 2.5 \cdot \log(\Sigma_{\rm ss,sys}) = 22.577 - 2.5 \cdot \log(2.71 \times 10^{-3}) = 28.995 \text{ mag arcsec}^{-2}$$

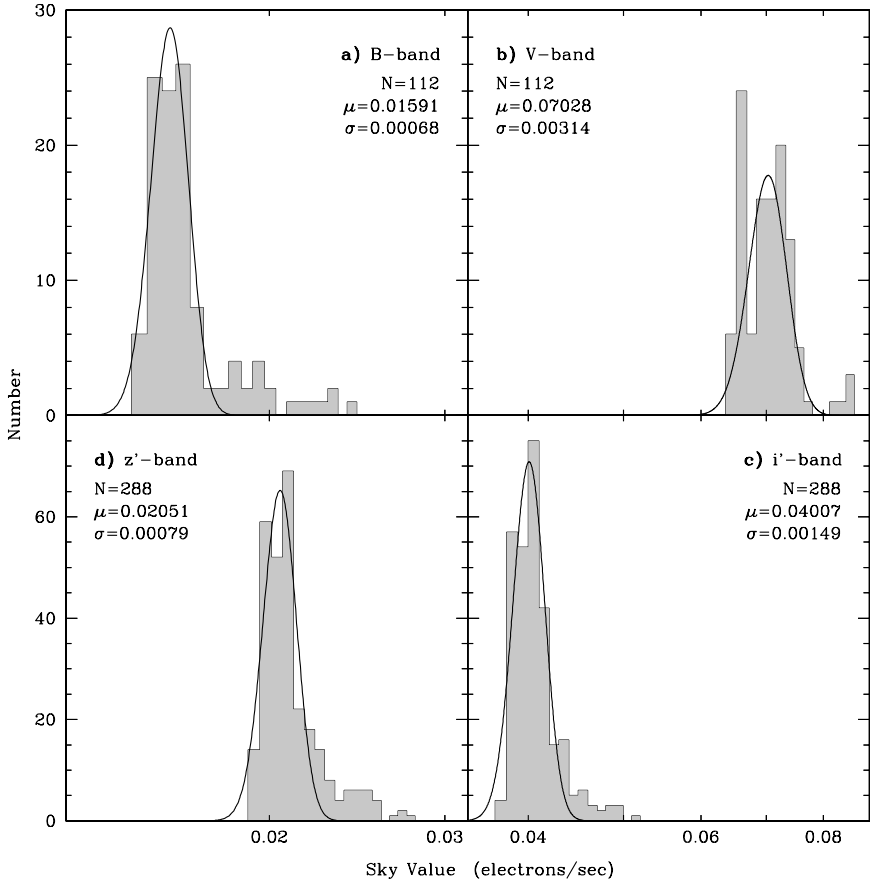

FIG. 6. The *actual sky values* measured using header parameters MDRIZSKY and EXPTIME from flat-fielded HUDF exposures. **(a)** For B-band using 112 exposures. **(b)** For V-band using 112 exposures. **(c)** For i'-band using 288 exposures. **(d)** For z'-band using 288 exposures. The mean (μ) and the sigma (σ) of the best-fit Gaussian to these distributions are shown in each panel.

From these two complementary approaches, we can conclude that all surface brightness measurements become unreliable for surface brightness levels fainter than 28.95 $\pm$ 0.05 mag arcsec^{-2} in the z'-band. We have also experimented with slightly larger cutouts (75×75 pixels instead of 51×51 pixels) to estimate the sky-subtraction error. We find that with the larger cutouts, the surface brightness corresponding to the 1σ sky-subtraction error is $\sim$0.1–0.2 mag arcsec^{-2} fainter. For larger cutouts we expect this surface brightness to be $\sim$0.4 mag fainter, but we find about 0.1–0.2 mag fainter.

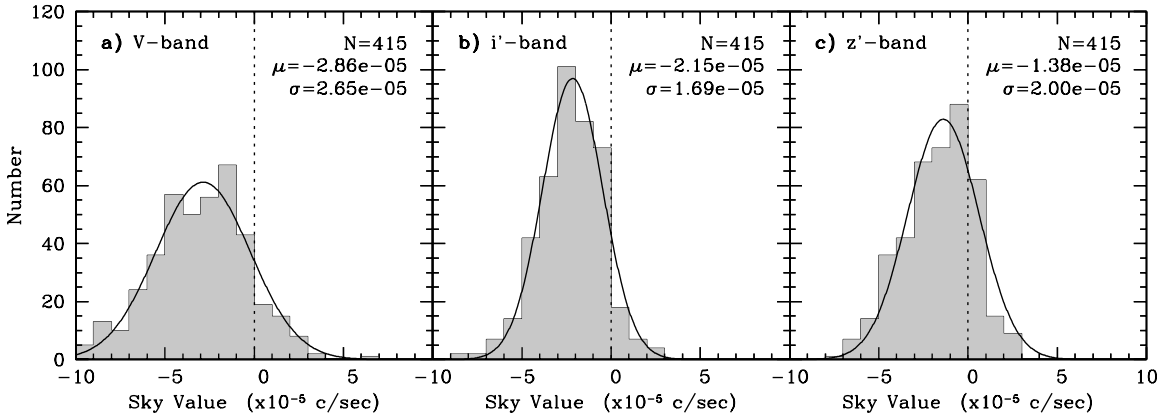

FIG. 7. Distribution of the modal sky background level used to estimate the 1σ uncertainty in that level, as measured in 415 *'blank' 51×51 pixel sky stamps* extracted from the drizzled HUDF images **(a)** for V-band, **(b)** for i'-band, and **(c)** for z'-band. The mean (μ) and the sigma (σ) of to the best-fit Gaussian to these distributions are shown in each panel.

This might be because of low-level large scale residual systematic sky-errors in the HUDF images. Therefore, we are at the limit of accurately measuring this surface brightness and hence, we will here quote the conservative brighter limit of the surface brightness corresponding to this 1σ sky-subtraction error. Expected contributions to this surface brightness due to uncertainties in the bias level determinations, which correspond to $\sim$0.001 counts sec^{-1} for typical HUDF exposures (A. M. Koekemoer; private communication), are less than 1%.

Figure 7 clearly shows that the distribution of the modal sky-values is not as symmetric around zero as in Figure 5, and hence, the use of a 'global' sky value for the HUDF is not as reliable as 'local' sky measurements. Therefore, for the surface brightness profiles and the following discussion, we will adopt the *local* 1σ random sky-subtraction error for all objects in our study.

The average modal sky values and their 1σ errors in the V- and i'-bands were calculated in exactly the same way as for the z'-band, as shown in Figure 5, 6 and 7. The resulting $BVi'z'$ sky values and the sky surface-brightness levels are all given in Table 1 and Table 2, respectively.

TABLE 1: Measured Sky Values in HUDF $BVi'z'$ Filters

HUDF Filter	Number of Exposures	Mean Sky Value[a] (e^-/s) and rms error[b]
B	112	0.015909 ± 0.000065
V	112	0.070276 ± 0.000297
i'	288	0.040075 ± 0.000088
z'	288	0.020511 ± 0.000047

[a] From Figure 6

[b] Error is standard deviation of the mean ($\sigma/\sqrt{N}$)

2.5. *Composite Surface Brightness Profiles*

For each redshift bin ($z \simeq 4, 5, 6$), we generated three "stacked" composite images from subsets of 10 postage stamps that were selected as follows. After placing all 30 image stamps per redshift bin into a 30× (51×51) pixel IDL array, 10 stamps were randomly drawn without selecting any object more than once. An output image was generated, in which the values at each pixel are the average of the corresponding pixels in the 10 selected input stamps. From the remaining 20 stamps, we again randomly select 10, from which we generated a second composite image, after which the final 10 images were averaged into the third composite image. The three composite images per redshift bin are therefore independent of each other. In none of our realizations did we produce composite images that were essentially unresolved. Even

the faintest $z \simeq 4-6$ galaxies are clearly resolved. The $z \simeq 4, 5, 6$ objects used to generate the composite images have an apparent magnitude range of approximately 27.5±1.0 AB mag. Because the magnitude range is relatively small and the S/N per pixel is low even in their central pixel, we have given all objects equal weight.

TABLE 2: Measured Sky Surface Brightness in HUDF

HUDF Filter	Sky SB[a] (AB mag arcsec^{-2})	Sky Color[a] (AB mag)	1σ Sky-Subtraction error (AB mag arcsec^{-2})
B	23.664 ± 0.003	$(B-V)_{\rm sky}$=0.800	29.85 ± 0.05
V	22.864 ± 0.002	$(V-i')_{\rm sky}$=0.222	30.15 ± 0.15
i'	22.642 ± 0.002	$(i'-z')_{\rm sky}$=0.065	29.77 ± 0.20
z'	22.577 ± 0.003	$(V-z')_{\rm sky}$=0.287	28.95 ± 0.05

[a] Sky surface brightness values and colors are consistent with the solar colors in AB mag of (V-i')=0.19, (V-z')=0.21 and (i'-z')=0.01 [except for bluest color (B-V)], and is dominated by the zodiacal background.

To test whether this range in magnitude will affect our stacks and hence, our profiles, we created 3 stacks depending on the apparent magnitude, i.e., one stack of the 10 brightest objects in the sample, a second stack of the 10 next brightest objects in the sample and a third stack of the 10 faintest objects in the sample. This is summarized in Figure 8d. We found that the profiles were very similar except that the profiles of the fainter stacks fall-off more quickly at larger radius compared to the profile of the brightest stack, but the inner profile and the deviation in the profiles are clearly visible in all 3 stacks. Therefore, we conclude that for our range in apparent magnitudes, our stacks/profiles are not affected. Perhaps most surprisingly, Figure 8d shows that r_e value of all 3 flux ranges (∼26.0–27.0, ∼27.0–28.0 & ∼28.0–

29.0 mag) are all about the same over ∼3-4 mag in flux, so the primary parameter that distinguishes the brighter from the fainter $z \simeq 6$ dropouts is their central surface brightness (which thus also varies by ∼3–4 mag).

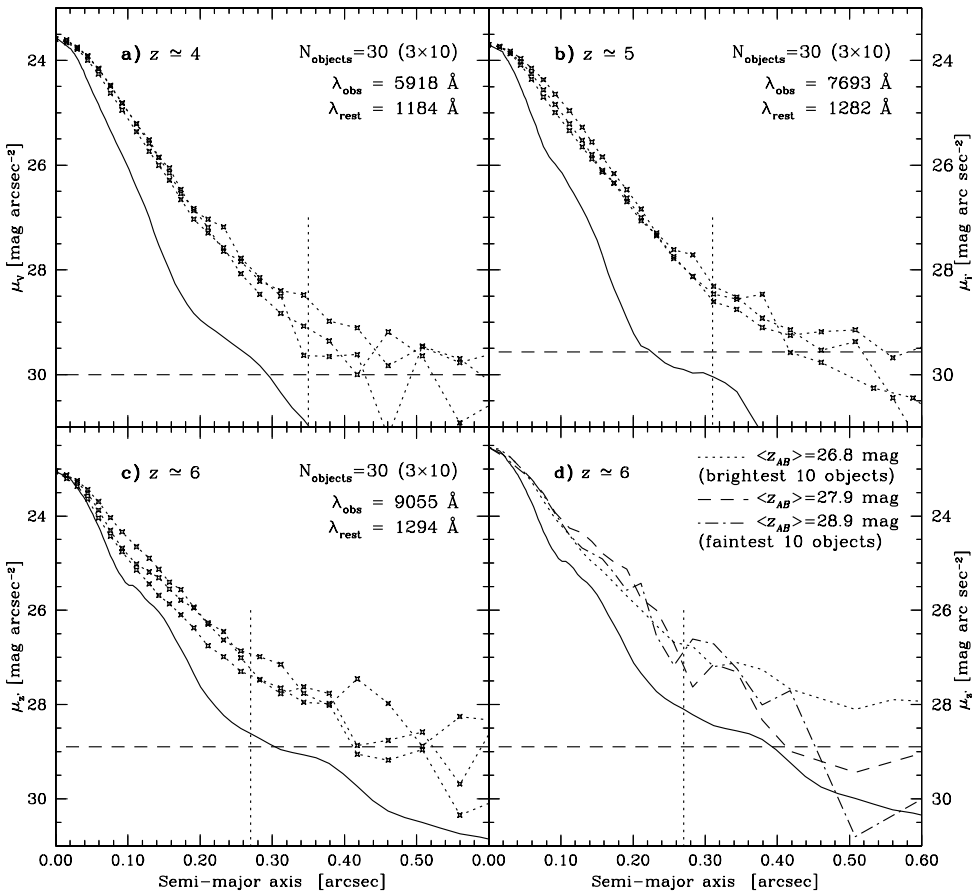

FIG. 8. Composite surface brightness profiles for three independent sets of 10 objects at **(a)** $z \simeq 4$, **(b)** $z \simeq 5$ and **(c)** $z \simeq 6$, respectively. The thin solid curve represents the ACS V, i' and z'-band PSFs, respectively, while the horizontal dashed line indicates the surface brightness level corresponding to the 1σ sky–subtraction error in the HUDF images. The vertical dotted line marks the radius at which the profile starts to deviate significantly from the extrapolation of the inner $r^{1/n}$ profile observed at smaller radii. Note that at $z \simeq 6$, this deviation is still well above the red z'-band PSF halo at $r \gtrsim 0\farcs30$. The panel **(d)** shows 3 $z \simeq 6$ composite profiles (each with a set of 10 objects) divided by apparent magnitudes. The brightest composite profile (dotted) has an average z'-band magnitude of ∼26.8 mag. The next brightest composite profile (short dash) has an average z'-band magnitude of ∼27.9 mag, and the faintest composite profile (dot-dash) has an average z'-band magnitude of ∼28.9 mag.

We used the IRAF[3] procedure `ELLIPSE` to fit surface brightness profiles shown in Figure 8 to each of the three independent composite images per redshift bin. We also computed a mean surface-brightness profile from the three composite surface brightness profiles generated from the three independent composite images for each redshift bin. Figure 9 shows composite images for $z \simeq 4, 5, 6$ objects. Here each composite image is a stack of 30 objects. Figure 10 shows the average surface brightness profiles for each of the redshift intervals $z \simeq 4, 5, 6$. The thin solid curves in Figure 8 and the dot-dash curves in Figure 10 represent the observed ACS V, i' and z'-band Point Spread Functions (PSFs), while the horizontal dashed lines indicate the surface brightness level corresponding to the 1σ sky–subtraction error in each of the HUDF images. It is important to note that we scaled the ACS PSFs to match the surface brightness of the central data point in our mean surface-brightness profile, to determine how extended the mean surface-brightness profile is with respect to the PSFs.

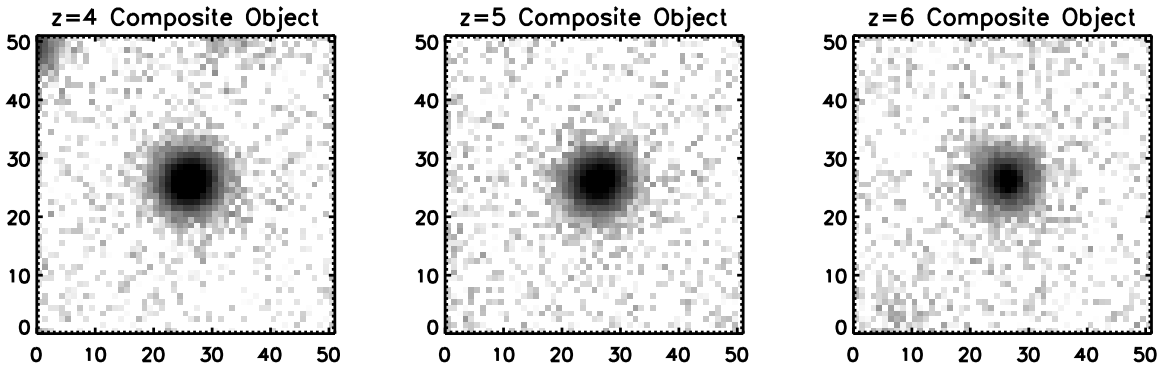

FIG. 9. Composite images for **Left** $z \simeq 4$, **Center** $z \simeq 5$ and **Right** $z \simeq 6$ objects. Here each composite image is a stack of 30 objects. Each stamp is 1.″53 on a side.

[3]IRAF (http://iraf.net) is distributed by the National Optical Astronomy Observatories, which are operated by the Association of Universities for Research in Astronomy, Inc., under cooperative agreement with the National Science Foundation.

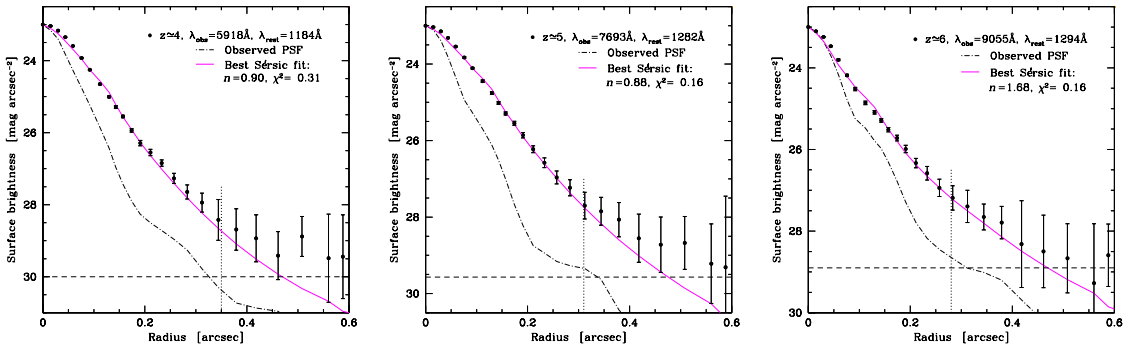

(a) For $z \simeq 4$ objects. (b) For $z \simeq 5$ objects. (c) For $z \simeq 6$ objects.

FIG. 10. Mean surface brightness profiles with a best fit Sérsic profiles for 30 composite images at $z \simeq 4$–6. The thin dot-dash curve represents the ACS V-, i'-, z'-band PSFs, respectively, while the horizontal dashed line indicates the surface brightness level corresponding to the 1σ sky–subtraction error in the HUDF images. The vertical dotted line marks the radius at which the profile starts to deviate significantly from the extrapolation of the inner $r^{1/n}$ profile observed at smaller radii. The n is the best fit Sérsic index.

In Figure 10, we fitted all possible combinations of the Sérsic profiles (convolved with the ACS PSF) to the observed profiles and using χ^2 minimization, found the best fits for galaxies at $z \simeq 4, 5, 6$. The best fit Sérsic index (n) for all three profiles ($z \simeq 4, 5, 6$) is $n < 2$, meaning these galaxies follow mostly exponential disk-type profiles in their central regions. We find that the observed profiles start to deviate from the best-fit profiles at $r \gtrsim 0\farcs27$, somewhat depending on the redshift. From Figure 10, we also see that in each of V ($z \simeq 4$), i' ($z \simeq 5$) and z' ($z \simeq 6$), the PSF declines more rapidly with radius than the composite radial surface brightness profile for $r \gtrsim 0\farcs27$. It is therefore unlikely that the observed 'breaks' result from the halos and structure of the ACS PSFs. Specifically, at $z \simeq 6$ the most significant deviations in the light-profiles are seen at levels 1.5–2.0 mag above the 1σ sky-subtraction error, and well above the PSF wings. Each of the mean surface brightness profiles display

a well-defined break, the radius of which appears to change somewhat with redshift. These results are tabulated in Table 3. The vertical dotted lines (in Figure 8 and Figure 10) mark the radius at which the mean surface brightness profiles start to deviate significantly from the extrapolation of the $r^{1/n}$ profile observed at smaller radii.

TABLE 3: Dynamical Ages for $z \simeq 4-6$ Objects

Redshift z	"Break" Radius[a] (arcsec)	"Break" Radius[b] (kpc)	Dynamical Age[c] (τ_{dyn})
4	0.35	2.5	0.09–0.29 Gyr
5	0.31	2.0	0.07–0.21 Gyr
6	0.27	1.6	0.05–0.15 Gyr

[a] From composite surface brightness profiles (Figure 8 and Figure 10).

[b] Radius in kpc corresponding to radius in arcsec at given redshift.

[c] If "break radius" interpreted as indicator of dynamical age.

Test of the stacking technique on nearby galaxies. — To test the general validity of the stacking technique itself on a local galaxy sample, we used surface photometry from the Nearby Field Galaxy Survey (NFGS: Jansen *et al.* 2000a,b). The NFGS sample contains 196 nearby galaxies, that were objectively selected from the CfA redshift catalog (CfA I; Davis & Peebles 1983; Huchra *et al.* 1983) to span the full range in absolute B magnitude present in the CfA I ($-14.7 \lesssim M_B \lesssim -22.7$ mag). The absolute magnitude distribution in the NFGS sample approximates the local galaxy luminosity function (e.g., Marzke *et al.* 1994), while the distribution over Hubble type follows the changing mix of morphological types as a function of luminosity in the local

galaxy population. The NFGS sample (as detailed in Jansen *et al.* 2000a) minimizes biases, and yields a sample that, with very few caveats, is representative of the local galaxy population. As part of the NFGS, UBR surface photometry, both integrated (global) and nuclear spectrophotometry, as well as internal kinematics were obtained (see Jansen & Kannappan 2001). Here, we will concentrate on the U-band surface photometry, since it is closest in wavelength to the rest-frame wavelengths observed at $z \simeq 4-6$. Although, ideally, we would want a filter further into the UV, Taylor-Mager *et al.* (2007) and Windhorst *et al.* (2002) show that for the majority of late-type nearby galaxies, the apparent structure of galaxies does not change dramatically once one observes shortward of the Balmer break. Early-type galaxies, however, are a clear exception to this, but these are not believed to dominate the galaxy population at $z \simeq 4-6$, as discussed before.

Figure 11 shows stacked profiles for relatively luminous early-, spiral-, and late-type galaxies drawn from the NFGS. Vertical dotted lines indicate the half-light radii and their intersection with the profiles, the surface brightness at that radius. Dashed lines indicate exponential fits to the outer portion of each profile. Figure 11 also shows that co-adding profiles for disparate morphological types and for mid-type spiral galaxies with a range in bulge-to-disk ratios can produce breaks in the composite profile. No such breaks are seen when the profiles of either early-type galaxies (E, S0) or late-type galaxies (Sd–Irr) are co-added. This figure shows that, *if* galaxies at $z \simeq 4-6$ had similar morphological types as local galaxies, then it would be possible to produce a break in the profiles (as shown in Figure 8 and Figure 10), merely by

mixing different types of galaxies. We do not believe that the galaxy populations at $z \simeq 4$–6 morphologically resemble those at low redshift. Hence, for primarily late-type galaxies, which dominate the faint blue galaxy population at AB≥24 mag (Driver *et al.* 1998), and which likely dominate the fainter end of the luminosity function at $z \simeq 4$–6 that we sample here (Yan & Windhorst 2004a,b), the image stacking is likely a valid exercise.

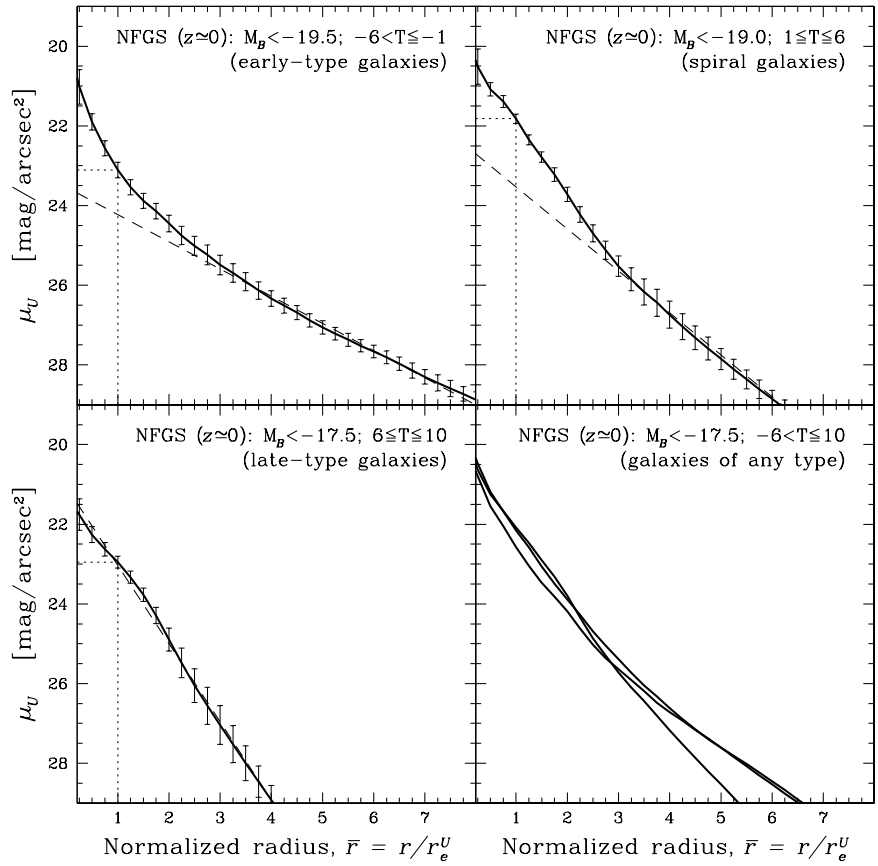

FIG. 11. Stacked radial surface brightness profiles for relatively luminous early-, spiral- and late-type nearby galaxies drawn from the Nearby Field Galaxy Survey (Jansen *et al.* 2000a,b). The vertical dotted line indicates the half-light radius, while the dashed line represents an exponential fit to the outer portions of each composite profile. Co-adding profiles for disparate morphological types and for spiral galaxies with a range in bulge-to-disk ratios can produce breaks in the composite profile. No significant breaks are seen in the *outer* light profiles, when the profiles of either early-type galaxies (E, S0) or late-type galaxies (Sd–Irr) are co-added.

The primary goal of this section was to show that the profile stacking technique is valid and can be used to get meaningful surface brightness profiles. We are not comparing our nearby sample with galaxies at $z \simeq 4-6$. These nearby galaxies are unlikely to be local analogues of high redshift galaxies. If we apply surface brightness dimming to UV light-profiles of these nearby galaxies, they would be mostly invisible to *HST*, and in some cases visible to the *James Webb Space Telescope* (*JWST*; see e.g., Windhorst *et al.* 2006). This is another way of saying that the $z \simeq 4-6$ objects are truly different from $z \simeq 0$ objects.

2.6. *Discussion*

Figure 10 shows that the mean surface brightness profiles deviate significantly from an inner $r^{1/n}$ profile at radii $r \gtrsim 0\farcs27$–$0\farcs35$, depending somewhat on the redshift bin. These deviations appear real, with the break/point of departure located $\gtrsim$1.5–2 mag above the 1σ sky-subtraction error and above the PSF-wings. In the following, we discuss several possible explanations for the observed shapes of our composite surface brightness profiles.

Galaxies with different morphologies. — Our test on nearby galaxies (Figure 11) shows that, if we stack many galaxies with different morphologies (early-type, late-type or spiral galaxies), it is possible to get a slope-change ('break') in the average surface brightness profile. Ravindranath *et al.* (2006) find that 40% of the brighter LBGs at $2.5 < z < 5$ have light profiles close to exponential, as seen for disk galaxies, and only ∼30% have high n, as seen in nearby spheroids. They also find a significant fraction (∼30%) of galaxies with light profiles *shallower* than exponential,

which appear to have multiple cores or disturbed morphologies, suggestive of close pairs or on-going galaxy mergers. Therefore, if faint galaxies at $z \simeq 4$–6 have a variety of morphological types, then the shape of the average surface brightness profile that we see may be due to the stacking of different types of galaxies. Therefore, we find that the exponential and the flatter profiles found by Ravindranath *et al.* (2006) for galaxies at $2.5 < z < 5$ also apply to higher redshifts ($z \geq 5$).

Also, we believe that it is more likely that the high redshift, faint galaxy population consists primarily of small galaxies with late-type morphologies and with sub-L* luminosities, as seen at $z \simeq 2-3$ (Driver *et al.* 1995, 1998). So if the $z \simeq 4-6$ population consists of such a late-type galaxy population, then the slope-change in the light profiles is likely not the result of co-adding images of objects with disparate morphological types.

Central star formation/starburst. — HST optical images of galaxies at $z \simeq 4$–6 sample their rest-frame UV ($\sim$1200 Å), where the contribution from the actively star-forming regions (young, massive stars) dominates the UV-light. Hathi *et al.* (2008a) have shown that galaxies at $z \simeq 5$–6 are high redshift starbursts with similar starburst intensity limit as local starbursting galaxies. Therefore, it is possible that galaxies at $z \simeq 4-6$ have centrally concentrated star formation or starburst. This possibility is based on three key assumptions: (1) most of the galaxies at $z \simeq 4, 5, 6$ are intrinsically later-type galaxies (Steidel *et al.* 1999); (2) the SED of these galaxies at $z \simeq 4, 5, 6$ are dominated by early A- to late O-type stars, respectively; and (3) there are no old stars with ages at $z \simeq 4-6$ greater than 2-1 Gyr in WMAP cosmology, respectively.

Hunter & Elmegreen (2006) studied azimuthally averaged surface photometry profiles for large sample of nearby irregular galaxies. They find some galaxies have double exponentials that are steeper (and bluer) in the inner parts compared to outer parts of the galaxy. Hunter & Elmegreen (2006) discuss that this type of behavior is expected in galaxies, where the centrally concentrated star formation or starburst steepens the surface brightness profiles in the center. If that is the case, then one might expect a better correlation between the break in the surface brightness profiles and changes in color profiles. Unfortunately, for our sample of galaxies at $z \simeq 4-6$, we don't have high- resolution restframe UBVcolor information. The objects are generally too faint for *Spitzer Space Telescope*, and hence we cannot confirm or reject this possibility for the shape of our composite surface brightness profiles.

Limits to dynamical ages for $z \simeq 4, 5, 6$ objects. — The average compact $z \simeq 4$–6 galaxy is clearly extended with respect to the ACS PSFs (Figure 10), and is best fit by an exponential profile ($n < 2$) out to a radius of about $r \simeq 0\farcs35$, $0\farcs31$, and $0\farcs27$ at $z \simeq 4, 5$ and 6, respectively. The apparent progression with redshift is noteworthy. The radius at which the profile starts to deviate from $r^{1/n}$ (in this case at radius $r \gtrsim 0\farcs35$–$0\farcs27$) may put an important constraint to the dynamical time scale of these systems. If this argument is valid, then we can estimate limits to the dynamical ages of $z \simeq 4, 5, 6$ galaxies as follows.

In WMAP cosmology, a radius of $r \gtrsim 0\farcs35$ at $z \simeq 4$ corresponds to $r \gtrsim 2.5$ kpc. The dynamical time scale (e.g., Binney & Tremaine 1987), τ_{dyn}, goes as $\tau_{dyn} = C r^{3/2}/\sqrt{G\,M}$, where the constant $C = \pi/2$. For a typical dwarf galaxy mass range

of $\sim 10^9 - 10^8$ $M_\odot$ inside r=2.5 kpc, we infer that the limits to the dynamical age would be $\tau_{dyn} \simeq$ 90–290 Myr, which is the lifespan expected for a late-type B-star. This means that the last major merger that affected this surface brightness profile and that triggered its associated starburst may have occurred $\sim$0.20 Gyr before $z \simeq 4$, —assuming that the star-formation was not spontaneous, but associated with some accretion or a merging event.

Table 3 shows the break-radius and inferred limits to dynamical ages for the $z \simeq 4-6$ objects. At $z \simeq 5$, we find that the limits to dynamical age at the break radius would be $\tau_{dyn} \simeq$ 70–210 Myr, which is the lifespan expected for a mid B-star, while at $z \simeq 6$, $\tau_{dyn} \simeq$ 50–150 Myr, which is the lifespan expected for a late O–early B-star. This means that the last major merger that affected these surface brightness profiles at $z \simeq 5$ and 6 and that triggered its associated starburst may have occurred $\sim$0.14 and $\sim$0.10 Gyr before $z \simeq 5$ and 6, respectively.

The dynamical time is a lower limit to the actual time available, since it assumes matter starts from rest. Any angular momentum at start will increase the available time. The best-fit SED age from the GOODS *HST* and *Spitzer* photometry on some of the brighter of these objects — using Bruzual & Charlot (2003) templates — is in the range of about $\sim$150–650 Myr (Yan *et al.* 2005; Eyles *et al.* 2005, 2007), the lower end of which is consistent with our limits to their dynamical age estimates, while the somewhat larger SED ages could also be affected by the onset of the AGB in the stellar population increasing the observed *Spitzer* fluxes and hence possibly overestimating ages (Maraston 2005). Our age estimates for $z \simeq 4-6$ are consistent

with the trend of SED ages suggested for $z \simeq 7$ (Labbé *et al.* 2006). It is noteworthy that, given the uncertainties, the two independent age estimates are consistent. If our limits to dynamical age estimates for the image *stacks* are thus valid, they are consistent with the SED ages, and point to a consistent young age for these objects.

Furthermore, the presence of young, massive late O–early B-stars at $z \simeq 6$ has implications for the reionization of the universe. From observations of the appearance of complete Gunn-Peterson troughs in the spectra of $z \gtrsim 5.8$ quasars (Fan *et al.* 2006), we know that the epoch of reionization had ended by $z \simeq 6$. From the steep (α=–1.8) faint-end slope of the luminosity function of $z \simeq 6$ galaxies, Yan & Windhorst (2004a,b) concluded that dwarf galaxies, and not quasars, likely finished reionization by $z \simeq 6$. Should the present interpretation of their light profiles be correct, then it would appear to add support to this picture, in the sense that such objects are dominated by B-stars and did not start their most recent major starburst long before $z \simeq 6$. It is the same global starburst that would have finished reionization by $z \simeq 6$.

2.7. *Looking Towards the Future (JWST Science)*

The results of this project are based on composite images of compact galaxies in the HUDF at $z \simeq 4-6$. Composite images were generated to increase signal-to-noise (S/N) ratio of faint individual galaxies. Such a composite would effectively correspond to a single galaxy detectable at a much higher S/N ratio, equivalent to ∼4500 *HST* orbits (∼3000 hrs) on a single such object. It will be very difficult to improve this analysis using the *HST* in next few years. The *James Webb Space Telescope* (*JWST*) will observe very distant galaxies ($z \gtrsim 6$) in the observed near-mid

infrared (IR) wavelengths after its launch in 2013. *JWST* will be very critical to understand structure/morphologies of these faint galaxies at $z \gtrsim 4-6$. *JWST* will accomplish such a high S/N observations for faint galaxies at $z \simeq 4-6$ in $(1/12)^{th}$ of the time compared to current capabilities (see e.g., Windhorst *et al.* 2008). Therefore, the 6.5 meter *JWST* will confirm and improve our results at 1 micron in 250 hours of *JWST* deep imaging as a single object. *JWST* will also enable such analysis on accuracy of sky background and composite images for galaxies at much higher redshift ($z \simeq 7-15$). We will be able to characterise *JWST* measured sky-background and its uncertainties very carefully, as we have done in this project with the HUDF. *JWST*'s smaller pixel size, darker sky (due to its L2 orbit) and observed near to mid-infrared wavelengths will help tremendously to make such a structural study for very first galaxies around $z \simeq 10-15$. It is very important to understand what type of morphological structure these galaxies have, what the ages are of their first generation of stars, how they formed, and how they contributed to the reionization process. It is therefore critical that *JWST* be designed and built to allow to do ultra-deep near-mid IR surveys. For the current purpose, this includes in particular that every reasonable effort be maintained to keep the scattered light in this open-tubed telescope to a minimum, so that we will be able to subtract the *l*ocal *JWST* sky-background — on $\lesssim$10 arcsec scales — to very high accuracy ($\lesssim 10^{-3}$ of the sky).

3. STARBURST INTENSITY LIMIT AT $z \simeq 5-6$

3.1. *Overview*

The peak star formation intensity in starburst galaxies does not vary significantly from the local universe to redshift $z \sim 6$. We arrive at this conclusion through new surface brightness measurements of 47 starburst galaxies at $z \simeq 5$–6, doubling the redshift range for such observations. These galaxies are spectroscopically confirmed in the Hubble Ultra Deep Field (HUDF) through the GRism ACS Program for Extragalactic Science (GRAPES) project. The starburst intensity limit for galaxies at $z \simeq 5-6$ agree with those at $z \simeq 3-4$ and $z \simeq 0$ to within a factor of a few, after correcting for cosmological surface brightness dimming and for dust. The most natural interpretation of this constancy over cosmic time is that the same physical mechanisms limit starburst intensity at all redshifts up to $z \simeq 6$ (be they galactic winds, gravitational instability, or something else). We do see two trends with redshift: First, the UV spectral slope (β) of galaxies at $z \simeq 5-6$ is bluer than that of $z \simeq 3$ galaxies, suggesting an increase in dust content over time. Second, the galaxy sizes from $z \simeq 3$ to $z \simeq 6$ scale approximately as the Hubble parameter $H^{-1}(z)$. Thus, galaxies at $z \simeq 6$ are high redshift starbursts, much like their local analogs except for slightly bluer colors, smaller physical sizes, and correspondingly lower overall luminosities. If we now assume a constant maximum star formation intensity, the differences in observed surface brightness between $z \simeq 0$ and $z \simeq 6$ are consistent with standard expanding cosmology and strongly inconsistent with a tired light model.

3.2. *Introduction*

Star formation on galactic scales is a key ingredient in understanding galaxy evolution. We cannot compare structure formation calculations to observed galaxy

populations without some model for how star formation proceeds. Such models are based on detailed observations in the nearby universe, combined with physically motivated scaling for differing conditions elsewhere in the universe. To test the validity of such scaling, it is valuable to directly measure the properties of star formation events in the distant universe, and see how they compare with their nearby counterparts.

Starbursts are regions of intense massive star formation that can dominate a galaxy's integrated spectrum. By comparing the properties of starbursts over a wide range of redshifts, we can test whether the most intense star formation events look the same throughout the observable history of the universe. High redshift galaxies are expected, on average, to be less massive and lower in metal abundance than their present-day counterparts. Either effect could in principle change the maximum intensity of star formation that such galaxies can sustain.

Meurer *et al.* (1997, hereafter M97) measured the effective surface brightness, i.e., the average surface brightness within an aperture that encompasses half of the total light, for various samples. They conclude that the maximum effective surface brightness of starburst galaxies is unchanged to better than an order of magnitude out to redshifts $z \simeq 3$. Weedman *et al.* (1998, hereafter W98) measured observed surface brightness from the single brightest pixel, and concluded that high-redshift ($2.2 \lesssim z \lesssim 3.5$) starburst galaxies have intrinsic ultra-violet (UV) surface brightnesses that are typically 4 times higher than for low-redshift starburst galaxies. Both M97 and W98 measured their surface brightness for spectroscopically confirmed galaxies in the Hubble Deep Field (HDF; Williams *et al.* 1996).

We have measured the surface brightness of starburst regions at $3 \lesssim z \lesssim 6$, using photometry from the HUDF images (Beckwith *et al.* 2006) and redshifts from the GRAPES project (Pirzkal *et al.* 2004). We combine these with earlier published results comparing $z \simeq 3$ and $z \simeq 0$ starbursts (M97, W98). The starburst intensity limit of starburst regions at $5 \lesssim z \lesssim 6$ sample is consistent with that at $z \simeq 3$ and $z \simeq 0$ to within the uncertainties, which are about a factor of three. *These high redshift star forming regions are thus starbursts, with a star formation intensity similar to their local counterparts, despite any effects of differing metallicity and/or galaxy size.* The starbursts should then be a set of standard surface brightness objects, and can be used to apply Tolman's test for expansion of the universe (Tolman 1930, 1934) over an unprecedented redshift range ($0 < z \lesssim 6$). Our surface brightness observations fully support standard expanding universe models. This result is robust to even rather large systematic errors, thanks to the wide redshift range spanned by the data.

Throughout this chapter we denote the *HST*/Advanced Camera for Surveys (ACS) F435W, F606W, F775W and F850LP filters as B, V, i', z', and *HST*/NIC3 F110W and F160W as J and H-bands, respectively. We assume a *Wilkinson Microwave Anisotropy Probe* (WMAP) cosmology of Ω_m=0.24, Ω_Λ=0.76 and H_0=73 km s^{-1} Mpc^{-1} (Spergel *et al.* 2007). This implies an age for the Universe of 13.7 Gyr. Magnitudes are given in the AB system (Oke & Gunn 1983).

3.3. *Observations and Sample Selection*

The HUDF is a 400 orbit survey of a $3.4' \times 3.4'$ field carried out with the ACS in the B, V, i' and z' filters (see Beckwith *et al.* 2006, for further details). We have

carried out deep unbiased slitless spectroscopy of this field with the ACS grism as part of the GRAPES project, which was awarded 40 *HST* orbits during Cycle 12 (ID 9793; PI S. Malhotra). The grism observations were taken at five different orientations in order to minimize the contamination of the spectra by overlapping nearby sources. We have extracted useful low resolution ($R \simeq 100$) spectra from 5900 Å to 9500 Å for ∼1500 objects in the HUDF to a limiting magnitude of $z'_{\rm AB} \simeq 27.5$ mag in the AB system. Details of the observations, data reduction and final GRAPES catalog are described in a paper by Pirzkal *et al.* (2004).

We identify high-redshift galaxies on the basis of their ACS grism spectra. This identification was based on detecting the Lyman break in the continuum or the Lyα emission for these sources. With the ACS grism low-resolution spectra, we are able to determine the redshifts to an accuracy of $\Delta z \approx 0.15$ even for the faintest detectable Lyman-break galaxies (LBGs) ($z'_{\rm AB} \simeq 27.5$ mag). Details of the selection process are described in Malhotra *et al.* (2005). There are 47 star-forming galaxies at $z \simeq 5-6$ in the GRAPES/HUDF with confirmed spectroscopic redshifts. These redshifts are sufficiently high that the observed visible/red wavelengths measure the rest-frame UV flux at wavelengths comparable to those at which M97 and W98 measured the surface brightness of starburst regions at $z \lesssim 3$. We used the following spectroscopically confirmed samples for our analysis.

- The $z \simeq 3$ LBGs from the Hubble Deep Field (HDF, Giavalisco *et al.* 1996; Steidel *et al.* 1996a,b) were used to compare our measurements with M97. This sample of 10 galaxies at $z \simeq 3$ forms the subset of UV samples used by M97. We

measured the UV spectral slopes (β) using observed (V–I) and (G–R) colors, and rest-frame UV fluxes were derived from the observed R-band (combined V and I light) magnitudes (Giavalisco *et al.* 1996; Steidel *et al.* 1996a,b). Here we denote the *HST*/WFPC2 F606W and F814W filters as V and I-bands, respectively. The G and R filters are defined in Steidel & Hamilton (1993).

- The $z \simeq 4$ B-band dropout galaxies were selected from the VLT redshift catalog of Vanzella *et al.* (2006). This sample is small (4 galaxies), but is useful for comparing $z \simeq 3-4$ and $z \simeq 5-6$ galaxy samples. We used the observed (i'–z') color to estimate β, and rest-frame UV fluxes were derived from the observed z'-band magnitudes. The observed i'- and z'-band magnitudes for $z \simeq 4$ galaxies were obtained from the HUDF/GOODS catalogs of Beckwith *et al.* (2006).

- We use a sample of 47 $z \simeq 5-6$ starburst galaxies having GRAPES redshifts (Malhotra *et al.* 2005; Rhoads *et al.* 2008) in the HUDF. Table 4 shows properties (coordinates, magnitudes, sizes and redshifts) for these 47 galaxies. We have only 19 galaxies (out of 47) covered by the Thompson *et al.* (2005) HUDF NICMOS images and therefore with J and H magnitudes. We estimate β from the observed (J–H) color. The rest-frame UV fluxes were derived from the observed J and H-band magnitudes for 19 galaxies, while the average β is used to predict J and H-band magnitudes for the remaining 28 galaxies for which we did not have NICMOS coverage.

TABLE 4: Sample of $z \simeq 4-6$ Galaxies

HUDF ID[a]	RA J2000	DEC J2000	B mag[b]	V mag	i' mag	z' mag	J mag	H mag	R50[c] pix	Redshift GRAPES
119	53.1660072	–27.8238735	28.98	29.22	27.46	27.83	—	—	3.42	5.09
322	53.1716057	–27.8207884	99.00[d]	31.94	29.15	27.05	—	—	5.33	5.70
457	53.1627077	–27.8189684	99.00	33.04	29.77	28.36	—	—	4.00	5.80
865[e]	53.1652728	–27.8140614	27.48	25.47	24.71	24.51	—	—	5.83	3.89[f]
1115	53.1722701	–27.8119757	99.00	27.93	26.38	26.19	26.71	26.21	4.67	4.70
1392	53.1563542	–27.8095882	99.00	31.18	27.78	28.44	—	—	2.43	5.10
2225	53.1667243	–27.8041607	99.00	29.68	26.73	25.16	25.47	25.29	5.24	5.80
2285	53.1683346	–27.8041253	99.00	29.75	27.92	27.83	—	—	3.18	5.20
2408	53.1885344	–27.8034642	31.30	28.69	26.87	26.68	—	—	5.87	4.90
2599	53.1626591	–27.8022980	99.00	28.83	27.20	27.12	27.56	27.80	3.81	5.00
2631	53.1774780	–27.8024502	99.00	99.00	29.82	27.88	—	—	4.21	6.60
2690	53.1407464	–27.8021066	99.00	33.28	29.24	27.35	—	—	3.26	5.90
2881	53.1415939	–27.8005701	99.00	27.65	25.93	25.70	25.66	25.50	5.62	4.60
2894	53.1462479	–27.8008152	99.00	29.90	27.79	27.80	—	—	3.64	5.30
2898	53.1798235	–27.8008762	36.61	28.51	27.00	27.15	27.66	27.75	3.74	4.80
3250	53.1326635	–27.7989462	99.00	30.39	27.45	27.59	—	—	4.62	4.90
3317	53.1439706	–27.7986558	31.40	29.89	28.32	27.11	27.28	27.26	7.86	6.10
3325	53.1439441	–27.7988859	99.00	31.96	28.77	27.13	27.26	27.02	3.92	6.00
3377	53.1359748	–27.7984127	32.41	35.99	28.59	27.70	26.97	26.02	4.05	5.60
3398	53.1358677	–27.7983281	31.61	31.30	28.23	26.82	27.03	27.27	4.83	5.60
3450	53.1428483	–27.7978540	32.37	33.01	28.86	27.51	27.02	27.44	6.39	5.90

Continued on next page...

TABLE 4 – Continued

HUDF ID[a]	RA J2000	DEC J2000	B mag[b]	V mag	i' mag	z' mag	J mag	H mag	R50[c] pix	Redshift GRAPES
3503	53.1429396	–27.7982143	99.00	31.16	29.37	27.92	—	—	5.52	6.40
3807	53.1457274	–27.7966782	99.00	31.90	29.28	28.33	—	—	4.10	6.10
3968	53.1833352	–27.7959542	32.56	30.25	27.83	28.72	—	—	4.20	4.70
4050	53.1392840	–27.7957997	31.35	31.44	29.58	27.49	27.33	27.46	3.74	6.00
4173	53.1721175	–27.7950895	99.00	29.56	27.34	27.16	—	—	3.55	5.00
5307	53.1908539	–27.7903658	99.00	29.79	27.41	26.96	26.67	26.73	3.67	5.00
5788	53.1456512	–27.7882204	31.06	29.89	27.61	27.02	—	—	6.07	5.10
6329	53.1466545	–27.7861315	99.00	31.16	28.10	27.02	27.15	27.46	3.97	5.50
6515	53.1273683	–27.7851701	99.00	28.55	27.34	27.59	—	—	3.13	4.75
7050	53.1510303	–27.7828664	31.22	29.48	27.45	26.89	27.29	27.25	4.04	5.40
7352	53.1376952	–27.7812664	31.88	28.88	26.92	26.86	26.45	26.16	6.27	4.60
8033	53.1519631	–27.7781802	99.00	31.24	28.70	26.29	26.35	25.75	7.22	6.00
8301	53.1671739	–27.7745269	35.49	29.64	27.28	27.00	27.37	27.03	4.73	4.90
8664	53.1890679	–27.7770073	99.00	28.77	26.92	26.80	—	—	4.96	5.00
8682	53.1887985	–27.7770926	30.61	28.08	26.13	25.83	—	—	8.01	5.00
8896	53.1900057	–27.7790583	31.79	28.44	26.94	26.90	—	—	4.73	5.00
8961	53.1420611	–27.7797801	99.00	30.65	28.83	26.68	—	—	4.01	5.80
9202	53.1383610	–27.7786918	99.00	32.11	29.13	27.61	—	—	5.41	5.70
9409[e]	53.1534403	–27.7661189	27.22	25.21	24.70	24.59	—	—	5.30	3.79[f]
9777	53.1702380	–27.7628560	99.00	28.19	26.20	25.35	—	—	5.04	5.40
9857	53.1627716	–27.7607679	30.87	38.76	28.58	27.12	—	—	3.69	5.80
9983	53.1671618	–27.7598597	30.31	27.51	25.66	25.51	—	—	7.34	4.80

Continued on next page...

TABLE 4 – Continued

HUDF ID[a]	RA J2000	DEC J2000	B mag[b]	V mag	i' mag	z' mag	J mag	H mag	R50[c] pix	Redshift GRAPES
20191	53.1725568	–27.8137124	31.23	27.15	25.77	25.67	25.81	25.51	5.79	4.67
30591	53.1553196	–27.8151593	33.39	31.37	32.27	27.51	—	—	4.99	6.70
32042	53.1689736	–27.8007244	99.00	32.72	31.75	28.84	—	—	4.00	5.75
33003	53.1460653	–27.7944931	99.00	99.00	31.63	28.00	27.47	27.35	4.01	6.40
35506	53.1660816	–27.7719653	30.31	32.92	31.06	27.82	—	—	5.97	6.20
36383	53.1677041	–27.7681044	99.00	99.00	31.07	28.66	—	—	5.58	5.80
–101[e]	53.1770656	–27.7643556	26.23	24.52	24.20	24.22	—	—	7.50	3.60[f]
–102[e]	53.1431467	–27.8155017	27.95	25.10	24.17	24.14	—	—	9.70	4.14[f]

[a] Identification from the HUDF catalogs of Beckwith *et al.* (2006), ACS grism spectra from Malhotra *et al.* (2005).

[b] All Magnitudes are given in the AB system.

[c] Half light radius (R50) measured in z'-band.

[d] A magnitude of 99.00 indicates no detection.

[e] Objects from Beckwith *et al.* (2006) B-band dropout catalog. Two objects with negative IDs don't have published HUDF IDs.

[f] Redshifts from Vanzella *et al.* (2006).

3.4. *Starburst Intensity Limit (M97 Approach)*

Magnitudes and color measurements. — All measurements for galaxies at $z \simeq 4-6$ were done on the *HST*/ACS HUDF images (Beckwith *et al.* 2006) and *HST*/NICMOS images (Thompson *et al.* 2005). The *HST*/NICMOS images were reprocessed by L. Eddie Bergeron (private communication). The *HST*/NICMOS images cover ∼50% of the HUDF ACS field. Therefore, only half of our galaxies have *J*- and *H*-band imaging. We need *J* and *H* magnitudes for galaxies at $z \simeq 5-6$ to measure the UV spectral slopes and luminosities at ∼2200 Å rest-frame. We use rest-frame ∼2200 Å to measure the effective surface brightness for consistency with M97. All broad-band magnitudes are measured as `SExtractor` (Bertin & Arnouts 1996) `MAG_AUTO` magnitudes, using dual-image mode to generate aperture-matched catalogs. We use the z'-band image as the detection image. `MAG_AUTO` apertures are Kron-like (Kron 1980) flexible apertures, which enclose most of the flux for an object. These apertures are same in all the filters for a given object. We also measured `SExtractor` Petrosian (1976) magnitudes (`MAG_PETRO`), with η=0.2 (Holwerda 2005), and isophotal magnitudes (`MAG_ISO`). We find that the average difference between `MAG_AUTO` and `MAG_PETRO` is ∼0.1 mag (i.e., $\langle m_{auto} - m_{petro} \rangle = \pm 0.1$), while the average difference between `MAG_AUTO` and `MAG_ISO` is ∼0.2 mag (i.e., $\langle m_{auto} - m_{iso} \rangle = \pm 0.2$). The effect of this magnitude uncertainty on the surface brightness measurements is very small (<0.1 dex). Our method to measure magnitudes is the same for all galaxies at $z \simeq 4-6$, and is consistent with the curve-of-growth method used for our comparison sample of $z \simeq 3$ galaxies (Giavalisco *et al.* 1996; Steidel *et al.* 1996a,b).

We use MAG_AUTO magnitudes to calculate the UV spectral slope (β) and the effective surface brightness.

The UV spectral slope (β). — The UV spectral slope (β) is determined from a power-law fit to the UV continuum spectrum (Calzetti *et al.* 1994),

$$f_\lambda \propto \lambda^\beta \quad ,$$

where f_λ is the flux density per unit wavelength (ergs s^{-1} cm^{-2} Å^{-1}). Converting this into magnitude units yields a linear relationship between β and colors. Figure 12 shows the average values of the UV spectral slopes, β, for galaxies at $z \simeq 3-4$ and $z \simeq$5–6. The mean values are plotted with error bars indicating the standard deviation of the mean (i.e., the sample standard deviation (σ) divided by the square root of the sample size (N)). The UV slopes for 10 galaxies at $z \simeq 3$ are obtained using the following two equations (M97) for two slightly different samples:

$$\beta = 2.55 \cdot (G - R) - 2 \ \text{ and } \ \beta = 3.23 \cdot (V - I) - 2 \quad .$$

Here G and R filters are defined in Steidel & Hamilton (1993). We also plot the average β measured for 4 galaxies at $z \simeq 4$, using:

$$\beta = 5.65 \cdot (i' - z') - 2$$

where we have used pivot wavelengths for i'- and z'-band, λ_i=7693 Å and $\lambda_{z'}$=9055 Å, respectively, to obtain the slope of 5.65 in the β–color linear relationship. Figure 12 also shows the average β for 19 galaxies at $z \simeq 5-6$ obtained using

$$\beta = 2.56 \cdot (J - H) - 2$$

where pivot wavelengths for the J- and H-bands are λ_J=11200 Å and λ_H=16040 Å, respectively, to obtain the slope of 2.56 in β–color relationship. We do not use (z'–J) color to estimate β for galaxies at $z \simeq 5$–6, because the (z'–J) colors can be insensitive to rest-frame UV colors due to the shorter color baseline, and are also more sensitive to uncertainties in the optical to infrared zero points (Bouwens *et al.* 2006). Therefore for comparison, we also measured β for galaxies at $z \simeq 5$ using (i'–z') colors and found that the average β is –1.53±0.38 compared to –1.65±0.21, the average β at $z \simeq 5$ using (J–H) colors. This implies that small variations in the UV rest-frame wavelength and observed colors do not affect the slope within the quoted uncertainties.

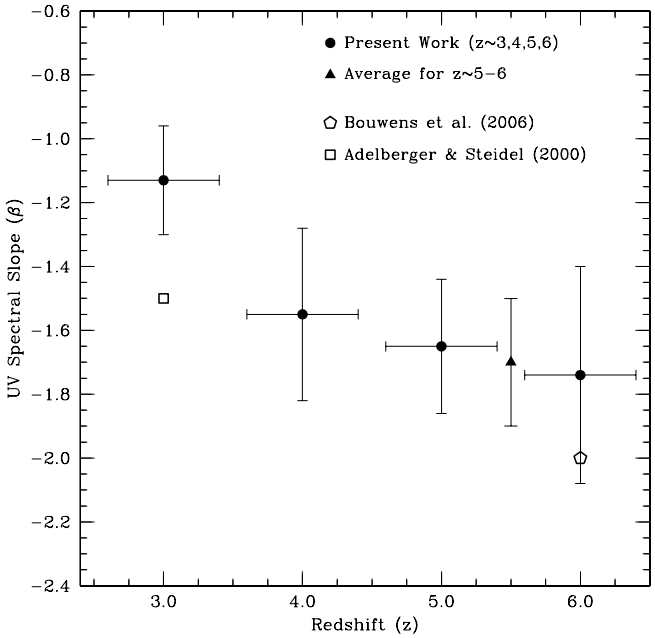

FIG. 12. UV spectral slopes (β) vs. redshift relation. Mean β are plotted with error bars indicating the standard deviation of the mean (i.e., $\sigma/\sqrt{N}$). We have plotted the data points at $z \simeq 3$ from Adelberger & Steidel (2000) and at $z \simeq 6$ from Bouwens *et al.* (2006) for comparison.

Figure 12 shows that the average β decreases from –1.13±0.17 at $z \simeq 3$ to –1.74±0.35 at $z \simeq 6$. The change in the average slope shows that the galaxies at $z \simeq 5-6$ are bluer than those at $z \simeq 3$, but still somewhat redder than the flat slope in f_ν ($f_\lambda \propto \lambda^{-2}$), that would be expected for a dust-free starburst galaxy.

Half-light radius (r_e or R50) measurements. — The half-light radius is defined as the radius containing 50% of the total flux of an object. The half-light radii for galaxies at $z \simeq 3$ are derived by Giavalisco *et al.* (1996) & Steidel *et al.* (1996b) and are measured such that half of the total emission from the starburst is enclosed within a circular aperture. We used the `SExtractor` half-light radii (R50, radii enclosing 50% of the flux within a circular aperture) obtained from the HUDF z'-band catalog (Beckwith *et al.* 2006) for galaxies at $z \simeq 4-6$. All radii are converted from arcsecs to kpc using a WMAP cosmology in the cosmological calculator by Wright (2006). The half-light radii for galaxies at $z \simeq 4-6$ are measured at rest-frame UV wavelengths λ=1500±300 Å. The sizes do not change appreciably when measured within this wavelength range. Figure 13 shows the average values of the half-light radii for 10 starburst galaxies at $z \simeq 3$, 4 starburst galaxies at $z \simeq 4$, and 47 starburst galaxies at $z \simeq 5-6$. Mean half-light radii are plotted with error bars indicating the standard deviation of the mean. The solid and dashed curves show the trend if sizes evolve as $H^{-1}(z)$ or $H^{-2/3}(z)$, respectively, where $H(z)$ is the Hubble parameter at redshift z. The curves are normalized to the mean size we measure at $z \simeq 4$ ($\sim$0.″21 or $\sim$1.5 kpc). Comparison between galaxies at $z \simeq 3$ and $z \simeq 5-6$ shows that the galaxy sizes increase as we go from $z \simeq 6$ to $z \simeq 3$.

We independently measured various flavors of `SExtractor` radii (half-light, Petrosian (1976), Kron) for galaxies at $z \simeq 5-6$ to assess the differences in these measurements. The Petrosian radius is defined as the radius at which the surface brightness is certain factor (η) of the average surface brightness within this isophote,

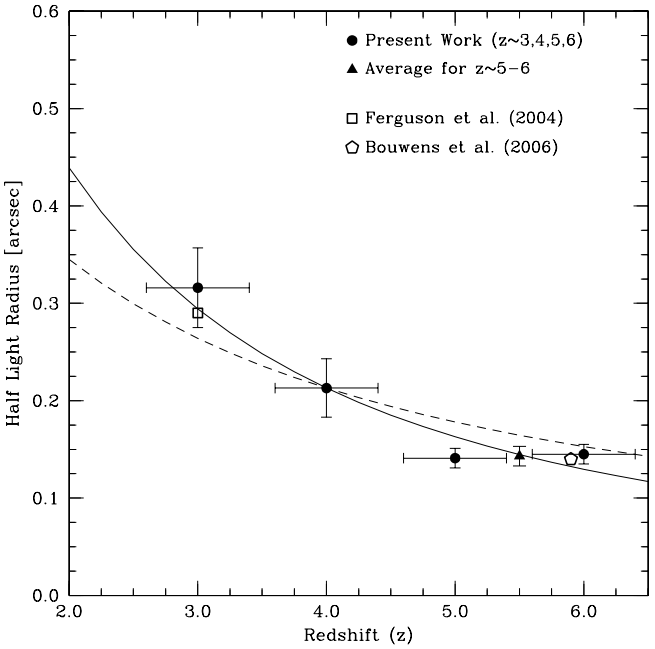

FIG. 13. Size (half-light radii) and redshift relation. Mean half-light radii are plotted with error bars indicating the standard deviation of the mean (i.e., $\sigma/\sqrt{N}$). The solid and dashed curves shows the trend if sizes evolve as $H^{-1}(z)$ and $H^{-2/3}(z)$, respectively. Both curves are normalized to the mean size at $z \simeq 4$ ($\sim$0.″21 or $\sim$1.5 kpc). We have plotted the data points at $z \simeq 3$ from Ferguson *et al.* (2004) and at $z \simeq 6$ from Bouwens *et al.* (2006) for comparison.

while the Kron radius is defined as the typical size of the flexible aperture computed from the moments (see `SExtractor` manual by Holwerda 2005, for further details). The average difference between the half-light and the other two radii was approximately $\pm$0.″04. Therefore, we expect about 30% uncertainty in the measurements of the half-light radii for galaxies at $z \simeq 5-6$.

Calculation of surface brightness for starburst galaxies. — We measure the effective surface brightness for 14 starburst galaxies at $z \simeq 3$–4 and 47 starburst galaxies at $z \simeq 5-6$ by adopting the method used by M97. First, we need to estimate dust extinction A_{1600} and k-corrections from the UV spectral slope (β). Dust extinction is estimated using the linear empirical relation between A_{1600} and β (Meurer *et al.* 1999), which is given by following equation:

$$A_{1600} = 4.43 + 1.99 \cdot (\beta)$$

where A_{1600} is the net absorption in magnitudes by dust at 1600 Å.

The next step in correcting apparent flux for corresponding rest-frame UV flux is to apply, where appropriate, the k-correction. We use following equation to estimate k-correction (M97):

$$k = \frac{f_{2320}}{f_{\lambda_c/1+z}} = \left[\frac{(1+z)\cdot 2320\ \text{Å}}{\lambda_c}\right]^{\beta}$$

where λ_c corresponds to the central wavelength of the filters used for the observed flux. Here, we reference all observations to the observations in M97, which use a UV central wavelength of 2320 Å. We apply above mentioned dust and k-corrections to apparent magnitudes to estimate absolute magnitudes and intrinsic UV luminosities for our samples of $z \simeq 3-6$ galaxies. The ratio of intrinsic UV to bolometric luminosity can be calculated for young starbursts. By using the stellar population models of Bruzual & Charlot (2003) to convert from intrinsic F220W flux/luminosity to bolometric luminosity, we find that the ratio of the UV to bolometric luminosity changes due to variations in the metallicity and the dust attenuation. The luminosity ratio spans a range from $\sim$0.2 to $\sim$0.5. The adopted ratio of the intrinsic UV to bolometric luminosity is:

$$\frac{L}{L_{\rm bol}} \simeq 0.33$$

We are using this value for the UV to bolometric luminosity ratio for two reasons:

(1) this bolometric correction is very close to the average value we get from our stellar population models, and

(2) this correction factor is also predicted by the models used by M97.

From $L_{\rm bol}$ and the half-light radii (r_e), we calculate effective surface brightness (S_e) using following relation:

$$S_e = \frac{L_{\rm bol}}{2\pi r_e^2} \quad \left(\frac{L_\odot}{\rm kpc^2}\right) \quad .$$

Here r_e is measured in kpc and $L_{\rm bol}$ in solar luminosities ($L_\odot$).

To characterize the S_e distribution for all galaxies in our sample we consider the median and 90^{th} percentiles, which we denote as $S_{e,50}$ and $S_{e,90}$, respectively. The upper limit to the surface brightness (starburst intensity limit) of starbursts is traced by $S_{e,90}$. Here we have used average β (from Figure 12) for each sample to estimate the surface brightness. Figure 14 shows $L_{\rm bol}$ and S_e as a function of r_e for the $z \simeq 0$–6 galaxy samples. The $z \simeq 0$ and $z \simeq 0.4$ surface brightness measurements are taken from M97. The $z \simeq 0$ data point is the median measurement for 11 nearby galaxies (M97). The $S_{e,50}$ and $S_{e,90}$ surface brightness levels of the combined sample are plotted as dashed and dotted lines respectively.

The top panel of the Figure 14 shows that the bolometric luminosities for galaxies at $z \simeq 5-6$ are smaller than the luminosities of galaxies at $z \simeq 3$. Using a two-sided K-S test on these luminosity distributions, we reject the hypothesis that the $z \simeq 3$ and $z \simeq 5-6$ luminosities are drawn from the same population at >99% probability. From the bottom panel of Figure 14, it is apparent that S_e shows little or no dependence on r_e over about one order of magnitude in size; hence there is no dependence on $L_{\rm bol}$ over about two orders of magnitude in luminosity. Figure 15 shows the effective surface brightness (S_e) as a function of redshift. The $z \simeq 0$ and $z \simeq 0.4$ surface brightness measurements are taken from M97. From Figure 14 and Figure 15,

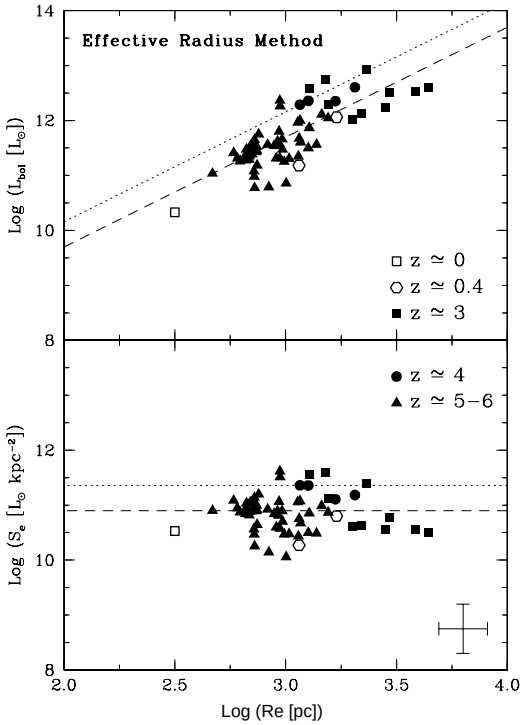

FIG. 14. Bolometric luminosity ($L_\odot^{\rm bol}$) and effective surface brightness ($L_\odot^{\rm bol}$ kpc^{-2}) against effective radii for starburst galaxies. The filled squares, circles and triangles are measurements for galaxies at $z\simeq3$, $z\simeq4$ and $z\simeq5-6$, respectively. The open square ($z\simeq0$) is the median measurement of 11 nearby galaxies from M97. The open hexagons ($z\simeq0.4$) are S_e measurements from M97. The dotted and dashed lines correspond to $S_{e,90}$ and $S_{e,50}$ of the combine sample. Uncertainties in $z\simeq3-6$ surface brightness and radii measurements are shown in lower right corner.

we find that $S_{e,90}$ of the starbursts remains constant (within the uncertainties) with redshift over the redshift range $z\simeq0-6$.

3.5. *Starburst Intensity Limit (W98 Approach)*

We also studied the surface brightnesses using the brightest pixel approach pioneered by Weedman *et al.* (1998). Weedman *et al.* (1998) measures observed surface brightness of the brightest pixel for galaxies at $2.2\lesssim z\lesssim3.5$ in the HDF and compared with the local starbursts by fading their observed (f_λ) surface brightness by $(1+z)^{-5}$. We use this approach to compare surface brightnesses of the brightest pixel for galaxies at $z\simeq3-6$.

A postage stamp (51×51 pixels) for each galaxy at $z\simeq5-6$ was excised from the z'-band HUDF image. Using z'-band segmentation maps, only object pixels were selected. For each object pixel in the postage stamp, we estimate the apparent

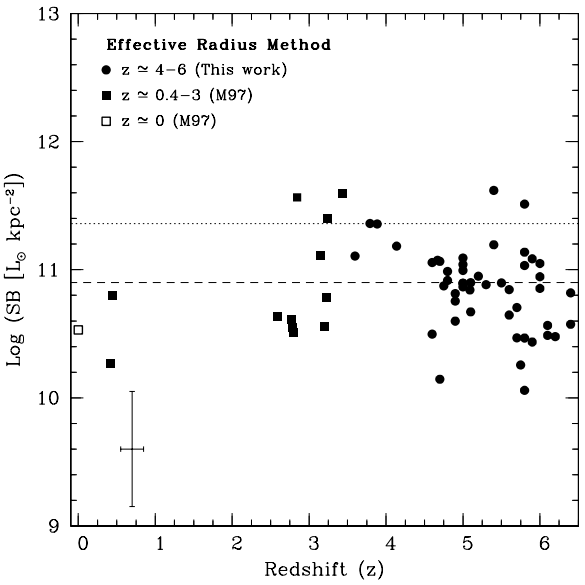

FIG. 15. Bolometric effective surface brightness ($L_{\odot}^{\rm bol}$ kpc^{-2}) as a function of redshift. The open square ($z \simeq 0$) is the median measurement of 11 nearby galaxies from M97. The filled squares ($z \simeq 0.4$) are S_e measurements from M97. The filled squares ($z \simeq 3$) are the galaxies from the sample of M97 for which we measured surface brightnesses. The circles are the galaxies in our sample ($z \simeq 4-6$). The dotted and dashed lines correspond to $S_{e,90}$ and $S_{e,50}$ of the combined sample. Uncertainties in $z \simeq 3-6$ surface brightness (due to radii and flux uncertainties) is shown in lower left corner.

magnitude. For the brightest pixel in each galaxy, the average UV spectral slope β was used to predict J-band (for galaxies at $z \simeq 5$) and H-band (for galaxies at $z \simeq 6$) magnitudes from z'-band apparent magnitudes. Using similar approach as discussed in previous chapter, we calculated the intrinsic UV luminosity ($L_{\odot}^{\rm UV}$) for the brightest pixel in each galaxy at $z \simeq 5-6$. For surface brightness measurements, we divide the intrinsic UV luminosity by the area of one pixel in kpc^2.

Figure 16 shows surface brightness ($L_{\odot}^{\rm UV}$ kpc^{-2}) for the brightest pixel in each of the 47 galaxies at $z \simeq 5$–6 and 4 galaxies at $z \simeq 4$. We have also plotted 18 galaxies at $z \simeq 3$ from W98. The W98 galaxies has observed surface brightnesses for the brightest pixels and hence, for proper comparison, we converted observed surface brightnesses for W98 galaxies to their corresponding rest-frame surface brightnesses. Here we have used average β for $z \simeq 3$ galaxies as shown in Figure 12, to estimate extinction and k-correction. The median ($S_{bp,50}$) and 90^{th} percentile ($S_{bp,90}$) surface brightness levels

of the combined sample are plotted as dashed and dotted lines, respectively. Here, the starburst intensity limit of starbursts is traced by $S_{bp,90}$. The $S_{bp,90}$ of galaxies at $z \simeq 3$ and $z \simeq 5-6$ is same to within a factor of $\sim$0.10 dex.

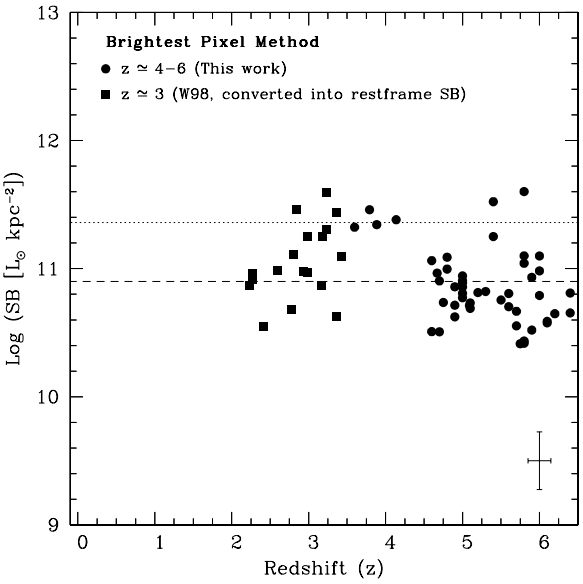

FIG. 16. Surface Brightness obtained from the brightest pixel of 47 galaxy images at $z \simeq 5-6$ and 4 galaxy images at $z \simeq 4$. The squares are 18 W98 galaxies. The W98 galaxies had observed surface brightnesses and hence, for proper comparison, we converted observed surface brightnesses to corresponding rest-frame surface brightnesses. The dotted and dashed lines correspond to $S_{bp,90}$ and $S_{bp,50}$ of the combine sample. Uncertainties in surface brightness (due to flux uncertainties) is shown in lower right corner.

We cannot properly compare the brightest pixel surface brightnesses between the W98 sample at $z \simeq 0$ and galaxies at $z \simeq 3-6$ for two reasons. First, the aperture sizes for W98 galaxies at $z \simeq 0$ are larger than the physical sizes corresponding to one pixel at $z \simeq 3-6$, and the sizes for W98 galaxies at $z \simeq 0$ are also larger than the effective radii measured by Meurer *et al.* (1995) for some of these local galaxies. Second, the discrepancy between the W98 adopted UV spectral slope (β) and β from Meurer *et al.* (1995) is large for some of these galaxies, which affects the applied extinction for their luminosity measurements.

Our analysis of the effective surface brightness (S_e) approach of M97 and the brightest pixel (S_{bp}) approach of W98 suggests that the starburst intensity limit, as

defined by $S_{e,90}$ or $S_{bp,90}$, of the starbursts is unchanged (within uncertainties) from $z \simeq 5-6$ to $z \simeq 3$.

3.6. *Results and Discussion*

Selection and measurement effects. — In following section, we discuss estimated uncertainties in the starburst intensity limit due to selection and measurement effects:

Different radii-measurements: The results shown in Figures 13, 14 and 15 use `SExtractor` half-light radii derived by Beckwith *et al.* (2006). Here we discuss the uncertainty in the surface brightness measurements due to radii measurements. We use three different flavors of radii measured using `SExtractor`. We measured the half-light radii, the Petrosian (1976) radii and the Kron radii for galaxies at $z \simeq 5-6$. We found that the average difference between the half-light radius and other two radii was approximately $\pm 0\farcs04$. This difference does not affect our conclusion that $z \simeq 5-6$ galaxies are smaller compared to $z \simeq 3$ galaxies. As shown in Figure 13, the average value of the half-light radii for galaxies at $z \simeq 5-6$ is $0\farcs14$ compared to $0\farcs32$, which is the average value for galaxies at $z \simeq 3$. The uncertainty in three different radii measurements is $\pm 0\farcs04$. Therefore for a given luminosity, we expect that this difference in radii measurement will cause $\sim$0.2 dex difference in $S_{e,90}$ estimate.

Surface brightness selection: The limiting surface brightness in the HUDF samples is $S_e \sim 5.0 \times 10^9\ L_\odot\ \mathrm{kpc}^{-2}$ at $z \simeq 5-6$, which is much fainter than the observed maximum surface brightness ($S_{e,90} \simeq 2.3 \times 10^{11}\ L_\odot\ \mathrm{kpc}^{-2}$) for all galaxies.

At the low surface brightness limit, our sample could be incomplete, but at the maximum surface brightness level our sample is complete.

Size selection effect: The $z \simeq 3$ galaxies are spectroscopically confirmed by Keck observations. The limiting magnitude for Keck spectroscopy is $R \lesssim 25.3$ (Steidel *et al.* 1996b). Using $S_{e,90}$ and the limiting magnitude, we estimate the minimum observable size for this sample as $\sim$700 pc or $\sim 0''.1$. Therefore, this sample of galaxies at $z \simeq 3$ is not biased against smaller sizes.

Flux uncertainty: Here we discuss three possible sources of uncertainties in the magnitudes (for a given size) that will affect our surface brightness measurements. They are as follows: (1) The average `SExtractor` uncertainties in J and H magnitudes are $\sim$0.2 mag. The largest magnitude uncertainties in the sample range up to $\sim$0.5 mag for three objects. Even this worst case magnitude uncertainty affects $S_{e,90}$ by only $\sim$0.2 dex. The uncertainty in $S_{e,90}$ due to the average difference between various magnitudes (`MAG_AUTO`, `MAG_PETRO` and `MAG_ISO`) is very small ($<$0.1 dex) and hence the uncertainties in J, H magnitudes dominate the uncertainty in $S_{e,90}$. (2) The ratio of the UV to bolometric luminosity for starburst galaxies is based on the stellar population models. We find that this ratio is affected by the change in metallicity or dust extinction in the stellar population models. The uncertainty in this ratio can be as large as a factor of $\sim$2.0. This uncertainty in the bolometric correction will change $S_{e,90}$ estimate by $\sim$0.3 dex but this is systematic uncertainty and will affect all starburst galaxies. (3) We have used linear fit to the observed relation between the F_{FIR}/F_{1600} and the UV spectral slope (β) to estimate A_{1600} (Fig.1 in Meurer *et*

al. 1999). The scatter in this plot can cause an uncertainty in A_{1600} of $\sim$0.4 mag. This uncertainty in A_{1600} will change $S_{e,90}$ estimate by $\sim$0.2 dex. This uncertainty will systematically affect all galaxies in this study.

Therefore, if these logarithmic uncertainties add in quadrature, we would expect the total uncertainty in $S_{e,90}$ to be $\sim$0.5 dex.

The starburst intensity limit. — We measure the effective surface brightness (S_e) and the brightest pixel surface brightness (S_{bp}) of the *spectroscopically* confirmed galaxies at $z \simeq 5-6$ in the HUDF and compare with the spectroscopically confirmed galaxies at $z \simeq 3$ in the HDF. We conclude that to better than a factor of 3, the starburst intensity limit of starbursts at $z \simeq 3$ and $z \simeq 5$–6 are the same. Using the K-S test on these distributions, the resulting probabilities ($\gtrsim$20%) support the hypothesis that these distributions are drawn from the same population. By combining the samples at $z \simeq 3-4$ and $z \simeq 5-6$, we find a mean $S_{e,90} \simeq 2.3 \times 10^{11}\ L_{\odot}\ \mathrm{kpc}^{-2}$ (with a factor of 3 or $\sim$0.5 dex uncertainty). We quantify the scatter in the S_e and S_{bp} distributions (Figures 15 and 16) by measuring standard deviation (σ) from a Gaussian fit to these distributions. We find that the scatter in the S_e distribution ($\sigma_{log(S_e)} \simeq 0.37$) is higher than the scatter in the S_{bp} distribution ($\sigma_{log(S_{bp})} \simeq 0.27$). Therefore, the brightest pixel method could be very useful in estimating the starburst intensity limit of starburst galaxies.

The approximate constancy of peak starburst intensity can be interpreted as the evidence that the interstellar medium (ISM) can only support some maximum pressure. Heckman *et al.* (1990) used [S II] emission line ratios to determine the

ISM pressure (P_0) for a sample of galaxies (mostly starbursts) undergoing a strong galactic wind. The star formation intensity required to produce P_0 is $S_e \simeq 1.7 \times 10^{11}$ $L_\odot$ kpc^{-2} (M97). This value agrees closely with our $S_{e,90}$, but was derived using different method. The physical process can be explained by assuming that the ISM pressure provides a "thermostat" for star-formation, such that strong outflows will result whenever the pressure rises above P_0 and shut down further star formation for a time. This results in a characteristic peak starburst intensity. We convert $S_{e,90}$ to an equivalent star formation intensity ($M_\odot$ yr^{-1} kpc^{-2}) by using conversion factors between UV luminosity and star-formation rate from Kennicutt (1998) and M97. We get a star-formation intensity in the range of 30–50 $M_\odot$ yr^{-1} kpc^{-2}, depending on the conversion factor. This peak intensity is physically distinct from the minimum intensity required to produce a galactic wind, which is orders of magnitude lower, at ~ 0.1 $M_\odot$ yr^{-1} kpc^{-2} (Lehnert & Heckman 1996; Heckman 2001). Thus, *every* galaxy in our sample is expected to have a galactic wind, as Lehnert *et al.* (2007) remark for a similar sample of $z \gtrsim 3$ LBGs. However, only in galaxies near the starburst intensity limit does the "thermostat" become active.

While the peak starburst intensity stays constant with redshift, the dust optical depth that we infer from the observed spectral slope β decreases systematically with redshift. This suggests that the star formation intensity limit does not depend on dust content, at least over the range of dust optical depths $\tau_{dust} \gtrsim 1$ probed by our sample. At yet higher redshifts we might expect that $\tau_{dust} < 1$, and that the starburst radiation field would no longer couple efficiently to the interstellar medium.

Whether this would substantially change the starburst intensity limit would depend on the fraction of starburst wind driving that is due to radiation pressure, rather than stellar winds and mechanical energy from supernova explosions.

The constancy of maximum star-formation surface intensity with redshift provides a basis for a strong test of the expanding Universe. Standard cosmologies predict that the bolometric surface brightness should vary with redshift as $(1+z)^{-4}$. Our results (using standard cosmology) combined with M97 results at low redshifts show that the maximum star formation intensity remains constant (within uncertainties) from $z \simeq 0$ to $z \simeq 6$. This conclusion depends critically on the use of a standard cosmology to go from observed flux and radius to inferred star formation intensity. Thus, if the peak star formation rate per unit area is controlled by some physical limit that is based on local, redshift-independent physics, our observations essentially require standard surface brightness dimming. While other evolutionary effects could become important, we have minimized these by measuring surface brightnesses at nearly fixed rest wavelength. Had we instead taken a "tired light" model, where bolometric surface brightness falls of as $(1+z)^{-1}$, our observations would require the true star formation intensity to be dramatically lower at high redshift— by a factor of order $(1+z)^3 \sim 7^3 \sim 300$. This factor greatly exceeds the estimated uncertainties in our analysis. Hence, the wide redshift range of our sample yields a strong application of Tolman's test (Tolman 1930, 1934), and we derive strong evidence in favor of the expanding Universe and against any alternative "tired light" models.

Size and luminosity evolution. — An average galaxy at $z \simeq 5-6$ in our sample has half-light radii of $\sim$0.8 kpc or $\sim 0\farcs14$, as shown in Figure 13, which is in good agreement with a number of recent studies (Bouwens *et al.* 2004b, 2006; Pirzkal *et al.* 2007; Dow-Hygelund *et al.* 2007). Ferguson *et al.* (2004) compares sizes of galaxies at $z \simeq 1$–5 within a fixed luminosity range. Our results agree with Ferguson *et al.* (2004) for $z \simeq 3-4$. The UV intrinsic luminosities for our sample of galaxies are brighter or equal to L^* (i.e., $L \gtrsim L^*$) at respective redshifts, but we do not require any particular minimum luminosity, while Ferguson *et al.* (2004) do require a minimum luminosity. Given that the maximum surface brightness is near-constant, a minimum luminosity immediately implies some minimum radius for inclusion in the Ferguson *et al.* (2004) sample. Figure 13 also shows comparison of our size measurements with the Ferguson *et al.* (2004) and the Bouwens *et al.* (2006) results. The solid and dashed curves in the Figure 13 show the trend if sizes evolve as $H^{-1}(z)$ or $H^{-2/3}(z)$, respectively, where $H(z)$ is the Hubble parameter at redshift z. The curves are normalized to the mean size we measure at $z \simeq 4$ ($\sim 0\farcs21$ or $\sim$1.5 kpc). The galaxy sizes from $z \simeq 3$ to $z \simeq 6$ scale approximately as the Hubble parameter $H^{-1}(z)$, though it is difficult to conclude with certainty how sizes scale from the measurements of high redshift ($z \gtrsim 3$) galaxies only, because two trends diverge significantly at lower redshifts ($z < 3$).

We also find that the bolometric or intrinsic UV luminosity for galaxies at $z \simeq 5-6$ is lower than for galaxies at $z \simeq 3-4$. The galaxies at $z \simeq 5-6$ are smaller compared to $z \simeq 3$ galaxies, while the maximum surface brightness remains

approximately constant. Therefore, the luminosity evolution could be due to the constant upper limit on the surface brightness as a function of redshift.

Evolution in UV spectral slope (β). — Our $z \simeq 3-6$ sample also allows us to place constraints on the rest-frame UV slope. We obtained these constraints by measuring rest-frame UV colors of $z \simeq 3-4$ and $z \simeq 5-6$, galaxies as shown in Figure 12. A comparison of our measured colors with those obtained in two previous studies (Stanway *et al.* 2005; Bouwens *et al.* 2006) show agreement within our 1σ uncertainties. The mean β inferred from this study for $z \simeq 6$ galaxies is β=–1.74±0.35, which is redder than the β=–2.0±0.3 inferred in the Bouwens *et al.* (2006) or the β=–2.2±0.2 inferred in the Stanway *et al.* (2005). We also find that the mean β value for galaxies at $z \simeq 5-6$ is bluer than the β=–1.1±0.2 we measure at $z \simeq 3$, or the β=–1.5±0.4 observed by the Adelberger & Steidel (2000). Irrespective of the exact β, the mean rest-frame UV slope observed at $z \simeq 5-6$ is bluer than that observed at $z \simeq 3$. This evolution is consistent with number of recent studies (Stanway *et al.* 2005; Yan *et al.* 2005; Bouwens *et al.* 2006).

To understand the evolution in the β, we use the `STARBURST99` stellar synthesis code *version 5.1* (Leitherer *et al.* 1999; Vázquez & Leitherer 2005) to investigate the variations in β as function of IMF, metallicity and the star formation history. We assume two different metallicities ($Z = 0.004$ and 0.02), two different star formation histories (constant and instantaneous) and two different versions of the Salpeter (1955) IMFs (α=2.35 with M_{up}=100 $M_\odot$ and α=2.35 with M_{up}=30 $M_\odot$). We measure β for various models by fitting a first-order polynomial to the UV spectra through

the wavelength interval 1250–1850 Å. We find that the changes in metallicity and the IMF have much smaller effect on the rest-frame UV slope for young ($\lesssim$20 Myr) starbursts. Our results agree with the Leitherer *et al.* (1999) models showing that the UV spectral slopes are independent of evolution and IMF effects. Leitherer *et al.* (1999) shows that for young starbursts, the UV spectral slope (β) at 2500 Å also does not change very much as a function of model parameters (Z and IMF). Therefore the observed evolution in β from $z \simeq 5$–6 to $z \simeq 3$ is more likely due to changes in the dust content, which reflect the slow build-up of metals in the galaxy's ISM as the cosmic SFR ramps up from $z \gtrsim 6$ to $z \simeq 3$.

4. LATE-TYPE GALAXIES AT $z \simeq 1$

4.1. *Overview*

We take advantage of the exceptional depth of the Hubble Ultra Deep Field (HUDF) images and the GRism ACS Program for Extragalactic Science (GRAPES) grism spectroscopy to explore the stellar populations of 34 bulges belonging to late-type galaxies at $0.8 \leq z \leq 1.3$. We selected these galaxies based on the presence of a noticeable Balmer break (at 4000 Å) in their GRAPES spectra, and by visual inspection of the HUDF images. The narrow extraction of these GRAPES spectra around the galaxy center enables us to study the spectrum of the bulges in these late-type galaxies. The 4000 Å break in the bulges spectra allows us to estimate the bulges redshifts and stellar ages. We first used the HUDF images to measure bulges color and Sérsic index. Next, we analyze the bulges spectra by fitting stellar population models. Our results show that, (1) the average age of late-type bulges in our sample is $\sim$1.3 Gyr and stellar masses are in the range of $10^{6.5}$-10^{10} $M_{\odot}$, (2) late-type bulges are younger and less massive compared to bulges in early-type galaxies at similar redshifts, (3) bulges and inner disks in these late-type galaxies show similar dominant stellar populations, suggestive of an inside-out formation scenario, and (4) late-type bulges are better fitted by exponential surface brightness profiles. The overall picture emerging from the GRAPES data is that, in late-type galaxies at $z \simeq 1$, bulges form through secular evolution and disks via an inside-out process.

4.2. *Introduction*

There are currently two alternative scenarios to explain bulge formation in galaxies. First, semi-analytic models have traditionally proposed early formation from mergers, generating a scaled-down version of an elliptical galaxy (e.g., Kauffmann

et al. 1993). Second, dynamical instabilities can contribute to the formation of a bulge in a primordial disk (Kormendy & Kennicutt 2004). These instabilities can be triggered either internally, or by the accretion of small satellite galaxies (Hernquist & Mihos 1995), and may result in later stages of star formation. Hence, the stellar populations in galaxy bulges provide valuable constraints to distinguish between these two scenarios.

The ability of the *Hubble Space Telescope* (*HST*) to resolve distant galaxies enabled the study of bulges in galaxies out to redshift $z \simeq 1$ (Bouwens *et al.* 1999; Abraham *et al.* 1999; Ellis *et al.* 2001; Menanteau *et al.* 2001; Koo *et al.* 2005; MacArthur *et al.* 2008). Simple phenomenological models – such as the one presented in Bouwens *et al.* (1999) – have, in the past, tried to determine whether bulge formation happens before or after the formation of the disk. The advantage of the lookback time probed out to $z \simeq 1$ allows us to quantify the occurrence of merging vs. secular formation of bulges. In the sample presented here we take advantage of the superb capabilities of the Advanced Camera for Surveys (ACS) to extract (slitless) low resolution spectra of bulges from faint galaxies at these redshifts.

In their detailed review, Kormendy & Kennicutt (2004) discuss two distinct type of bulges, classical bulges — i.e., merger-built with Sérsic index $n \gtrsim 2$ — and pseudo bulges — built out of disk material having Sérsic index $n < 2$. Early-type galaxies tend to have classical bulges, while late-type galaxies are more likely to host a pseudo bulge. This scenario states that early- and late-type galaxies generally form their bulges in different ways. Many studies have been done at low and high redshifts

to investigate properties of bulges and their formation histories. Studies on local galaxies (de Jong 1996; Courteau *et al.* 1996; Thomas & Davies 2006; Carollo *et al.* 2007) have shown through colors and surface brightness profiles that towards later-type galaxies along the Hubble sequence, more bulges are best-fit by an exponential profile (disk-like) compared to an $r^{1/4}$ profile. Courteau *et al.* (1996) and de Jong (1996) carried out bulge-disk decompositions for $\gtrsim$80 galaxies, and found that 60–80% of late-type galaxies are best-fit by the double exponential profiles. More recently, Carollo *et al.* (2007) used *HST* ACS and the Near Infrared Camera and Multi Object Spectrometer (NICMOS) multi-band imaging to study the structure and the inner optical and near-infrared colors of local ($z \simeq 0$) bulges in a sample of nine late-type spirals. Their analysis suggests that half of the late-type bulges in their sample must have developed *a*fter the formation of the disk, while for other half, the bulk of stellar mass was produced at earlier epochs — as is found in early-type spheroids — and hence must have developed before the formation of the disk. Thomas & Davies (2006) analysed the central stellar populations of bulges in spiral galaxies with Hubble types Sa to Sbc by deriving luminosity-weighted ages and metallicities. They find that bulges are generally younger than early-type galaxies, because of their smaller masses. They suggest that bulges, like low-mass ellipticals, are rejuvenated, but not by secular evolution processes involving disk material.

On the theoretical side, semi-analytical and N-body simulations of galaxy formation have been mainly based on two basic assumptions. In the first scenario, all bulges result from the merging of disk galaxies (e.g., Kauffmann *et al.* 1993), whereas

the second one is based on an inside-out bulge formation scenario (e.g., van den Bosch 1998), in which baryonic matter of a protogalaxy virializes and settles in an inside-out process. Athanassoula (2008) argues that in order to adequately describe the formation and evolution of disk-like bulges, simulations should include gas, star formation and feedback. The author also states the importance of cosmologically-motivated initial conditions in the simulations, since the properties of pre-existing disks may influence the properties of the disk-like bulges. When accounting for these effects, Athanassoula (2008) simulated bulges that show properties similar to the observed disk-like bulges.

The initial studies of bulges at high redshift (Abraham *et al.* 1999; Ellis *et al.* 2001; Menanteau *et al.* 2001) were done by measuring optical colors in galaxies to distinguish between bulge and disk colors. Ellis *et al.* (2001) analyzed the internal optical colors of early-type and spiral galaxies from the Hubble Deep Fields (HDF, Williams *et al.* 1996) for redshifts $z \lesssim 0.6$. They find that bulges are redder than the surrounding disks, but bluer than pure ellipticals at the same redshifts. In other work, Menanteau *et al.* (2001) find strong variations in internal/central colors of more than 30% of the faint spheroidals in the HDF. They do not find such large variations in cluster galaxies, and hence estimate that at $z \simeq 1$, these strong color variations in field bulges are due to more recent episodes of star-formation. Recent studies (Koo *et al.* 2005; MacArthur *et al.* 2008) have focused on bulge-disk decompositions to investigate the colors and radial profiles of bulges at $z \simeq 1$. Koo *et al.* (2005) present a candidate sample of luminous high-redshift ($0.73 < z < 1.04$) bulges ($I_{814} < 23.1$

mag) within the Groth Strip Survey, and find that majority of luminous bulges at $z \simeq 1$ are very red. Their data favors an early bulge-formation scenario in which bulges and field E-S0's form prior to disks. MacArthur *et al.* (2008) study bulges of spiral galaxies within the redshift range $0.1 < z < 1.2$ in the Great Observatories Origins Deep Survey (GOODS) fields, and find that bulges of similar mass follow similar evolutionary patterns.

In this chapter, we use the extraordinary imaging depth of the Hubble Ultra Deep Field (HUDF, Beckwith *et al.* 2006) and deep slitless grism spectroscopy using ACS from the GRism ACS Program for Extragalactic Science (GRAPES) project (PI: S. Malhotra; Pirzkal *et al.* 2004; Malhotra *et al.* 2005) to explore the stellar ages of bulges in late-type galaxies at $z \simeq 1$. The exceptional angular resolution and depth of the GRAPES/HUDF data combined with excellent grism sensitivity allows us to extract spectra of the most central regions of faint galaxies at $z \simeq 1$.

Throughout this chapter we refer to the *HST*/ACS F435W, F606W, F775W, and F850LP filters as the B-, V-, i'-, and z'-bands, respectively. We adopt a Hubble constant H_0=70 km s^{-1} Mpc^{-1} and a flat cosmology with Ω_m=0.3 and Ω_Λ=0.7. At redshift $z \simeq 1$, this cosmology yields a scale of $1''.0 = 8.0$ kpc. The lookback time is 7.7 Gyr for a universe that is 13.5 Gyr old. Magnitudes are given in the AB system (Oke & Gunn 1983).

4.3. *Observations and Sample Selection*

The HST/ACS data. — The HUDF is a 400 orbit survey of a $3.4' \times 3.4'$ field carried out with the ACS in the B, V, i' and z' filters (Beckwith *et al.* 2006). We have

carried out deep slitless spectroscopy of this field with the ACS grism as a part of the GRAPES project, which was awarded 40 *HST* orbits during Cycle 12 (ID 9793; PI: S. Malhotra). The grism observations were taken at five different orientations, in order to minimize the effects of contamination and overlapping from nearby objects. We have extracted low resolution spectra ($R \simeq 50-100$[4]) from 6000 to 9500 Å for objects in the HUDF to a limiting magnitude of $z'_{\rm AB} \simeq 27.5$ mag at a net significance $N > 5$. Details of the observations, data reduction and final GRAPES catalog are described in Pirzkal *et al.* (2004). We used the multi-band high-resolution HUDF images to study each object at $z \simeq 1$ in the ACS band closest to the B-band rest-frame, in order to minimize any effects of the morphological K-correction (e.g., Windhorst *et al.* 2002). Colors for our galaxies are in the *HST* ACS V, i' and z' system, bracketing the 4000 Å break and corresponding to rest-frame (U–B) at redshifts $z \simeq 1$.

Sample selection and properties. — The *HST*/ACS grism sensitivity peaks at ∼8000 Å, and hence the GRAPES spectra are sensitive in identifying galaxies at $z \simeq 1$ through their 4000 Å breaks, and galaxies at $z \simeq 5-6$ through their Lyman breaks. We selected objects with high signal-to-noise in the one-dimensional (1D) GRAPES grism spectra (∼1500 in the HUDF) that show continuum breaks. All these spectra were extracted using narrow extraction windows (5 pixels wide — the pixel-scale in the grism images is 0.″05/pixel) around the center of each galaxy. We compared the running average of flux in 10 data points between neighboring regions on each 1D spectrum. If the difference between two neighboring, average flux values was greater

[4]Slitless spectroscopy results in a variable spectral resolution, depending on the size of the object. These details concerning the slitless spectroscopy are described in Pasquali *et al.* (2006a)

than 3σ, we considered that change in flux level as a 'break' in the spectrum. A large ($\sim$150) number of objects were selected using this technique. After this visual selection procedure, many objects were classified and studied as Lyman break galaxies at $z \gtrsim 4.5$ (Malhotra *et al.* 2005; Hathi *et al.* 2008a), or as late-type stars (Pirzkal *et al.* 2005), or as ellipticals at $z \simeq 1$ (Pasquali *et al.* 2006b). During this visual classification, we also found that a number of late-type galaxies (mostly spirals) showed a prominent 4000 Å break (at observed $\sim$8000 Å), which is the major spectral feature due to the presence of an old stellar population. This feature was in general observed in all grism spectra obtained for each object at different position angles, unless object grism overlap prevented us from doing so at one particular grism position angle. We selected 34 late-type galaxies (median redshift $z \simeq 1$), to study the properties of their central stellar populations. We measure D4000 — the amplitude of the 4000 Å break (Balogh *et al.* 1999) — as the ratio of the average continuum flux longward and shortward of the 4000 Å break from the 1D grism spectra. Figure 17 shows the distribution of D4000 for these galaxies at $z \simeq 1$. The average D4000 ($\sim$1.3) for the selected late-type galaxies (grey histogram) is smaller than the D4000 observed for a typical elliptical galaxy (> 1.6, Kauffmann *et al.* 2003; Padmanabhan *et al.* 2004). We also show D4000 (hashed histogram) for elliptical galaxies ($0.6 \leq z \leq 1.1$) from Pasquali *et al.* (2006b). Figure 18 shows the color-composite images of 6 typical late-type galaxies at $z \simeq 1$ in our sample, which clearly demonstrates that all have redder bulges in their centers. Table 5 shows the optical ($BVi'z'$) magnitudes, the HUDF IDs, and coordinates for each selected galaxy, as obtained from the published HUDF catalog (Beckwith

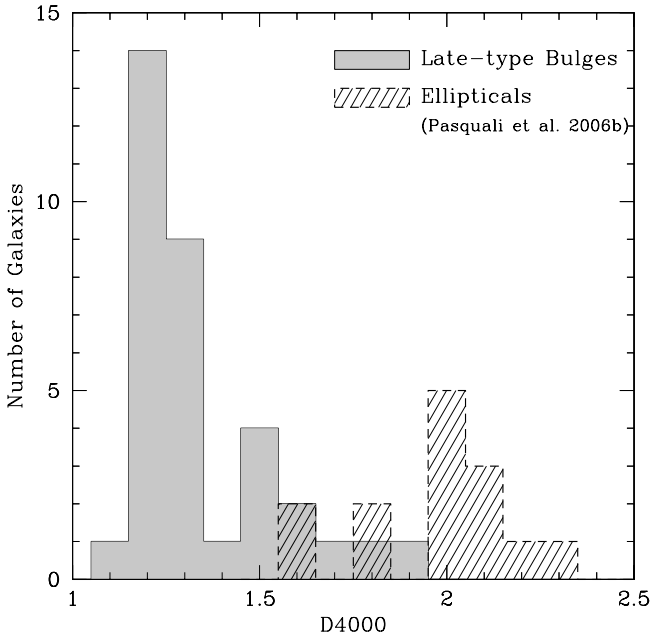

FIG. 17. Distribution of amplitude of 4000 Å break (D4000; Balogh *et al.* 1999) for all galaxies in our sample (grey histogram). D4000 was measured as a ratio of average continuum flux redward and blueward of the 4000 Å break from 1D GRAPES grism spectra. The average value of the D4000 is ∼1.3 and for comparison, the ellipticals have D4000 > 1.6 (Kauffmann *et al.* 2003; Padmanabhan *et al.* 2004). We have also plotted D4000 (hashed histogram) for elliptical galaxies ($0.6 \leq z \leq 1.1$) from Pasquali *et al.* (2006b).

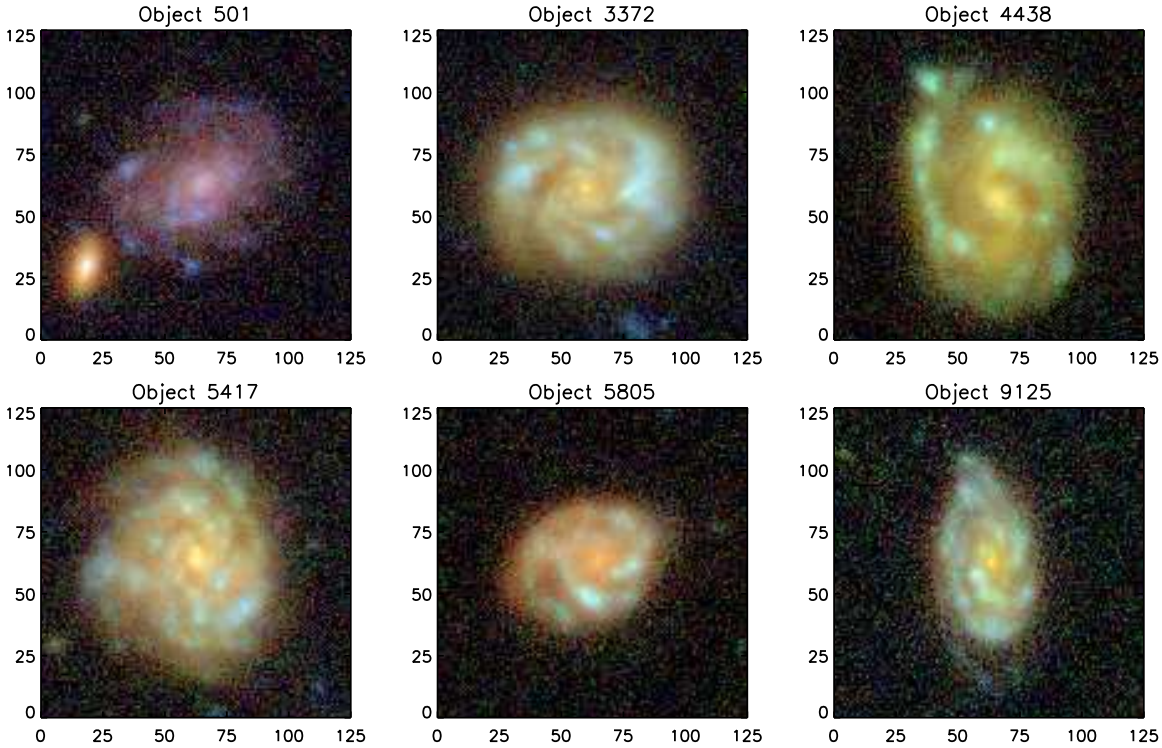

FIG. 18. Color composite images of a representative sample of late-type spiral galaxies at $z \simeq 1$. Axes show size of the stamp in pixels (0.″03/pixel). Note that all have small central bulges that are (in general) redder than their disks.

et al. 2006). The last column of Table 5 gives the observed (V–z') colors for these galaxies, corresponding to rest-frame (U–B) colors at $z \simeq 1$. Table 6 gives all available redshifts for these galaxies. The first 3 columns in Table 6 show the published HUDF IDs and coordinates, while the fourth column shows the photometric redshifts from the GRAPES spectro-photometric redshift catalog (for description, see Ryan *et al.* 2007) or the GOODS-MUSIC (MUltiwavelength Southern Infrared Catalog) catalog (Grazian *et al.* 2006). The fifth column of Table 6 gives the redshifts from GRAPES SED fitting as described later in this chapter. The last column of Table 6 gives the spectroscopic redshifts from VLT (Grazian *et al.* 2006; Vanzella *et al.* 2008), when available.

TABLE 5: Sample Properties of $z \simeq 1$ Galaxies

HUDF ID	RA J2000	DEC J2000	B mag[b]	V mag	i' mag	z' mag	$(V–z')$[a] color
501	53.1677662	−27.8166951	24.73	24.47	23.94	23.40	1.068
521	53.1699372	−27.8178736	26.27	25.98	25.28	24.94	1.041
901	53.1681788	−27.8129432	24.44	24.03	23.35	23.06	0.970
3048	53.1659121	−27.7997159	26.63	26.21	25.40	25.17	1.041
3299	53.1923333	−27.7978741	25.71	25.40	25.00	24.59	0.817
3372	53.1761793	−27.7961337	22.90	22.34	21.64	21.25	1.095
3373	53.1668679	−27.7976989	24.48	24.43	23.94	23.77	0.662
3613	53.1567527	−27.7955981	23.80	23.34	22.63	22.12	1.219
4072	53.1278092	−27.7950828	24.66	24.49	24.26	23.73	0.759
4084	53.1278372	−27.7947976	24.61	24.44	24.05	23.56	0.888
4438	53.1376781	−27.7919373	23.58	23.13	22.44	22.08	1.049
4491	53.1675702	−27.7925214	23.93	23.68	23.24	22.89	0.791
4591	53.1713278	−27.7929428	25.08	24.83	24.16	23.84	0.990
5190	53.1450905	−27.7894219	24.22	24.00	23.70	23.17	0.827
5405	53.1606000	−27.7897302	26.09	25.79	25.12	24.64	1.150
5417	53.1661791	−27.7875215	23.10	22.61	21.97	21.48	1.135

Continued on next page...

TABLE 5 – Continued

HUDF ID	RA J2000	DEC J2000	B mag[b]	V mag	i' mag	z' mag	$(V–z')$[a] color
5658	53.1740361	−27.7880062	24.99	24.61	23.99	23.43	1.178
5805	53.1920649	−27.7871824	23.91	23.58	23.04	22.57	1.011
5989	53.1609549	−27.7864996	24.81	24.58	24.05	23.55	1.028
6079	53.1394080	−27.7867760	25.76	25.35	24.78	24.12	1.222
6785	53.1915603	−27.7826687	24.15	23.88	23.57	22.97	0.907
6821	53.1782201	−27.7830771	24.13	23.90	23.47	23.04	0.865
7036	53.1903447	−27.7820005	24.43	24.29	24.09	23.57	0.714
7112	53.1658806	−27.7815379	24.65	24.09	23.41	22.83	1.258
7559	53.1587381	−27.7705348	23.93	23.54	22.86	22.48	1.057
8125	53.1729989	−27.7778393	23.95	23.85	23.45	23.14	0.716
8551	53.1517635	−27.7754183	23.90	23.42	22.71	22.25	1.173
8585	53.1479310	−27.7739569	22.42	22.13	21.63	21.15	0.973
9018	53.1470806	−27.7784243	24.44	24.32	23.96	23.66	0.663
9125	53.1663274	−27.7685923	24.13	23.83	23.36	22.71	1.121
9183	53.1601763	−27.7693039	24.86	24.80	24.40	24.18	0.611
9341	53.1598624	−27.7668404	24.88	24.68	24.12	23.72	0.953
9444	53.1554162	−27.7660748	25.81	24.91	24.04	23.34	1.572
9759	53.1596949	−27.7622834	24.76	24.62	24.34	23.82	0.803

[a] Observed $(V–z')$ color corresponds to rest-frame $(U–B)$ color at $z \simeq 1$.

[b] All magnitudes are in the AB photometric system.

TABLE 6: Redshifts for Sample Galaxies at $z \simeq 1$

HUDF ID	RA J2000	DEC J2000	z[c] phot	z[d] SED Fit	z[e] VLT
501	53.1677662	−27.8166951	1.07	1.02	—
521	53.1699372	−27.8178736	1.04	0.99	—
901	53.1681788	−27.8129432	0.94	0.88	—
3048	53.1659121	−27.7997159	0.84	0.85	—
3299	53.1923333	−27.7978741	1.06	1.20	1.221
3372	53.1761793	−27.7961337	1.04	0.98	0.996
3373	53.1668679	−27.7976989	0.89	0.93	—

Continued on next page...

TABLE 6 – Continued

HUDF ID	RA J2000	DEC J2000	z^{c} phot	z^{d} SED Fit	z^{e} VLT
3613	53.1567527	−27.7955981	1.07	0.98	1.097
4072	53.1278092	−27.7950828	1.27	1.20	1.189[f]
4084	53.1278372	−27.7947976	1.08	1.06	—
4438	53.1376781	−27.7919373	1.04	0.97	0.998
4491	53.1675702	−27.7925214	1.05	1.01	—
4591	53.1713278	−27.7929428	0.92	0.90	—
5190	53.1450905	−27.7894219	1.22	1.18	1.316
5405	53.1606000	−27.7897302	1.07	0.90	1.096
5417	53.1661791	−27.7875215	1.10	1.03	1.097
5658	53.1740361	−27.7880062	1.07	1.05	1.096
5805	53.1920649	−27.7871824	1.05	1.02	—
5989	53.1609549	−27.7864996	0.95	1.00	1.135
6079	53.1394080	−27.7867760	1.16	1.16	1.298
6785	53.1915603	−27.7826687	1.14	1.29	—
6821	53.1782201	−27.7830771	1.07	1.02	—
7036	53.1903447	−27.7820005	1.21	1.16	0.743[f]
7112	53.1658806	−27.7815379	1.07	1.04	—
7559	53.1587381	−27.7705348	0.96	0.93	—
8125	53.1729989	−27.7778393	1.05	1.04	—
8551	53.1517635	−27.7754183	1.05[c]	1.05	1.047
8585	53.1479310	−27.7739569	0.97	1.05	1.088
9018	53.1470806	−27.7784243	0.95	0.99	—
9125	53.1663274	−27.7685923	1.20	1.21	1.295
9183	53.1601763	−27.7693039	0.94	0.94	—
9341	53.1598624	−27.7668404	1.03	1.01	—
9444	53.1554162	−27.7660748	1.07	1.02	1.096
9759	53.1596949	−27.7622834	1.34	1.22	—

[c] From GRAPES photometric redshift catalog (Ryan *et al.* 2007).

[d] From GRAPES SED/4000 Å model fitting.

[e] From GOODS-MUSIC catalog (Grazian *et al.* 2006) and Vanzella *et al.* (2008).

[f] Quality flag on these spectroscopic redshifts is poor.

Observed color profiles. — We used the Interactive Data Language (IDL[5]) procedure `APER`[6] to compute aperture photometry using several aperture radii. We chose our starting aperture radius to be 2.5 ACS pixels ($\sim$0.″1), because the width of the narrow extraction window (see Pirzkal *et al.* 2004, for extraction details) of our GRAPES spectra is 5 pixels. We measured aperture magnitudes for all galaxies in our sample in all four ($BVi'z'$) ACS bands with aperture radii ranging from 2.5 pixels to 35 pixels. Using these aperture magnitudes, we measured the (V–z') color profiles for our galaxies. Figure 19 shows these color profiles for 6 galaxies. This figure show that the inner-disk in most of these galaxies is red, and dominated by the older stellar population. Our galaxies show that for all apertures the (V–z') color is redder than 0.9, with redder colors at smaller aperture sizes (the central bulge region).

Figure 20 shows the observed (V–i') color as function of redshift for bulges and spheroids. The black dots correspond to our sample of HUDF/GRAPES bulges. The crosses are the GOODS/HDF-N spheroids presented by MacArthur *et al.* (2008), and the filled triangles are the GOODS/CDF-S early-type galaxies from Ferreras *et al.* (2005). The lines represent the expected color evolution for a set of star formation histories using the population synthesis models of Bruzual & Charlot (2003). The thick lines track the color evolution for a stellar population with solar metallicity and an exponentially decaying star-formation rate, starting at $z_F = 5$, with an exponential decay timescale of 0.5 (solid), 1 (dashed) and 8 Gyr (dotted). The thin solid line shows the expected color evolution for a decay timescale of 0.5 Gyr and 1/3 of solar

[5]IDL Website http://www.ittvis.com/index.asp

[6]IDL Astronomy User's Library Website http://idlastro.gsfc.nasa.gov/homepage.html

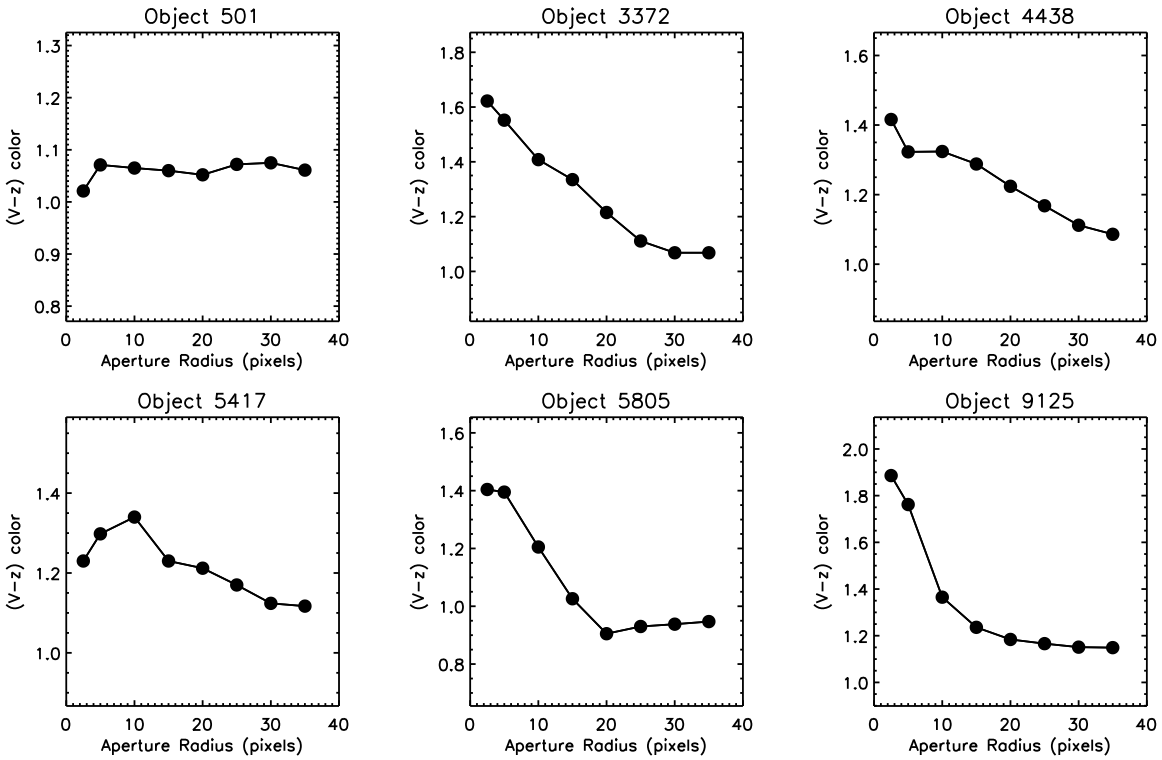

FIG. 19. Observed (V–z') colors measured using aperture magnitudes from eight different size apertures. Here we show colors for six sample galaxies. These are the same six galaxies as shown in Figure 18. Note that with the exception of object ID 501, all these galaxies become bluer from the inside outwards.

metallicity. Most of the bulges in early-type galaxies in GOODS/CDF-S (Ferreras *et al.* 2005; MacArthur *et al.* 2008) are consistent with short decay timescales, while the bulges in our late-type spiral sample agree better with a more extended star formation history. This figure shows that the bulges explored in this paper belong to a similar population as the "blue early-types" presented in Ferreras *et al.* (2005). This blue population constitutes ∼20% of the total sample of early-type systems visually selected in GOODS/CDF-S. Because of the excellent photometric depth of the HUDF, our sample extends the bulge redshift distribution of MacArthur *et al.* (2008) to $z \simeq 1.3$.

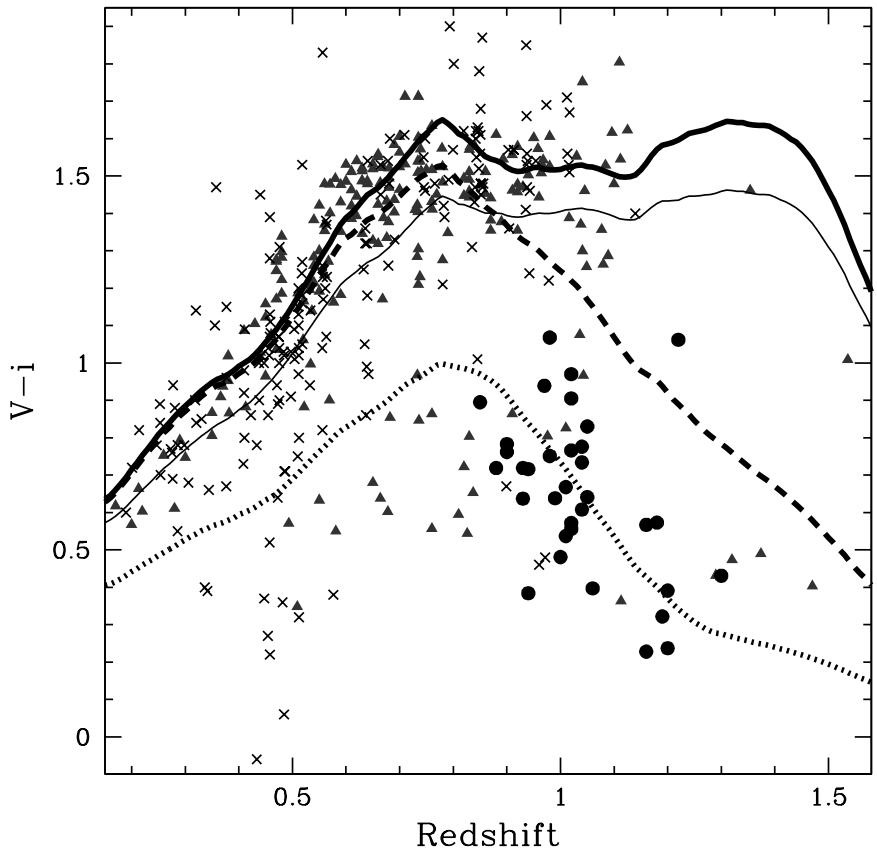

FIG. 20. (V–i') vs. redshift. The black dots correspond to our sample of bulges. The crosses are the spheroids presented by MacArthur *et al.* (2008), and the triangles are the early-type galaxies from Ferreras *et al.* (2005). The lines represent the color evolution of a set of SFHs from models of Bruzual & Charlot (2003). The thick lines track the color evolution of a stellar population with solar metallicity and an exponentially decaying SFR, started at $z_F = 5$, with a decay timescale of 0.5 (solid), 1 (dashed) and 8 Gyr (dotted). The thin solid line shows the evolution with a timescale of 0.5 Gyr at 1/3 of solar metallicity.

4.4. *Morphological Properties*

We performed a morphological analysis of the sample galaxies in two steps: (a) a non-parametric analysis of the distribution of the galaxy light, using the measures of concentration, asymmetry, and clumpiness to confirm our visual inspection; (b) a two dimensional decomposition performed with GALFIT (Peng *et al.* 2002), in order to quantify the galaxy morphology and in particular to extract their Sérsic indices.

CAS measurements. — We use the classical Concentration (C), Asymmetry (A) and clumpinesS (or smoothness) — the CAS parameters (Conselice *et al.* 2000; Conselice 2003) — to carry out the non-parametric approach to quantify morphology. We computed the C and A values for our galaxies following the definitions and methods as discussed in Conselice *et al.* (2000). The Concentration index correlates with the Sérsic index and the Bulge-to-Disk (B/D) ratio: high C-values correspond to early-type morphology, while lower C-values are suggestive of a disk-dominated or later-type and irregular galaxies. Asymmetry can distinguish irregular galaxies or perturbed spirals from relaxed systems, such as E/S0 and normal spirals. Clumpiness quantifies the degree of structure on small scale, and roughly correlates with the rate of star-formation. We derived the Concentration and Asymmetry indices using the images taken in the z'-band, which roughly corresponds to the rest-frame B-band at $z \simeq 1$. Our measurements of C and A are shown in Figure 21, together with the mean loci for nearby early-, mid- and late-type galaxies as derived by Bershady *et al.* (2000). A few perturbed galaxies show higher asymmetry values. Figure 21 clearly shows that our sample of galaxies consists of mostly late-type galaxies, and confirms our visual morphological classification of late-type galaxies with bulges.

Two-dimensional (2D) galaxy fitting using GALFIT. — GALFIT (Peng *et al.* 2002) is an automated algorithm to extract structural parameters from galaxy images by fitting/decomposing these with one or more analytic 2D functions. It offers different parametric models (the "Nuker" law, the generalized Sérsic–de Vaucouleurs profile, the exponential disk, and Gaussian or Moffat functions), and allows multi-

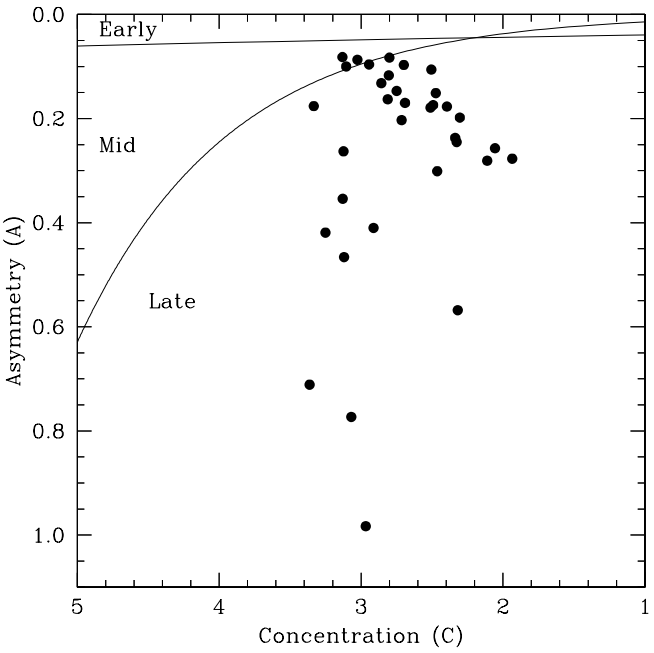

FIG. 21. Asymmetry and Concentration values for the selected late-type galaxies. The distinction between early-, mid- and late-type galaxies is from Bershady *et al.* (2000) and Conselice *et al.* (2005). It is clear that nearly all our disk galaxies containing (small) bulges are classified as late-type spirals.

component fitting, which is useful to measure B/D or Bulge-to-Total (B/T) light ratios.

Thumbnail image extraction: The GALFIT disk+bulge decompositions were performed on thumbnail (or "postage stamp") images extracted around the objects in our sample, rather than on the entire science image itself. Three thumbnail images for each object were extracted from the original HUDF images. All thumbnail images are 201×201 pixels ($\sim 6\farcs0 \times 6\farcs0$) in size. The first thumbnail was extracted from the science image itself. The second thumbnail was extracted from the comprehensive segmentation image generated by Coe *et al.* (2006), which was used as the "bad pixel map/mask" image used in GALFIT. GALFIT uses this "mask" image so that all non-zero valued pixels are ignored in the fit. Hence, the extracted segmentation stamps were modified, so that only pixels belonging to the galaxy had zero value, while any pixels belonging to another object are set to a non-zero value. We tested

this GALFIT decomposition with and without bad pixel maps for comparison, and obtained very similar fitting results. The third thumbnail was extracted from the drizzle-generated weight image (Koekemoer *et al.* 2002). These weight images were modified for GALFIT (C. Peng, private communication) as follows. First, the science image was smoothed by a few pixels to get rid of some of the random pixel-to-pixel variations. Second, a variance image S, was calculated using $S = (1/wht) + data/exptime$, where, wht is the drizzle-generated weight image, $data$ is the science image in counts/sec and $exptime$ is the total exposure time of the image. Finally, a sigma image is generated using $\sigma = \sqrt{S}$. These modified weight images were used as the input "sigma" image (noise maps) in the GALFIT, which is necessary for proper error-propagation.

Sky background: The drizzled HUDF images are sky subtracted and therefore, to understand the effects from the sky-subtraction errors, we used the following procedure. A careful analysis of the HUDF sky-background and its corresponding uncertainties was performed by Hathi *et al.* (2008b). We used these sky-background values from Hathi *et al.* (2008b), and allowed GALFIT to either vary this sky-level during the fitting process, or keep it fixed. For comparison, we also used the sky-background measured from each individual object stamp, and repeated the process. We also tested our GALFIT decomposition by comparing the results from GALFIT with and without the addition of the sky-background. We found very consistent and similar fitting parameters from all these tests. Therefore, we adopted the sky-background levels measured by Hathi *et al.* (2008b) in our final GALFIT decomposition.

Using GALFIT: GALFIT produces model images of galaxies based on initial input parameters. These images are convolved with the ACS Point Spread Function (PSF) image before comparing with the actual galaxy image. Fitting proceeds iteratively until convergence is achieved, which normally occurs when the χ^2 does not change by more than 5 parts in 10^4 for successive five iterations (See Peng *et al.* 2002). GALFIT requires initial guesses for the fitting parameters. Following Dong & De Robertis (2006) and Simien & de Vaucouleurs (1986), we used the output parameters from the published HUDF SExtractor catalogs (Beckwith *et al.* 2006) as input values for the magnitude, the half-light radius, the position angle, and the ellipticity of each object. The initial value for the Sérsic index, n, was taken to be 1.5 (Coe *et al.* 2006). Tests based on an adopted initial value of n=4 showed similar results.

All GALFIT measurements were obtained from the V- and z'-band images (approximately rest-frame U- and B-band, respectively). First, we fitted only an one-component Sérsic profile to our galaxies to improve the initial estimates for the Sérsic index, the axis ratio and the position angle of each galaxy. The distribution of Sérsic indices for our galaxies in the V- and z'-band is shown in Figure 22. Our measurements of the Sérsic index in V- and z'-band are comparable to i'-band values of the galaxies in Coe *et al.* (2006). Figure 22 confirms that most of the galaxies in our sample have a Sérsic index $n < 2$ in both V- and z'-bands, which implies that our galaxies are disk-dominated, as Figure 18 and Figure 19 clearly suggest.

Next, we simultaneously fitted two components: a Sérsic profile plus an exponential disk profile, to get better estimates of the bulge and disk magnitudes, respec-

tively. For this simultaneous fit, we kept the coordinates of the galactic center (within ± 1 pixel constraint), the axial ratio and the position angle fixed, while we allowed GALFIT to fit m_{bulge}, m_{disk}, R_e, R_s and the the Sérsic index (n). For all galaxies in our sample, we obtained better fits for $b$ulge Sérsic indices of $n \lesssim 1.0$. We also tested our runs by fixing initial value of n=1 for all galaxies and found that GALFIT converged to similar solutions in the end. The bulge and disk models obtained from these best fits were then used to estimate the B/D ratio. We used an aperture of 5 pixels diameter to measure the B/D and B/T ratios, which used the same aperture size as for extracting the GRAPES SEDs. The majority of our galaxies show a B/D value <1 within this aperture. For larger apertures encompassing the galaxies' total light, B/D appears to be << 1, in agreement with our galaxies being disk-dominated (i.e., late-type galaxies).

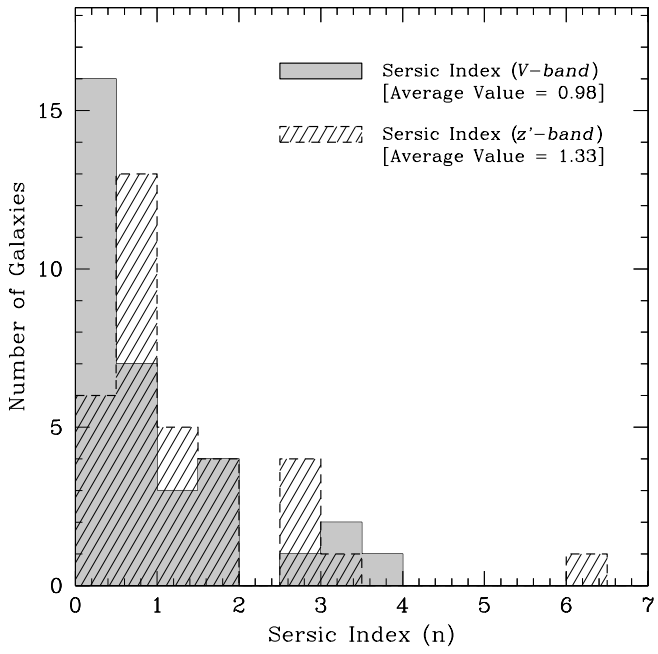

FIG. 22. The distribution of Sérsic indices (n) for the galaxy retrieved from GALFIT single component Sérsic fit to galaxies in V- and z'-band. The mean values of n is reported in top right corner. Using a two-sided K-S test on these distributions, we cannot reject the hypothesis that the V- and z'-band distributions are drawn from the same population.

4.5. *Stellar Population Models*

The GRAPES grism spectra were taken at five different position angles (PAs) to remove any contamination and overlap from nearby objects. We generated one final spectrum for each galaxy by combining all of the GRAPES spectra obtained at the 5 different PAs. The combination was performed as a simple averaging operation, after resampling the spectra onto a common wavelength grid. Portions of spectra which were contaminated more than 25% (see Pirzkal *et al.* 2004, for a description) were not used, unless absolutely necessary. The Poisson errors were propagated, and the standard deviation of the mean between the 5 individual PAs was computed. The larger of either the Poisson noise or the standard deviation of the mean was used in the subsequent analysis. Our goal is to fit stellar population models to the age-sensitive 4000 Å break observed in the GRAPES spectra of these galaxies.

Star formation histories (SFH). — We fit our ACS grism spectra to a grid of models obtained by combining the simple stellar populations of Bruzual & Charlot (2003). A standard χ^2 method is used. We explore a wide volume of parameter space in order to infer robust constraints on the possible ages and metallicities of the stellar populations in the central bulges of these galaxies. This comparison requires a careful process of degrading the synthetic SED (resolution $R \sim 2000$) to the (variable) resolution of the GRAPES spectra. Special care must be taken with respect to the change of the Line Spread Function (LSF) with wavelength, which results in both an effective degradation of the spectral resolution as a function of wavelength, and a different net spectral resolution with respect to the size of the galaxy. After exploring

a range of values $R = 30 - 80$, we find that an effective resolution of $R = 50$ is suitable for all the spectra in our sample. The ACS grism spectral resolution is not degenerate with respect to parameters describing the star-formation history, and mostly results in a global shift of the likelihood.

In order to determine the redshift as accurately as possible, we start with some guessing values obtained from three sources: a photometric redshift; a VLT spectroscopic redshift — where available — and a redshift estimate taken from an automated method (as discussed in 'Sample selection' section) to search for a prominent 4000 Å break in GRAPES data. A small set of templates at the GRAPES resolution were used to determine the best redshift for each galaxy, using the guessing values described above as a starting point, and performing a simple cross-correlation for a range of redshifts until the best match is found. This method generates the redshifts used throughout this paper, shown in Table 6 as "SED Fit".

In order to make a robust assessment of the ages and metallicities of the unresolved stellar populations, we use two different sets of models to describe the build up of the stellar component. The models depend on a reduced set of parameters, which can characterize a star-formation history in a representative fashion.

Model #1 (EXP): We take a simple exponentially decaying star formation rate, so that each star-formation history is well parametrized by a formation epoch, which can be described by a formation epoch ($t(z_F)$); a star-formation timescale ($\tau_\star = 0.1 \rightarrow 4$ Gyr); and a metallicity ($[m/H] = -1.5 \rightarrow +0.3$), which is kept fixed at all times. The numbers in brackets give the range explored in the analysis of the model

likelihood. The range in formation epochs is chosen from $z_F = 10$ to $t(z_F) = 0.2$ Gyr (this range depends on the observed redshift of the galaxy).

Model #2 (CSP): We follow a consistent chemical enrichment code as described in Ferreras & Silk (2000). The model allows for gas infall and outflow. The metallicity evolves according to these parameters, using the stellar yields from Thielemann *et al.* (1996) for massive stars ($> 10M_{\odot}$), and van den Hoek & Groenewegen (1997) for intermediate mass stars. The free parameters are the formation epoch (same range as the one chosen for Model #1), the timescale for the infall of gas ($\tau_f = 0.1 \rightarrow 1$ Gyr), and the fraction of gas ejected in outflows ($B_{\rm OUT} = 0 \rightarrow 1$). The star-formation efficiency is kept at a high value $C_{\rm EFF} = 20$ as expected for early-type populations (see Ferreras & Silk 2000).

For each of the two sets of models we run a grid of SFHs, convolving simple stellar populations from the models of Bruzual & Charlot (2003). The grid spans $64 \times 64 \times 64$ SFHs (note that three free parameters are chosen in each set) over a wide range of values as shown above. Once the best fit is obtained within the grid, we run a number of models with random values of the parameters with an accept/reject criterion based on the likelihood – analogous to the Metropolis algorithm, e.g., Saha (2003). The process ends when 10,000 models are accepted. The total number of accepted models determine the median and confidence levels of the parameters. The distribution of reduced χ^2 values has an average of χ^2=0.74 and RMS $\sigma(\chi^2) = 0.35$. The χ^2 used throughout includes a mild Gaussian prior on the metallicity with average [m/H]$= -0.1$ and RMS $\sigma([m/H]) = 0.5$. This prior allows for a relatively wide

range of average metallicities, and is compatible with the values commonly found in these systems (e.g., Carollo *et al.* 2007). The distribution of bulge metallicities ($\log(Z/Z_{\odot})$) estimated from the stellar population models is shown in Figure 23. The data point shows the average value and rms scatter of the distribution. A mild Gaussian prior on the metallicity with average [m/H]$= -0.1$ and RMS $\sigma([m/H]) = 0.5$ is overplotted on the distribution. Figure 23 clearly shows that the metallicity prior still allows for a wide range of average metallicities. The average metallicities obtained from our models is comparable with the values obtained at $z \simeq 1$ from ground-based spectroscopic observations (e.g., Shapley et al. 2005; Schiavon et al. 2006; Liu et al. 2008), which was our main motivation to include metallicity priors in first place. Using a flat prior instead yields very similar results.

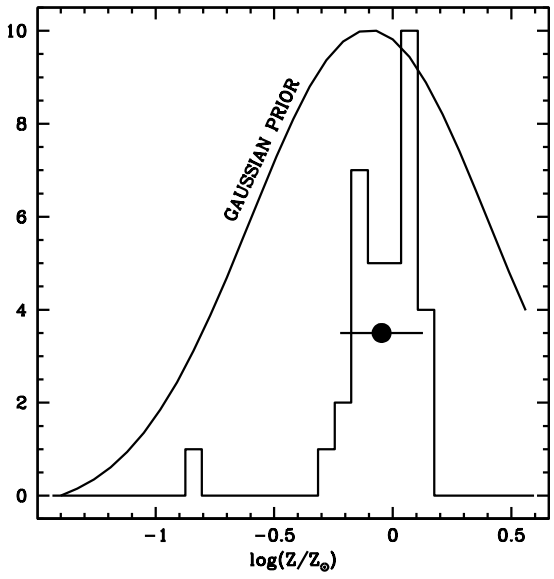

FIG. 23. The distribution of bulge metallicities ($\log(Z/Z_{\odot})$) estimated from the stellar population models. The data point shows the average value and rms scatter of the distribution. We overplot a mild Gaussian prior used on the metallicity with average [m/H]$= -0.1$ and RMS $\sigma([m/H]) = 0.5$. It is clearly shown that this metallicity prior still allows for a wide range of average metallicities, and is compatible with the values obtained at $z \simeq 1$ from ground-based spectroscopic observations (e.g., Shapley et al. 2005; Schiavon et al. 2006; Liu et al. 2008).

Figure 24 shows the best fit models and the observed SEDs for 10 galaxies in our sample. The error bars represent the observations, and the solid line correspond to the best fits for the CSP model. The wavelength is shown in the observed frame,

whereas the wavelength range chosen for all galaxies is 3800–5000 Å *in the rest-frame*. This choice ensures a consistency in the comparison of the stellar populations in our sample. The chosen range straddles the age-sensitive 4000 Å break.

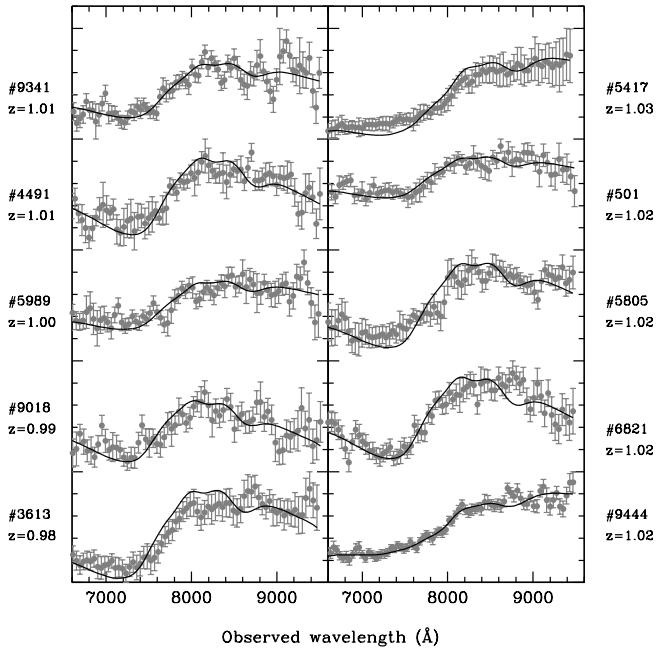

FIG. 24. Spectral energy distributions of 10 galaxies in our sample (Each one is labeled with the HUDF numbers and model redshifts). The error bars are the observed ACS/G800L data and the lines are the best fits according to the CSP models (see text for details). The distribution of reduced χ^2 values has an average of χ^2=0.74 and RMS $\sigma(\chi^2) = 0.35$.

Figure 25 shows the 4000 Å break amplitude, D4000, as a function of stellar age. The distribution of bulge ages is overplotted as histogram, which agrees very well with the range in D4000 (which is 1.2 to 1.5 in general) that we obtain, as shown in Figure 17. Different curves show three simple stellar population models with three different metallicities. For metallicity around solar (thick-solid and dashed lines), which we obtain for our bulges, the variation in D4000 with age is very similar. For solar metallicity with E(B–V)=0.2 dust reddening (thin-solid line) and for high metallicity (dotted line), the relation is somewhat steeper. Figure 25 shows that for the range in D4000 and metallicities of our sample, the effect of metallicity on D4000 small, and D4000 is a good age indicator for this sample.

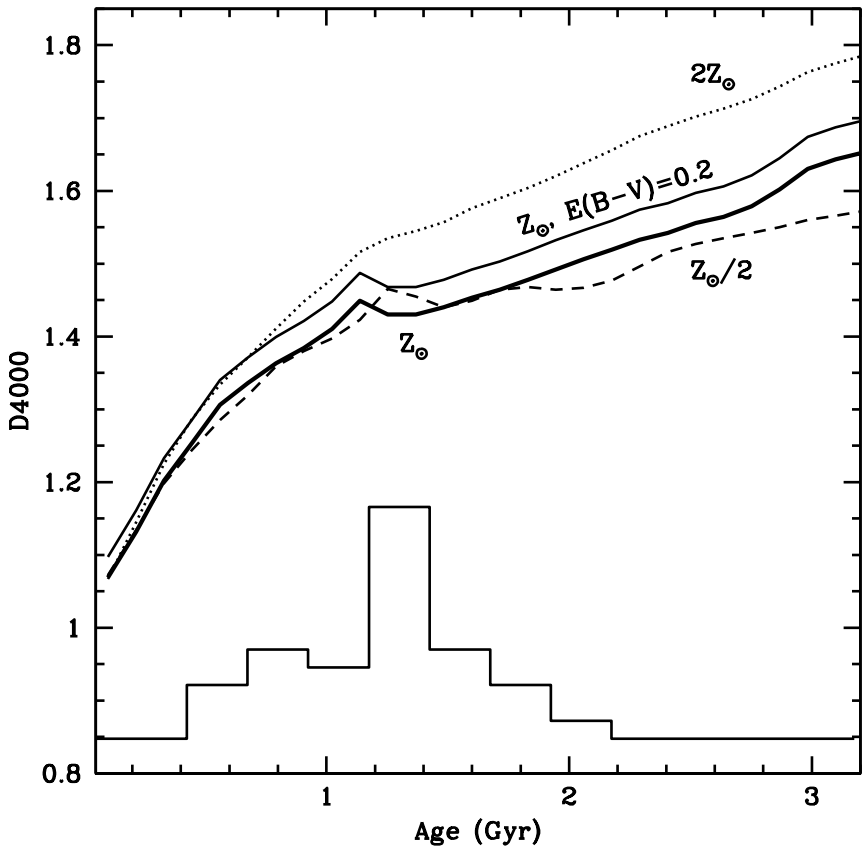

FIG. 25. The D4000 as a function of stellar age. The distribution of bulge ages is overplotted as histogram, which agrees very well with the range in D4000 (which is 1.2 to 1.5) we get as shown in Figure 17. Different curves show three simple stellar population models with three different metallicities. For metallicity around solar (thick-solid and dashed lines), which we are getting for our bulges, the variation in D4000 with age is very similar, and so a slight change in metallicity does not affect D4000. For solar metallicity with 0.2 dust reddening (thin-solid line) and for high metallicity (dotted line), the relation is little steeper.

Figure 26 shows the ages and metallicities of the best SFHs for each bulge. The average and RMS scatter for age and metallicity are shown as dots and error bars, respectively. For the EXP models – which have zero spread in metallicity – the error bars in metallicity represent the uncertainty estimated from the likelihood. The solid lines in the lower panels correspond to the age of the Universe as a function of redshift.

The dashed lines show the age that a *simple stellar population* – a population with a single age – would have if formed at redshifts (from top to bottom) $z_F = \{5, 3, 2\}$. The median value of the stellar ages of our bulges is 1.3 Gyr. The CSP models treat chemical enrichment in a more consistent way than the EXP models and should therefore better reflect the true populations.

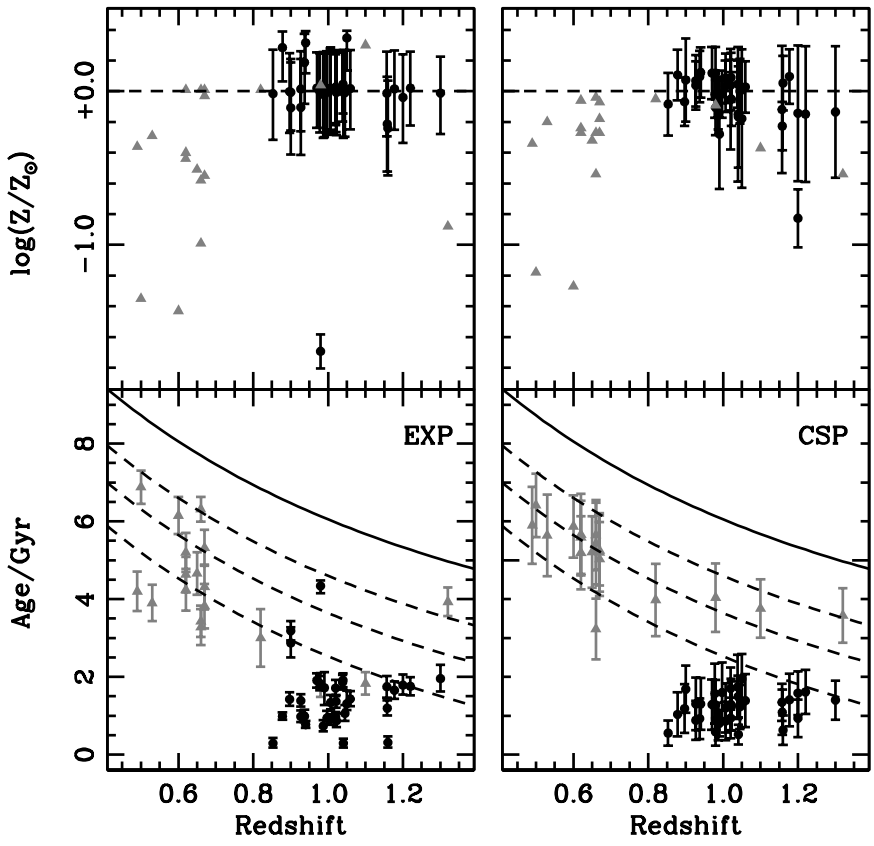

Fig. 26. Ages and metallicities corresponding to the best fit according to a simple exponentially decaying model (EXP; [**Left**]) or a consistent chemical enrichment code (CSP; [**Right**]). The filled circles are the average values of age or metallicity and the error bars represent the RMS of the distribution. The solid lines in the bottom panel track the age of the Universe at a given redshift for a concordance cosmology. The dashed lines – from top to bottom – correspond to formation redshifts of $z_F = \{5, 3, 2\}$. The dashed lines correspond to the age of simple stellar populations formed at $z_F = \{5, 3, 2\}$ (i.e., if they had an e-folding timescale τ_f=0). The triangles are the lower redshift early-type galaxies from Pasquali *et al.* (2006b), which were analyzed the same way.

We would emphasize here that it is the *average* stellar age that can be reasonably constrained with the data. Therefore, Figure 26 does not imply that all stars in these bulges are ∼1.3 Gyr but many may be older. To clarify, the formation epoch (characterized by a formation redshift) is the age when star formation starts in the model. Figure 27 shows the formation redshift (z_F) and the e-folding timescale (τ_f) corresponding to the best fit stellar population models. Here, z_F is the epoch at which the model starts star-formation (as described earlier), and τ_f is the e-folding timescale of star-formation, with shorter timescales ($\lesssim$0.5 Gyr) corresponding to a more elliptical-type old stellar population. We see a large spread in both z_F and τ_f, but with a clear indication that most low mass bulges have a more extended star-formation history ($\tau_f \gtrsim 1$ Gyr) and a lower formation redshift ($z_F \lesssim 2.5$). Hence, most of our bulges appear to have an extended SFHs. We also include a characteristic error bar showing uncertainties in these values.

The best-fit stellar population models show that our bulges have similar ages independent of redshift. This similarity in ages could be due to two possible reasons. First, our galaxy sample has a redshift range from $z \simeq 0.8$ to 1.3, but most of our galaxies are in much smaller redshift range from $z \simeq 0.9$ to 1.1. We have applied same selection criteria to all of our galaxies in a small field so it is possible that we have selected similar kind of galaxies/bulges with similar bulge ages in this small redshift range. Secondly, Vanzella *et al.* (2006) has predicted Large Scale Structure (LSS) in the CDF-S around $z \simeq 1.0$ from VLT spectroscopic redshifts. Redshift distribution in the HUDF (smaller field in the CDF-S) also show a strong peak around $z \simeq 1.0$. So

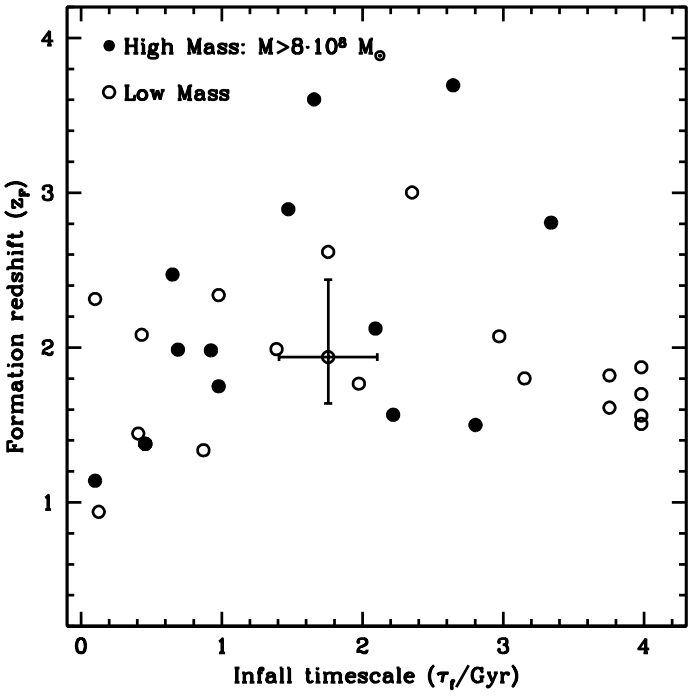

FIG. 27. Formation redshift (z_F) and the e-folding timescale (τ_f) corresponding to the best fit stellar population model. z_F is the epoch at which we start star-formation (as described in the text) and τ_f is the e-folding timescale of star-formation, with shorter timescales corresponding to an elliptical-type old population. There is a large spread in both z_F and τ_f, but with a clear indication that many low mass bulges may have had an extended star-formation history ($\tau_f \gtrsim 1$ Gyr) and a lower formation redshift ($z_F \lesssim 2.5$). We also include a characteristic error bar showing the typical fitting uncertainties in these values.

it is possible that we may be looking at a smaller subset of this LSS at $z \simeq 1.0$.

Bulge mass estimates. — The photometry from Table 5 can be combined with the M/L ratios obtained from the best-fit SFH to constrain the stellar mass (M_s) content of the bulges. This M/L is derived from the composite model obtained by combining the simple stellar populations from Bruzual & Charlot (2003) using a Chabrier (2003) Initial Mass Function (IMF). If we change the IMF from Chabrier (2003) to Salpeter (1955), the stellar mass will increase by $\sim$0.3 dex in $log(M_s)$, which within the other errors in data and models, does not change our overall results. The

photometry has to be corrected to take into account contamination from the disk. We use the B/D ratio obtained from the GALFIT to estimate the bulge fraction of the light in the galaxy. The stellar mass estimates for our bulges are in the range of $6.5 \leq log(M_s/M_\odot) \leq 10.0$.

Disk contamination. — The best-fit stellar population models to the GRAPES SEDs suggests that the late-type bulges at $z \simeq 1$ are young, with an average age of $\sim$1.3 Gyr. To better understand this result, we first need to quantify the effect of disk contamination in our measurements. The GRAPES SEDS are extracted from an aperture of relatively narrow-width aperture (5 pixels in diameter) around the center of each galaxy. The narrow extraction of the grism spectra is dominated by the bulge and the inner disk light. The extracted spectra clearly show 4000 Å breaks in all uncontaminated PAs, due to the older stellar population in the central region of the galaxy. We fit our stellar population models to this break only and hence, we need to investigate the spectral contamination due to the inner disk in these age estimates. We perform following photometric tests to understand the effect of the inner disk on the bulge ages.

(1) We used the disk and bulge light profiles produced by GALFIT and measured their flux in a strip 5 pixel wide and around their common center, to estimate the disk and bulge light-fraction within this aperture. We find that the light contributed by the disk to the total flux in this aperture can be as high as 30%. At the same time, we measured the disk and bulge colors within the same aperture, to find that the disk and the bulge are similar within the photometric errors, so that the disk

contamination in the bulge spectrum is not expected to dominate our estimate of the bulge age. This can be already be seen in Figure 19, where the bulge is in general 0.3–0.8 mag redder in (V–z') than the disk.

(2) We compared the bulge age derived from the stellar population models with the color difference between two apertures. We measure the color difference between two apertures with 2.5 pixels and 5 pixels radii, equivalent to the narrow and wide GRAPES spectral extractions, respectively. The top panel of Figure 28 shows the comparison between the color difference and the bulge age. The points on the plot are color-coded according to their B/D ratios, measured from GALFIT. Blue color stands for B/D$\leq$0.5, green means 0.5<B/D$\leq$1 and red represents B/D>1. The top panel of the Figure 28 does not show any major trends among age, color difference, and B/D ratio. Secondly, we compared the bulge age to the color difference between the 2.5 pixels aperture and the annulus defined by the 2.5 and 5 pixels apertures. The bottom panel of the Figure 28 shows this comparison. The points on the plot are color-coded according to their B/D ratios, as in the top panel. Like the top panel, the bottom panel of Figure 28 does not show any major correlation among age, color difference, and B/D ratio. Finally, we directly compared the B/D ratio with the age and mass of the bulge. The top panel of Figure 29 shows the comparison between the B/D ratios obtained from the GALFIT and the bulge age from the stellar population models for all galaxies in the sample. Figure 29 does not show any correlation between the age and the B/D ratio. Similarly, the bottom panel of Figure 29 shows at best a very mild correlation between the bulge stellar mass and the B/D ratio.

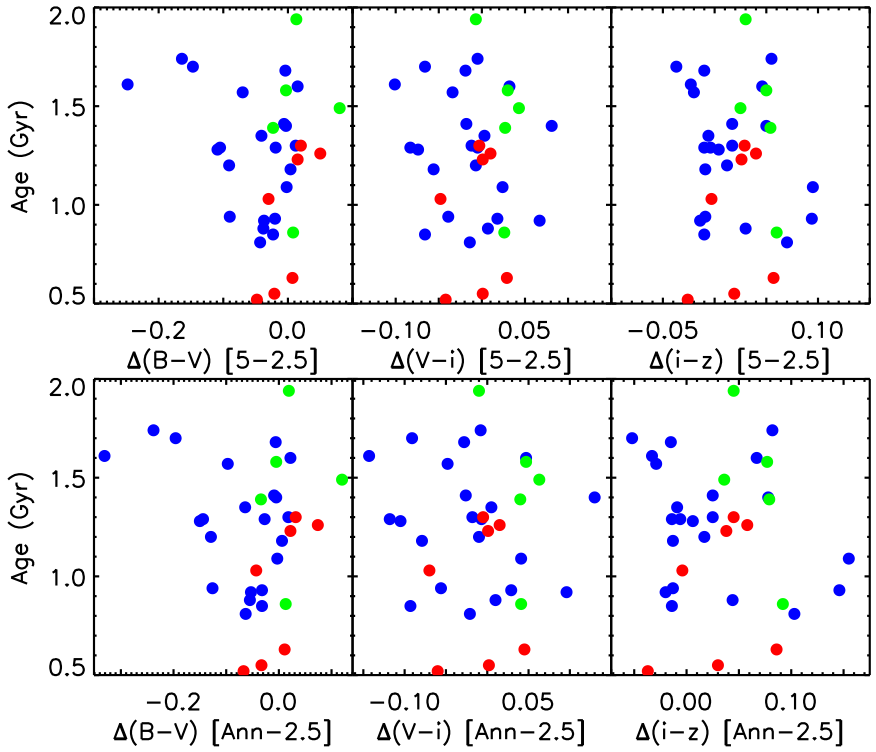

FIG. 28. Comparison between aperture colors and the best-fit bulge age. [**Top**] shows the bulge age as a function of the color difference between the 2.5 pixels aperture and the 5 pixels aperture. [**Bottom**] shows the bulge age as a function of the color difference between the 2.5 pixels aperture and the annulus defined by the 2.5 and 5 pixels apertures. A blue colored circle stands for B/D$\leq$0.5, green means 0.5<B/D$\leq$1 and red represents B/D>1. Here B/D is measured in the i'-band. Both panels does not show any correlation among the age, color difference, and B/D ratio.

(3) For a few sample galaxies, we extracted the spectrum of their disk above and below the bulge aperture used to extract the bulge spectrum, at a distance of approximately 10 pixels from the galaxy center. Similarly to its bulge, the disk also exhibits a 4000 Å break in the spectrum whose amplitude is only slightly smaller (within few percents) from that of the bulge. This test shows that both bulges and inner disks are comparably red/old. We also fitted stellar population models using both the bulge and disk spectra, and analyzed how the bulge-age and metallicity

change as a function of disk contamination, i.e., the fraction of disk light added to the bulge spectrum. Our simulations show that the determination of the bulge age is not dominated by disk contamination. Even when disk contamination is completely ignored – or fully subtracted – the bulge ages do not change much.

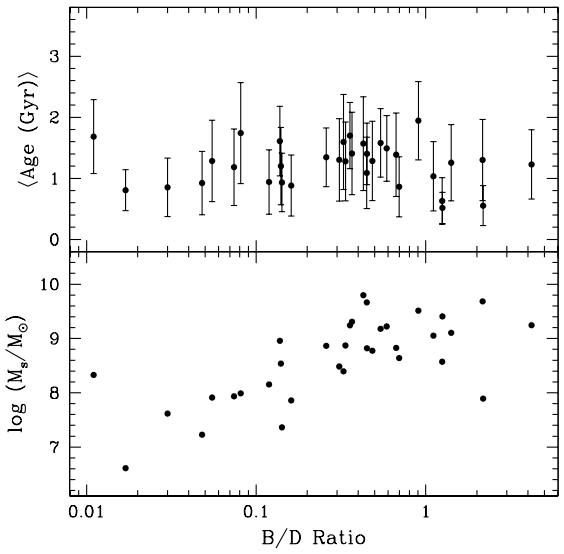

FIG. 29. Correlation between measured B/D ratio from GALFIT and the CSP model parameters age and mass. The top panel shows that there is no correlation between the B/D ratio and the bulge ages for late-type galaxies. The bottom panel shows at best a very mild correlation between the B/D ratio and the mass of these late-type bulges.

In summary, we do not detect any significant correlation between the bulge age, B/D ratio and the aperture color difference. We thus conclude that our estimate of the bulge ages is fairly robust, and that the younger age of the sample bulges is likely real and not due to disk contamination.

4.6. *Discussion*

The ages and masses of late-type bulges are estimated by fitting our GRAPES SEDs with stellar population models. Our analysis shows that bulges in late-type galaxies at higher redshift ($z \simeq 1$) appear to be relatively young (average age$\sim$1.3 Gyr) and less massive ($6.5 \leq log(M_s/M_\odot) \leq 10.0$) compared to early-type galaxies at same redshift. This finding appears to be independent of the relative amount of

disk-light present, or the color of the underlying disk. Figure 30 shows the stellar masses of our bulges (filled and open circles) compared with the best-fit ages from the CSP models. We also include the stellar mass estimates for the elliptical galaxies from GRAPES/HUDF (grey triangles; Pasquali *et al.* 2006b), which were analyzed in a similar way. Their sample of early-type galaxies covers a lower range of redshifts ($0.5 \leq z \leq 1.0$). Hence, for a proper comparison, we divide our bulges with respect to redshift: $z \leq 1$ (solid circles) and $z > 1$ (open circles). The bulges in our late-type spirals span a much lower range of ages, and have lower masses, compared to those of early-type galaxies.

Elmegreen *et al.* (2005) have classified ∼900 galaxies (larger than 10 pixels or 0.″3) in the HUDF according to morphology and their photometric properties. They find 269 spiral galaxies in the HUDF. Using the Elmegreen *et al.* (2005) morphological classifications, and accurate spectro-photometric redshifts from Ryan *et al.* (2007), we estimate that the results in this paper represent approximately ∼40–50% of the total late-type/spirals HUDF galaxy population within the magnitude and redshift range used in this paper.

Our analysis of the central and the inner disk colors of these galaxies (Figure 19) and their grism spectra shows that the inner disk and the bulge components have similar colors, and that the bulge ages are not significantly affected by the light (and stellar populations) of the underlying disk. This result is consistent with the idea that the inner disk of galaxies in general has similar colors and age as the bulge (e.g., Peletier & Balcells 1996). The effect of dust on these measurements should not be

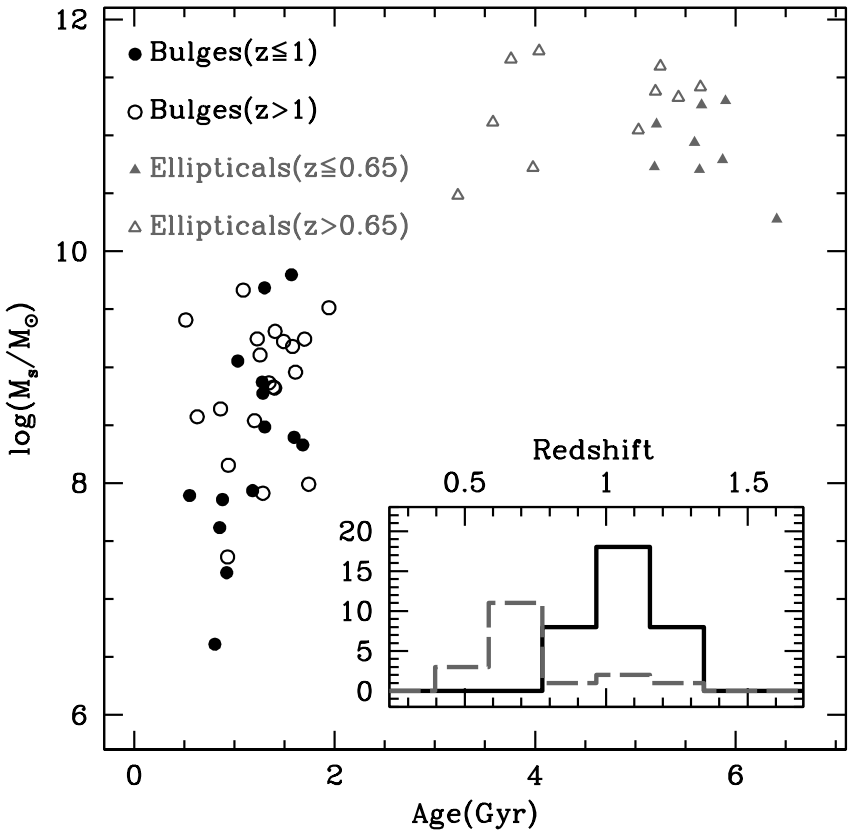

FIG. 30. Comparison between bulges in early-type (grey triangles/dashed lines) and late-type galaxies (black circles/lines). Measurements for early-type galaxies are discussed in Pasquali *et al.* (2006b). Inset shows redshift distribution for both these samples with ellipticals peaking at $z \simeq 0.7$. Early-type galaxies are mostly at $z < 1$, therefore we divide our late-type bulges into $z \leq 1$ (filled circles) and $z > 1$ (open circles). It is clear that for similar redshifts, bulges in late-type galaxies are younger and less massive compared to bulges in early-type galaxies.

significant, since our bulge ages are based on the amplitude of the 4000 Å observed in the GRAPES grism spectra, which is sensitive to age rather than to dust. Also, MacArthur *et al.* (2004) argue that dust is generally not a significant contributor to galaxy colors in low-mass/low-luminosity spiral galaxies, but is likely important in more massive/brighter galaxies. On the other hand, even if dust plays an important role in this analysis, then inclusion of dust will make our ages still younger, and our

result that bulges and inner-disks have similar dominant stellar population with an average age of $\sim$1.3 Gyr should then be viewed as an upper limit.

We performed GALFIT decomposition on the sample galaxies by simultaneously fitting the bulge to a Sérsic profile and the disk to an exponential profile. For all bulges in our sample, we obtained better fits using Sérsic indices of $n \lesssim 1.0$. Therefore, these bulges are disk-like (Kormendy & Kennicutt 2004; Athanassoula 2005) and have radial surface brightness profiles similar to disks. Similar analyses for local spirals by de Jong (1996) and Courteau *et al.* (1996) have shown that the majority of bulges in late-type galaxies are better fit by exponential profile. Our results show that a similar trend also exists at $z \simeq 1$. The similarities we find in the bulge and the inner-disk properties (4000 Å break, colors and profiles) could imply that these less massive, younger bulges at $z \simeq 1$ grow through secular evolution processes (Kormendy & Kennicutt 2004). At $z \simeq 1$, it is possible that we are seeing these galaxies still forming, and these "disk-like" bulges might grow from disk material or minor mergers to become more massive bulges observed at present day. Disk-like pseudo-bulges can also grow by gas inflow and star-formation. Bars can drive central gas inflows (Sheth *et al.* 2005), and therefore, there could be a correlation between these disky bulges and central bars. Sheth *et al.* (2008) find that the bar fraction in very massive, luminous spirals is constant from $z \simeq 0$ to $z \simeq 0.84$, whereas for low-mass, blue spirals it declines significantly with redshift to about $\sim$20% at $z \sim 0.84$, indicating that some bars do form early enough. Elmegreen *et al.* (2005) has morphologically classified

few ($\sim$10%) of our sample galaxies as barred galaxies, so it will be interesting to investigate these late-type galaxies in future studies to understand this relation.

Aperture color analysis by Ellis *et al.* (2001) for bulges at $z < 0.6$ in early-type and spiral galaxies with $I_{AB} < 24$ mag found that their central colors are redder than the surrounding outer disk colors, but that these central colors are bluer than those of pure ellipticals at the same redshifts. Figure 30 suggests that our results agree with Ellis *et al.* (2001). This is not perhaps surprising, since we also select our sample based on galaxy total-magnitudes, with no constraints on its bulge magnitude. In comparison, Koo *et al.* (2005) select their sample based on bulge luminosity, and they find that luminous, high-redshift ($0.73 < z < 1.04$) bulges ($I_{AB} < 24$ mag) within the Groth Strip Survey are very red/old. They clearly show that if the bulge sample is luminous, then all bulges are equally red and old. In contrast, we show that if the bulge sample is selected without any constraint on the bulge magnitude, then late-type bulges are younger than bulges in early-type galaxies at similar redshifts.

Galaxy colors and structural properties show a bimodal distribution, separating into a red sequence, populated by early-type galaxies, and a blue "cloud", populated by late-type galaxies (Balogh *et al.* 2004; Driver *et al.* 2006). Whether a galaxy resides in a red sequence or a blue cloud is also related to the type of bulge in a galaxy (Drory & Fisher 2007). Figure 20 shows this bimodal distribution. Our late-type galaxies with pseudo bulges lie in the bluer cloud compared to early-type galaxies that lie on the red color sequence. This clearly shows that the processes involved in the formation of galactic bulges and their host galaxies are very similar. Observations indicate that

these formation mechanisms depend strongly on the bulge (as well galaxy) mass, and that they were active already at $z \simeq 1.3$. This evidence is strengthened by the results of Thomas & Davies (2006) and MacArthur *et al.* (2008), who find that bulges of similar mass have a similar evolutionary path. Possibly because of cosmic variance, we do not detect early-type spirals at $z \simeq 1$ in the HUDF. Comparing our sample of late-type bulges with the massive early-type galaxies at similar redshifts studied by Pasquali *et al.* (2006b), we confirm the existence of different evolutionary tracks for bulges in early- and late-type galaxies (see Figure 20).

Our analysis of the deepest optical survey, the HUDF, along with the deep unique ACS grism spectroscopy provides the best spatial resolution at $z \simeq 1$, and yields more detailed insight in the process of galaxy formation. Massive and luminous bulges (e.g., Koo *et al.* 2005), which mostly reside in early-type galaxies and in earlier-type spiral galaxies, are old and formed at $z \gtrsim 2$. The secular evolution suggested by Kormendy & Kennicutt (2004) does not play any role in their formation. Our ACS grism study of the HUDF here has shown that lower-mass bulges, which are mostly associated with later-type galaxies, are younger and form at $z \lesssim 2$ possibly via secular evolution.

5. DISCUSSION & CONCLUSIONS

5.1. *Overview*

In this final section, a summary of results from three studies investigating structural and physical properties of high redshift galaxies in the Hubble Ultra Deep Field (HUDF) is presented. This is followed by a description of the future prospects for understanding high redshift galaxies using deep ground-based spectroscopy and new upcoming space-based instruments on the *Hubble Space Telescope* (*HST*) and the *James Webb Space Telescope* (*JWST*). Deep ground-based spectroscopy from 8m-10m class telescope (e.g., *Keck*, *Very Large Telescope (VLT)*, *Southern African Large Telescope (SALT)*, *Large Binocular Telescope (LBT)*) is necessary to understand physical characteristics of these high redshift galaxies, while upcoming Wide Field Camera-3 (WFC3) on the *HST* and Near-Infrared Camera (NIRCam) on the *JWST* are necessary to secure multi-wavelength data and morphological information for many known and yet to be discovered high-redshift galaxies. A preview of what such observations might show is given by, e.g., Windhorst *et al.* (2008).

5.2. *Summary of Results*

Surface brightness profiles at $z \simeq 4-6$ (chapter 2). — We used the stacked HUDF images to analyze the average surface brightness profiles of $z \simeq 4-6$ galaxies at the *HST* diffraction limit. Our analysis shows that even the faintest galaxies at $z \simeq 4-6$ are resolved. This may have implications for their stellar density and its relation to the stellar density in present-day galaxies. We also find that the average surface brightness profiles display "breaks" at a radius that progresses toward lower redshift from $r \simeq 0\farcs27$ (1.6 kpc) at $z \simeq 6$ to $r \simeq 0\farcs35$ (2.5 kpc) at $z \simeq 4$.

The shape of the radial surface brightness profile that we observe (Figure 10) could result from a mixture of different morphological types of galaxies, if they existed at $z \simeq 4-6$, because we can produce similar breaks in the surface brightness profiles when we mix different types of nearby galaxies. Alternatively, if these galaxies are dominated by a central starburst, then they could show such double exponential-type profiles, as discussed by Hunter & Elmegreen (2006). In a third scenario, if the galaxies at $z \simeq 4-6$ are truly young and mostly late-type objects, the outer profiles seen in our mean radial surface-brightness profiles at $z \simeq 4-6$ bear the imprint of the hierarchical build-up process and are still dominated by in-falling material, which is *not* detectable in the individual HUDF images of these faint objects. We have estimated limits to the dynamical ages from the break radius at $z \simeq 4, 5$, and 6 very roughly as ∼0.20, 0.14 and 0.10 Gyr, respectively. These ages are similar to the Spectral Energy Distribution (SED) ages inferred at $z \simeq 4-6$ (Yan *et al.* 2005; Eyles *et al.* 2005, 2007), and they are consistent with SED ages suggested for $z \simeq 7$ (Labbé *et al.* 2006). Hence, at $z \simeq 4, 5, 6$, the last major merger that affected the surface brightness profiles that we observe, and that triggered the observed star-burst, may have occurred respectively ∼0.20, 0.14 and 0.10 Gyr earlier, or very approximately at $z \simeq 4.5, 5.5, 6.5$. This would be consistent with the hierarchical assembly of galaxies and with the end of the epoch of reionization, since it would imply that going from $z \simeq 4$ to $z \simeq 6$, the SEDs become progressively more dominated by late-B–late-O stars. This, in turn, implies that sub-L^* (i.e., dwarf) galaxies may have produced sufficient numbers of energetic UV photons to complete the reionization process by $z \simeq 6$, as

Yan & Windhorst (2004a,b) suggested. It will be imperative to study with future instruments like *HST*/WFC3 and *JWST* (Windhorst *et al.* 2006, 2008) whether the dominant stellar population indeed changes from late-O–early-B at $z \simeq 6$ (i.e., capable of reionizing) to mid- to late-B at $z \simeq 4-5$ (i.e., capable of maintaining reionization), and to what extent the intrinsic sizes of these faint objects will ultimately limit deep *JWST* surveys.

Starburst intensity limit at $z \simeq 5$–6 (chapter 3). — We have measured the starburst intensity limit for *spectroscopically confirmed* galaxies at $z \simeq 5$–6 from Advanced Camera for Surveys (ACS) grism survey GRism ACS Program for Extragalactic Science (GRAPES) in the HUDF. We find that there is little variation in the upper limit of the surface brightness from $z \simeq 3$ to $z \simeq 6$, and that the starburst intensity limit is within a factor of 3 when compared with the sample of $z \simeq 3-4$ galaxies (Figure 15). The constancy of the starburst intensity limit for starburst galaxies at $z \simeq 5-6$ — combined with the results obtained by Meurer *et al.* (1997) for starbursts at $z \lesssim 3$ — implies that the physical processes limiting the starburst intensity at lower redshifts also apply to these high redshift galaxies. We find that the high redshift starbursts have a smaller characteristic linear size than their local counterparts, and a correspondingly lower luminosity (since their maximum surface brightnesses are similar and their sizes smaller). We observe the apparent galaxy size evolution from $z \simeq 3$ to $z \simeq 6$ and find that the sizes scale approximately as the Hubble parameter $H^{-1}(z)$. Finally, using rest-frame UV colors, we conclude that the evolution in the UV spectral slope from $z \simeq 3$ to $z \simeq 6$ reinforces the evolution of dust, which leads to bluer galaxies

at $z \simeq 5-6$ compared to galaxies at $z \simeq 3$. This implies that starbursts were less obscured, when the universe was younger and had lower heavy element abundances. Any future search for galaxies at higher redshifts (e.g., *JWST*; Windhorst *et al.* 2008) needs to take into account the size evolution and constancy of the maximum surface brightness, and therefore the decrease in characteristic luminosity with redshift.

Late-type galaxies at $z \simeq 1$ (chapter 4). — We have estimated the stellar ages and masses of 34 bulges of late-type galaxies observed in the HUDF by fitting stellar population models to the 4000 Å break observed in the GRAPES grism spectra (Figure 26). This study takes advantage of the exceptional angular resolution and depth of the GRAPES/HUDF data which allow us to identify the bulge component of the sample galaxies at $z \simeq 1$ both on the direct *HST* and on the ACS grism images, and to extract its corresponding spectrum. We find that bulges in late-type galaxies at high redshift ($z \simeq 1$) appear to be predominantly young (with an average age$\sim$1.3 Gyr) and less massive ($6.5 \leq log(M_s/M_\odot) \leq 10.0$) than bulges in early-type galaxies at the same redshift. This finding is robust against the amount of disk-light underneath the bulge light. Our results support the scenario where low-mass late-type bulges formed through secular evolution processes, perhaps driven by minor mergers or infall.

5.3. *Future Work*

In the past decade, ground and space-based observations of high redshift galaxies have begun to disentangle the process of galaxy assembly. The details of that process at high redshifts, however, remain poorly constrained. There is presently little

information on the dynamical structure of these or other galaxies at $z \simeq 6$. It is not clear whether these objects represent isolated disk systems, or collapsing spheroids, mergers, and/or other dynamically young objects. Distinction between these possible morphologies and, therefore, a better estimate of the formation redshifts of the systems observed at $z \simeq 4-6$ in particular, is important for testing the galaxy assembly picture, and for the refinement of galaxy formation models.

We cannot compare structure formation calculations to the observed galaxy populations without knowledge of their star formation processes. It is therefore essential to directly measure the properties of star-formation events in the distant universe, and see how they compare with their nearby counterparts. Projects like the GRAPES in the HUDF and the Probing Evolution And Reionization Spectroscopically (PEARS) in the Great Observatories Origins Deep Survey (GOODS) fields provide excellent samples of faint spectroscopically confirmed high redshift galaxies (Malhotra *et al.* 2005; Hathi *et al.* 2008a; Malhotra *et al.* 2008), along with the brighter Lyman-break galaxies (LBGs)/Lyman-α Emitters (LAEs) confirmed by ground-based telescopes at $z \geq 4.5$.

Future science goals are to characterize the star-formation properties, dust content, the stellar populations and the rest-frame ultraviolet (UV)/optical morphologies for large numbers of spectroscopically confirmed LBGs at $z \geq 4.5$. To accomplish these goals, we will use deep WFC3 Near-Infrared (NIR) images from the *HST*, deep NIR ground-based spectroscopy (using 8m-10m class telescopes) and mid Infrared (IR) data from the *Spitzer Space Telescope* (*Spitzer*). Future NIR imaging and spec-

troscopic instruments such as LBC and/or LUCIFER on 2×8.4m *Large Binocular Telescopes (LBT)* will be an additional asset to this proposed research. These goals are inter-related research areas in which, existing and upcoming instruments will play major role addressing the issues of star-formation process and structural evolution in high redshift galaxies.

Starburst activity and stellar population at $z \simeq 5-6$. — Studies of low redshift starbursts have established that the UV spectral slope (β) is a good indicator of dust reddening, and correlates with the far-IR emission from dust (Meurer *et al.* 1997). There are many indications that galaxies at $z \simeq 5-6$ are bluer in the UV than $z \simeq 3-4$ galaxies (e.g., Stanway *et al.* 2005; Bouwens *et al.* 2006). We (Hathi *et al.* 2008a, Chapter 3) find that the UV slope of $z \simeq 5-6$ galaxies ($\beta \simeq -1.70$) is bluer than that of $z \simeq 3$ galaxies ($\beta \simeq -1.10$), although the current sample size remains too small for definite conclusions. This we intend to improve upon drastically in next few years with the *HST*/WFC3.

Estimation of dust extinction is important for measuring the star-formation rate (SFR) from the UV continuum. Heckman (2005) has proposed that the most useful parameter to compare local starbursts with physically similar galaxies at high-z is its 'intensity' (i.e., SFR/area). We (Hathi *et al.* 2008a, Chapter 3) measured an upper limit to the starburst intensity for LBGs at $z \simeq 4-6$, and when we combine our results with those of Meurer *et al.* (1997) at $z \simeq 0-3$, we find that this starburst intensity limit does not change much between $z \simeq 0$ and 6. Does this mean that physical mechanisms (e.g., galactic winds) limiting this starburst intensity occur similarly for

local and high-z starbursts? At the moment, we don't know. Proposed observations of high-z galaxies with the *HST*/WFC3 will help to understand these details.

To identify "old" stellar populations (i.e., stars older than 10^8 years) or dusty star formation regions, we need to observe high redshift ($z \simeq 5$–6) galaxies at their rest-frame optical wavelengths. NIR and mid IR observations are essential to accurately determine their SEDs and rest-frame optical properties. At the redshift of these galaxies, the (H–3.6μm) color constrains the 4000 Å break, and thus can accurately constrain the population of old stars (e.g., Yan *et al.* 2005). At these redshifts and flux levels, there is no better way to constrain the presence of old stars than to combine NIR and mid IR fluxes to measure the 4000 Å break before the launch of *JWST*.

We are presently involved in the *HST*/ACS PEARS project, which through low-resolution *HST* grism spectroscopy in GOODS-S and GOODS-N has identified and confirmed $\gtrsim$100 galaxies at $z \geq 4.5$. The rest-frame UV continuum of these galaxies correspond to the NIR observed-frame. Using deep, high resolution *HST* J, H images, we will obtain very accurate NIR fluxes to measure the UV spectral slope β (which measures dust) and the corresponding starburst intensity limit for these high-z galaxies. Low-resolution grism spectra will also be used to confirm the measured UV slope. We will use deep ground-based spectroscopy to measure a wide variety of physical parameters for these galaxies: confirm their redshifts, make independent estimate of β, measure linewidths and/or rotation velocities in many cases, dynamical masses, equivalent widths of their emission lines, their metallicities and SFRs for these galaxies. *Spitzer*/IRAC fluxes will be obtained from the deep archival data

in the GOODS (PI: M. Dickinson). Combining *HST*, *Spitzer* and grism data, we can estimate ages and masses of their dominant stellar populations in these galaxies. If we identify old stellar populations (i.e., age $> 3{\times}10^8$ years) in spectroscopically confirmed L* galaxies at $z{\simeq}5{-}6$, we immediately know that they formed at redshifts $z_{form} \gtrsim 7-8$, and so we can estimate their contribution to the reionizing photon budget at $z > 7$ (e.g., Yan & Windhorst 2004a).

Surface brightness (SB) profiles of galaxies at $z{\simeq}4$–6. — The HUDF, GOODS and deep ACS/WFC parallel fields contain $\gtrsim$500 objects (Beckwith *et al.* 2006; Bouwens *et al.* 2006, 2007; Yan & Windhorst 2004a,b) which are B, V, i'-band dropouts, making them candidates for galaxies at $z \simeq 4$,5,6, respectively. Despite the depth (to AB$\lesssim$27–29.5 mag) of these *HST* fields, however, these objects appear very faint, with little discernable structural detail.

The similarity in flux and appearance of many of the $z \simeq 6$ candidates in the HUDF identified by Yan & Windhorst (2004b) suggested that it may be possible to gain information about their dynamical structure, by creating composite images from objects that are matched in flux, shape and size. Such a composite would effectively correspond to a single galaxy detectable at a much higher signal-to-noise (S/N) ratio, equivalent to $\sim$4500 *HST* orbits ($\sim$3000 hrs) on a single such object. At AB$\simeq$27–29.5 mag, measuring reliable radial SB profiles is not possible for most individual objects, but a composite radial profile has much higher S/N and could be meaningful, as long as the objects are intrinsically similar and at the same redshift.

We (Hathi *et al.* 2008b, Chapter 2) conducted a preliminary study by stacking a small numbers (30 objects at each redshift bin at $z \simeq 4, 5, 6$) of compact and isolated $z \simeq 4$–6 galaxy candidates in the HUDF to study their *average* radial SB profiles. Our results show that image stacking provides reliable, reproducible average SB-profiles. The shape of the average SB profiles shows that even the faintest $z \simeq 4-6$ objects are *resolved* at the *HST* diffraction limit. The mean SB profiles shows that the average compact galaxy at $z \simeq 4-6$ is clearly extended with respect to the ACS Point Spread Function (PSF), and can be fitted to a $r^{1/n}$ profile to a radius of $r \simeq 0\farcs35$–$0\farcs27$. The radius at which the profile starts to deviate from $r^{1/n}$ (e.g., $r \simeq 0\farcs31$ for $z \simeq 5$) may put an important constraint to the dynamical time scale of the system. The average profiles and the observed deviations could help us to gain insight into the stellar population that dominate the inner profiles. This method could provide an *independent way* of estimating ages of these stellar populations, and thus far seems to suggest dynamical ages of 0.2-0.1 Gyr, i.e., similar to their SED ages at these redshifts.

We can apply this approach on large number of 'dropouts' from the HUDF, GOODS and deep ACS/WFC parallel fields to undertake a much more detailed and comprehensive analysis, to conclusively establish what is the physical significance of these composite radial light-profiles of $z \simeq 4$–6 objects. We can use previously discussed PEARS/GRAPES projects and deep NIR spectroscopy to confirm many of these faint 'dropouts', and understand any evolution in their rest-frame average UV SB profiles from $z \simeq 6$ to $z \simeq 4$. In future, the 6.5 meter *JWST* can confirm our

results at 1μ in $\sim$250 hrs. Therefore, we will use this large high-resolution space-based IR telescope to investigate the morphological structure of individual galaxies at $z \simeq 6$. The *JWST*, to be launched in 2013, will accomplish that in $(1/12)^{th}$ of the time compared to present capabilities. It is therefore critical that *JWST* be designed and built to allow to do ultra-deep near-mid IR surveys, and subtract the sky to a precision better than 10^{-3} of the zodiacal foreground.

REFERENCES

Abraham, R. G., Ellis, R. S., Fabian, A. C., *et al.* 1999, MNRAS, 303, 641

Adelberger, K. L., & Steidel, C. C. 2000, ApJ, 544, 218

Athanassoula, E. 2005, MNRAS, 358, 1477

Athanassoula, E. 2008, IAU Symposium 245 "Galactic bulges", M. Bureau *et al.* eds (arXiv:0802.0151)

Balogh, M.L., Morris, S. L., Yee, H. K. C., *et al.* 1999, ApJ, 527, 54

Balogh, M.L., Baldry, I. K., Nichol, R., *et al.* 2004, ApJ, 615, L101

Baugh, C. M., Cole, S., & Frenk, C. S. 1996, MNRAS, 283, 1361

Beckwith, S., Stiavelli, M., Koekemoer, A. M., et al. 2006, AJ, 132, 1729

Benitez, N. 2000, ApJ, 536, 571

Bershady, M. A., Jangren, A., & Conselice, C. J. 2000, AJ, 119, 2645

Bertin, E., & Arnouts, S. 1996, A&AS, 117, 393

Binney, J. J., & Tremaine, S. 1987, Galactic Dynamics (Princeton: Princeton Univ. Press)

Bolzonella, M., Miralles, J. M., & Pelló, R. 2000, A&A, 363, 476

Bouwens, R., Cayón, L., & Silk, J. 1999, ApJ, 516, 77

Bouwens, R., Illingworth, G. D., Thompson, R. I., *et al.* 2004a, ApJ, 606, L25

Bouwens, R. J., Illingworth, G. D., Blakeslee, J. P., *et al.* 2004b, ApJ, 611, 1

Bouwens, R. J., Illingworth, G. D., Blakeslee, J. P., *et al.* 2006, ApJ, 653, 53

Bouwens, R. J., Illingworth, G. D., Franx, M., *et al.* 2007, ApJ, 670, 928

Brandt, W. N., Hornschemeier, A. E., Schneider, D. P., *et al.* 2001, ApJ, 558, L5

Bruzual, G., & Charlot, S. 2003, MNRAS, 344, 1000

Bunker, A. J., Stanway, E. R., Ellis, R. S., *et al.* 2004, MNRAS, 355, 374

Calzetti, D., Kinney, A. L., & Storchi-Bergmann, T. 1994, ApJ, 429, 582

Carollo, C. M., Scarlata, C., Stiavelli, M., *et al.* 2007, ApJ, 658, 960

Chabrier, G. 2003, PASP, 115, 763

Coe, D., Benitez, N., Sánchez, S. F., *et al.* 2006, AJ, 132, 926

Conselice, C. J., Bershady, M. A., & Jangren, A. 2000, ApJ, 529, 886

Conselice, C. J. 2003, ApJS, 147, 1

Conselice, C. J., Blackburne, J. A., & Papovich, C. 2005, ApJ, 620, 564

Courteau, S., de Jong, R. S., & Broeils, A. H. 1996, ApJ, 457, L73

Cowie, L. L., Songaila, A., Hu, E. M., *et al.* 1996, AJ, 112, 839

Davis, M., & Peebles, P. J. M. 1983, ApJ, 267, 465

Davis, M., Guhathakurta, P., Konidaris, N. P., *et al.* 2007, ApJ, 660, L1

de Jong, R. S. 1996, A&AS, 118, 557

Dong, X. Y. & De Robertis, M. M. 2006, AJ, 131, 1236

Dow-Hygelund, C., Holden, B., Bouwens, R., *et al.* 2007, ApJ, 660, 47

Driver, S. P., Windhorst, R. A., & Griffiths, R. E. 1995, ApJ, 453, 48

Driver, S. P., Fernandez-Soto, A., Couch, W. J., *et al.* 1998, ApJ, 496, L93

Driver, S. P., Allen, P. D., Graham, A. W., *et al.* 2006, MNRAS, 368, 414

Drory, N. & Fisher, D. B. 2007, ApJ, 664, 640

Ellis, R. S., Abraham, R. G., & Dickinson, M. 2001, ApJ, 551, 111

Elmegreen, D. M., Elmegreen, B. G., Rubin, D. S., *et al.* 2005, ApJ, 631, 85

Eyles, L. P., Bunker, A. J., Stanway, E. R., *et al.* 2005, MNRAS, 364, 443

Eyles, L. P., Bunker, A. J., Ellis, R. S., *et al.* 2007, MNRAS, 374, 910

Fan, X., Strauss, M. A., Becker, R. H., *et al.* 2006, AJ, 132, 117

Ferguson, H. C., Dickinson, M., Giavalisco, M., *et al.* 2004, ApJ, 600, L107

Fernández-Soto, A., Lanzetta, K. M., & Yahil, A. 1999, ApJ, 513, 34

Ferreras, I., & Silk, J. 2000, MNRAS, 316, 786

Ferreras, I., Lisker, T., Carollo, C. M., *et al.* 2005, ApJ, 635, 243

Georgakakis, A., Hopkins, A. M., Sullivan, M., *et al.* 2003, MNRAS, 345, 939

Giavalisco, M., Steidel, C. C., & Macchetto, F. D. 1996, ApJ, 470, 189

Giavalisco, M., Ferguson, H. C., Koekemoer, A. M., *et al.* 2004a, ApJ, 600, L93

Giavalisco, M., Dickinson, M., Ferguson, H. C., *et al.* 2004b, ApJ, 600, L103

Gonzaga, S., *et al.* 2005, "ACS Instrument Handbook", Version 6.0, (Baltimore:STScI)

Grazian, A., Fontana, A., de Santis, C., *et al.* 2006, A&A, 449, 951

Guzman, R., Gallego, J., Koo, D. C., *et al.* 1997 ApJ, 489, 559

Hathi, N. P., Malhotra, S., & Rhoads, J. 2008a, ApJ, 673, 686

Hathi, N. P., Jansen, R. A., Windhorst, R. A., *et al.* 2008b, AJ, 135, 156

Hathi, N. P., Ferreras, I., Pasquali, A., *et al.* 2008c, ApJ, accepted (arXiv:0805.0791)

Heavens, A., Panter, B., Jimenez, R., *et al.* 2004, Nature, 428, 625

Heckman, T. M., Armus, L., & Miley, G. K. 1990, ApJS, 74, 833

Heckman, T. M., Lehnert, M. D., Strickland, D. K., *et al.* 2000, ApJS, 129, 493

Heckman, T. M. 2001, in ASP Conf. Ser. 240, Gas and Galaxy Evolution, ed. J. E. Hibbard, M. Rupen, & J. H. van Gorkom (San Francisco: ASP), 345

Heckman, T. M. 2005, ASSL, 329, 3

Hernquist, L. & Mihos, J. C. 1995, ApJ, 448, 41

Holwerda, B. W. 2005, (arXiv:0512139)

Hu, E. M., Cowie, L. L., McMahon, R. G., *et al.* 2002, ApJ, 568, L75

Huchra, J. P., Davis, M., Latham, D., *et al.* 1983, ApJS, 52, 89

Hunter, D. A., & Elmegreen, B. G. 2006, ApJS, 162, 49

Jansen, R. A. & Kannappan, S. J. 2001, Ap&SS, 276, 1151

Jansen, R. A., Franx, M., Fabricant, D., *et al.* 2000a, ApJS, 126, 271

Jansen, R. A., Fabricant, D., Franx, M., *et al.* 2000b, ApJS, 126, 331

Kannappan, S. J., Jansen, R. A., & Barton, E. J. 2004, AJ, 127, 1371

Kauffmann, G., White, S. D. M., & Guiderdoni, B. 1993, MNRAS, 264, 201

Kauffmann, G., Heckman, T. M., White, S. D. M., *et al.* 2003, MNRAS, 341, 33

Kennicutt, R. C., Jr. 1998, ARA&A, 36, 189

Kinney A. L., Calzetti D., Bohlin R. C., *et al.* 1996, ApJ, 467, 38

Kodaira, K., Taniguchi, Y., Kashikawa, N., *et al.* 2003, PASJ, 55, L17

Kodama, T., Yamada, T., Akiyama, M., *et al.* 2004, MNRAS, 350, 1005

Koekemoer, A. M., Fruchter, A. S., Hook, R. N., *et al.* 2002, The 2002 *HST* Calibration Workshop, ed. S. Arribas, A. Koekemoer, and B. Whitmore (Baltimore:STScI), 337

Koo, D. C., Simard, L., Willmer, C. N. A., *et al.* 2005, ApJS, 157, 175

Kormendy, J. 1977, ApJ, 218, 333

Kormendy, J. & Kennicutt, R. C. 2004, ARA&A, 42, 603

Kron, R. G. 1980, ApJS, 43, 305

Kurk, J. D., Cimatti, A., di Serego A, S., *et al.* 2004, A&A, 422, L13

Labbé, I., Bouwens, R., Illingworth, G. D., *et al.* 2006, ApJ, 649, L67

Lehnert, M. D., & Heckman, T. 1996, ApJ, 472, 546

Lehnert, M. D., Bremer, M., Verma, A., *et al.* 2007, in ASP Conf. Ser., Pathways Through an Eclectic Universe, ed. J. H. Knappen, T. J. Mahoney, & A. Vazedekis (arXiv:0708.3000)

Leitherer, C., Schaerer, D., Goldader, J. D., et al. 1999, ApJS, 123, 3

Liu, X., Shapley, A., Coil, A., *et al.* 2008, ApJ, 678, 758

Lynden-Bell, D. 1967, MNRAS, 136, 101

MacArthur, L. A., Courteau, S., Bell, E., *et al.* 2004, ApJS, 152, 175

MacArthur, L. A., Ellis, R. S., Treu, T., *et al.* 2008, ApJ, 680, 70

Madau, P. 1995, ApJ, 441, 18

Malhotra, S., Rhoads, J. E., Pirzkal, N., *et al.* 2005, ApJ, 626, 666

Malhotra, S., Pirzkal, N., Rhoads, J., *et al.* 2008, ApJ, in preparation

Maraston, C. 2005, MNRAS, 362, 799

Marzke, R. O., Huchra, J. P. & Geller, M. J. 1994, ApJ, 428, 43

McCarthy, P. J. 2004, BAAS, 36, 1555

Menanteau, F., Abraham, R. G., & Ellis, R. S. 2001, MNRAS, 322, 1

Meurer, G. R., Heckman, T. M., Leitherer, C., *et al.* 1995, AJ, 110, 2665

Meurer, G. R., Heckman, T. M., Lehnert, M. D., *et al.* 1997, AJ, 114, 54 (M97)

Meurer, G. R., Heckman, T. M., & Calzetti, D. 1999, ApJ, 521, 64

Mobasher, B., Idzi, R., Benitez, N., *et al.* 2004, ApJ, 600, L167

Mobasher, B., Capak, P., Scoville, N., *et al.* 2007, ApJS, 172, 117

Nandra, K., Mushotzky, R. F., Arnaud, K., 2002, ApJ, 576, 625

Oke, J. B., & Gunn, J. E. 1983, ApJ, 266, 713

Padmanabhan, N., Seljak, U., Strauss, M. A., *et al.* 2004, New Astronomy, 9, 329

Panter, B., Jimenez, R., Heavens, A. F., *et al.* 2007, MNRAS, 378, 1550

Pascarelle, S. M., Windhorst, R. A., Keel, W. C., *et al.* 1996, Nature, 383, 45

Pasquali, A., Pirzkal, N., Larsen, S., *et al.* 2006a, PASP, 118, 270

Pasquali, A., Ferreras, I., Panagia, N., *et al.* 2006b, ApJ, 636, 115

Peletier, R. F. & Balcells, M. 1996, AJ, 111, 2238

Peng, C. Y., Ho, L. C., Impey, C. D., *et al.* 2002, AJ, 124, 266

Petrosian, V. 1976, ApJ, 209, L1

Pirzkal, N., Xu, C., Malhotra, S., *et al.* 2004, ApJS, 154, 501

Pirzkal, N., Sahu, K. C., Burgasser, A., *et al.* 2005, ApJ, 622, 319

Pirzkal, N., Malhotra, S., Rhoads, J., *et al.* 2007, ApJ, 667, 49

Ravindranath, S., Giavalisco, M., Ferguson, H. C., et al. 2006, ApJ, 652, 963

Rhoads, J. E., Xu, C., Dawson, S., *et al.* 2004, ApJ, 611, 59

Rhoads, J. E., Malhotra, S., Pirzkal, N., *et al.* 2008, ApJ, submitted (arXiv:0805.1056)

Rix, H-W., Barden, M., Beckwith, S., *et al.* 2004, ApJS, 152, 163

Ryan, R. E., Jr., Hathi, N. P., Cohen, S. H., *et al.* 2005, ApJ, 631, L159

Ryan, R. E., Jr., Hathi, N. P.; Cohen, S. H., *et al.* 2007, ApJ, 668, 839

Sérsic, J. L. 1968, Atlas de galaxias australes

Saha, P. 2003, *Principles of Data Analysis*, Cappella Archive.

Salpeter, E. E. 1955, ApJ, 121, 161

Schiavon, R., Faber, S. M., Konidaris, N., *et al.* 2006, ApJ, 651, L93

Scoville, N., Abraham, R. G., Aussel, H., *et al.* 2007, ApJS, 172, 150

Shapley, A. E., Coil, A., Ma, C-P., *et al.* 2005, ApJ, 635, 1006

Sheth, K., Vogel, S. N., Regan, M. W., *et al.* 2005, ApJ, 632, 217

Sheth, K., Elmegreen, D. M., Elmegreen, B. G., *et al.* 2008, ApJ, 675, 1141

Simien, F., & de Vaucouleurs, G. 1986, ApJ, 302, 564

Sparks, W. B., *et al.* 2001, ACS Default (Archival) Pure Parallel Program (ISR01-06)

Spergel, D. N., Bean, R., Doré, O., *et al.* 2007, ApJS, 170, 377

Stanway, E. R., McMahon, R. G., & Bunker, A. J. 2005, MNRAS, 359, 1184

Steidel, C. C. & Hamilton, D. 1992, AJ, 104, 941

Steidel, C. C., & Hamilton, D. 1993, AJ, 105, 2017

Steidel, C. C., Giavalisco, M., Pettini, M., *et al.* 1996a, ApJ, 462, L17

Steidel, C. C., Giavalisco, M., Dickinson, M., *et al.* 1996b, AJ, 112, 352

Steidel, C. C., Adelberger, K. L., Giavalisco, M., *et al.* 1999, ApJ, 519, 1

Stern, D., Yost, S. A., Eckart, M. E., *et al.* 2005, ApJ, 619, 12

Stetson, P. B. 1987, PASP, 99, 191

Taniguchi, Y., Ajiki, M., Nagao, T., *et al.* 2005, PASJ, 57, 165

Taylor-Mager, V. A., Conselice, C. J., Windhorst, R. A., *et al.* 2007, ApJ, 659, 162

Thielemann, F-K., Nomoto, K., & Hashimoto, M. 1996, ApJ, 460, 408

Thomas, D., & Davies, R. L. 2006, MNRAS, 366, 510

Thompson, R. I., Illingworth, G., Bouwens, R., *et al.* 2005, AJ, 130, 1

Tolman, R. C. 1930, PNAS, 16, 511

Tolman, R. C. 1934, *Relativity, Thermodynamics, & Cosmology*, (Oxford: Oxford Univ. Press), 467

van Albada, T. S. 1982, MNRAS, 201, 939

van den Bosch, F. C. 1998, ApJ, 507, 601

van den Hoek, L. B., & Groenewegen, M. A. T. 1997, A&AS, 123, 305

van Dokkum, P. G., Förster, S., Natascha, M., *et al.* 2003, ApJ, 587, L83

van Dokkum, P. G., Franx, M., Förster, S., *et al.* 2004, ApJ, 611, 703

Vanzella, E., Cristiani, S., Dickinson, M., *et al.* 2006, A&A, 454, 423

Vanzella, E., Cristiani, S., Dickinson, M., *et al.* 2008, A&A, 478, 83

Vázquez, G. A., & Leitherer, C. 2005, ApJ, 621, 695

Weedman, D. W., Wolovitz, J. B., Bershady, M. A., *et al.* 1998, AJ, 116, 1643 (W98)

White, R. L., Helfand, D. J., Becker, R. H., *et al.* 2007, ApJ, 654, 99

Williams, R. E., Blacker, B., Dickinson, M., *et al.* 1996, AJ, 112, 1335

Windhorst, R. A., Gordon, J. M., Pascarelle, S. M., *et al.* 1994, ApJ, 435, 577

Windhorst, R. A., Keel, W. C., & Pascarelle, S. M. 1998, ApJ, 494, 27

Windhorst, R. A., Taylor, V. A., Jansen, R. A., *et al.* 2002, ApJS, 143, 113

Windhorst, R. A., Cohen, S. H., Jansen, R. A., *et al.* 2006, NewAR, 50, 113

Windhorst, R. A., Hathi, N. P., Cohen, S. H., *et al.* 2008, *Advances in Space Research*, 41, 1965

Wright, E. L. 2006, PASP, 118, 1711

Yan, H., Windhorst, R. & Cohen, S. 2003, ApJ, 585, L93

Yan, H. & Windhorst, R. 2004a, ApJ, 600, L1

Yan, H. & Windhorst, R. 2004b, ApJ, 612, L93

Yan, H., Dickinson, M., Stern, D., *et al.* 2005, ApJ, 634, 109

Yan, H., Hathi, N. P., & Windhorst, R. A. 2008, ApJ, 675, 136

York, D. G., Adelman, J., Anderson, J. E., Jr., *et al.* 2000, AJ, 120, 1579

Zibetti, S., White, S. D. M., & Brinkmann, J. 2004, MNRAS, 347, 556